

A CRITICAL APPRAISAL OF NANOINDENTATION WITH  
APPLICATION TO ELASTIC-PLASTIC SOLIDS AND SOFT  
MATERIALS

Thesis By

Poh Chieh Benny Poon

In Partial Fulfillment of the Requirements for the

Degree of

Doctor of Philosophy



CALIFORNIA INSTITUTE OF TECHNOLOGY

Pasadena, California

2009

(Defended on Sept 12, 2008)

©2009

Benny Poon

All Rights Reserved

To my family and friends

## ACKNOWLEDGEMENTS

Through my graduate career, I have been fortunate to meet many individuals who all have made indelible imprints in my journey. It is to my chagrin that I will not be able to acknowledge each one of them here, so this acknowledgement is not, and cannot be, complete. Instead, I would like to highlight and thank these 3 people who have left the deepest impressions and consequently, molded me intellectually.

When I first started my PhD career, I unwittingly worked with Professor Daniel Rittel, not knowing that he would have such an impact on my life. His hands-on mentoring kept me focused, and endless questions taught me critical thinking. Unquestionably, he has played a significant role in shaping the way I think and approach scientific problems. I will always be thankful for your guidance, without which I would not have accomplished this work.

During my years amidst the cornfields in Urbana-Champaign, my sanity was kept somewhat intact by my undergraduate advisor, Professor John Lambros. By nurturing my interest in solid mechanics, I attribute to his patient and tireless mentorship the reason why I stumbled into graduate school in the first place. I will always be grateful for all the times you came into the lab to personally show the greenhorn I was then how things worked.

Most importantly, to my formidable racketball partner and graduate advisor Professor Guruswami Ravichandran, I will always treasure our long talks and advising sessions. Your mentorship truly extended beyond the boundaries of the classroom and lab. Thank you for guiding me in ways that I cannot possibly list, or even realize, and for

extending more support and understanding than I deserved; for affording me the freedom to steer my own research project and the opportunities to work with accomplished scientists from all over the world. My years at Caltech under your tutelage have been, scientifically and personally, the most enlightening years of my life thus far.

Last but not least, I would like to extend my sincere thanks to my mentors and colleagues (Dr. J. Zhao, Dr. E. Bouchaud, Dr. R. Conner, Dr. L. Ponson, M. Mello, J. Rimoli, L. Zheng, Dr. C. Franck, M. Gonzalez, L. Bo, A. Tchieu, J.T. de Besombes, J.Y. Suh, X. Lu, Dr. M. Tao, L. Miranda, P. Arakelian, S. Kramer, C. Kovalchick) for helping me in numerous ways; my defense committee (Professors K. Bhattacharya, C. Daraio, N. Lapusta, G. Ravichandran, D. Rittel) for your insightful critique and advice; and my family and friends, without whose love and support, all this would never have been possible.

Finally, this work is made possible through the generous funding by the National Science Foundation (DMR # 0520565) through the Center for Science and Engineering of Materials (CSEM) at the California Institute of Technology. I also thank the Ronald and Maxine Linde Venture Fund, which enabled the purchase of the Hysitron<sup>TM</sup> Triboindenter used in this investigation.

## ABSTRACT

This study examines the accuracy of the extracted elastic properties using nanoindentation. Since the conventional method to extract these properties utilizes Sneddon's elastic solution, this study first considers indentations of linearly elastic solids for direct comparison. The study proposes a criterion for a converged specimen's geometry and modifies Sneddon's equation to account for the finite tip radius and specimen compressibility effects. A composite correction factor is derived to account for the violations of the underlying assumptions behind Sneddon's derivation. This factor is a function of indentation depth, and a critical depth is derived beyond which the finite tip radius effect will be insignificant. Techniques to identify the radius of curvature of the indenter and to decouple the elastic constants for linear elastic materials are proposed. Experimental results on nanoindentation of natural latex are reported and discussed in light of the proposed modified relation and techniques.

The second part of the study examines the accuracy of the extracted material properties in elastic-plastic nanoindentations. The study establishes that the accurate determination of the projected area of contact,  $A$ , is crucial. However, the conventional method to determine  $A$  is largely limited to elastic materials, hence a new electrical resistance method is proposed to measure  $A$  for elastic-plastic materials. With an accurate  $A$ , the error associated with the extracted elastic material properties is reduced by more than 50% in some cases. This error remains to be a function of the material's Poisson's ratio, which is identified to influence the amount of residual stresses at the plastic imprint.

Finally, this study examines the accuracy of the extracted material properties in the nanoindentation of soft materials using an Atomic Force Microscope (AFM). The effects of cantilever stiffness, preload, and surface interaction forces are observed to influence the measurements. Three set of experiments were performed to decouple these effects. The effect of a preload resembles a shift of nanoindentation load-displacement curve, while the cantilever stiffness is observed to have significant influence on the measurement of the surface forces. Lastly, a novel technique to account for these effects is proposed, in order to accurately extract the material properties of interest.

# TABLE OF CONTENTS

Acknowledgements.....	iv
Abstract.....	vi
Table of Contents.....	viii
Lists of Figures and Tables.....	x
Nomenclature.....	xiv
Chapter 1: Introduction.....	1
Chapter 2: An Analysis of Nanoindentation in Linearly Elastic Solids.....	11
2.1. Introduction.....	12
2.2. Conventional Extraction of Elastic Properties.....	16
2.3. Numerical Simulations.....	20
2.3.1. Sneddon’s Solution and a Rigid Indenter with a Finite Tip Radius.....	20
2.3.2. Converged Specimen Geometry.....	22
2.3.3. Finite Tip Radius Effect.....	27
2.4. Proposed Techniques and Modifications.....	35
2.4.1. Technique for Characterizing the Tip Radius of the Indenter.....	35
2.4.2. Methodology to Decouple the Measurements for Linear Elastic Constants, $E$ and $\nu$ .....	36
2.4.3. Quantifying Error Due to Finite Tip Radius and Specimen’s Compressibility.....	39
2.4.4. Sensitivity of the Load-Displacement Measurements to Finite Tip Radius Effect.....	43
2.5. Summary and Conclusions.....	47
Chapter 3: An Analysis of Nanoindentation in Elasto-Plastic Solids.....	55
3.1. Introduction.....	56
3.2. Conventional Extraction of Elastic Properties.....	59
3.3. Numerical Simulations.....	63
3.3.1. The Effective Half Angle, $\alpha'$ .....	63
3.3.2. The Relationship Between $h_e/h_{max}$ and $E/\sigma_y$ for Elastic, Perfectly Plastic Materials.....	65
3.3.3. Error Involved in the Conventional Derivation.....	68
3.3.4. Examination of the Underlying Assumptions.....	69
3.3.4.1. Does the unloading and subsequent reloading load-displacement follow the same path?.....	69
3.3.4.2. Validity of the ‘equivalent’ problem.....	71
3.3.5. The Straightforward Application of Sneddon’s Equation.....	73
3.3.6. Factors Affecting the Accuracy of the Stiffness Equation.....	75
3.3.6.1. Residual stresses at the plastic imprint.....	75
3.3.6.2. Accurate determination of $A$ .....	78
3.3.6.2.1. The contact depth, $h_c$ .....	78
3.3.6.2.2. Finite tip radius of the indenter.....	78
3.4. Proposed Technique.....	81
3.4.1. Measurement of the Projected Contact Area using Electrical Resistance Method.....	83
3.4.2. Reduction of Errors with Accurate Measurement of $A$ .....	84

3.5. Summary and Conclusions.....	90
Chapter 4: An Analysis of Nanoindentation in Soft Materials.....	104
4.1. Introduction.....	105
4.2. Effects that Affect the Accuracy of the Extracted Material Properties.....	108
4.2.1. Stiffness of the Cantilever.....	109
4.2.2. Tip-Specimen Contact Point.....	113
4.2.3. Surface Forces.....	114
4.3. Experiments.....	116
4.3.1. Indentation with a ‘Rigid Cantilever’ on a Soft Material with negligible Surface Forces.....	116
4.3.2. Indentation with a Compliant Cantilever on a Rigid Material with Surface Forces.....	121
4.3.3. Indentation with a Compliant Cantilever on a Soft Material with Surface Forces.....	127
4.3.3.1. Indentation with the soft cantilever.....	131
4.3.3.2. Indentation with a stiff cantilever.....	135
4.4. Summary and Conclusions.....	143
Chapter 5: Conclusions and Future Challenges.....	152

## LIST OF FIGURES AND TABLES

Fig. 2.1. Illustration of an indentation by a rigid cone into a linearly elastic solid.....	17
Fig. 2.2. (a) Geometry of indentation of a cylindrical specimen with a rigid conical indenter with finite tip radius; (b) The Mises equivalent stress field in the specimen during indentation at $h_{max} = 600 \text{ nm}$ .....	21
Fig. 2.3. Load-displacement measurements in the numerical experiment with a rigid indenter with a finite tip radius of $200 \text{ nm}$ compared with Sneddon's equation.....	22
Fig. 2.4. Non-unique load-displacement relationships for specimens with the same radius, $r_s$ , of $18 \mu\text{m}$ but different height, $h_s$ ( $18, 30, 40, 60, 92$ and $120 \mu\text{m}$ ).	24
Fig. 2.5. Load-displacement curves for specimens with $r_s = 30 \mu\text{m}$ and different aspect ratios, $r_s/h_s$ ( $0.3, 0.6, 1,$ and $2$ ). It can be observed that a unique curve was obtained when $r_s/h_s \geq 1$ , suggesting convergence.....	25
Fig. 2.6. Load-displacement curves for specimens with different $h_s/h_{max}$ . Insert shows a close-up view of the load-displacement curves at larger indentation depths for different $h_s/h_{max}$ ( $15, 30, 50, 100,$ and $150$ ).....	26
Fig. 2.7. Convergence study for different $h_{max}/h_s$ and $r_s/h_s$ .....	27
Fig. 2.8. Simulated load-displacement curves of identical elastic cylindrical specimens ( $E = 50 \text{ GPa}, \nu = 0.3$ ) indented with rigid conical indenters of different tip radii, $\rho$ ( $0, 30, 75, 120, 150,$ and $200 \text{ nm}$ ).....	29
Fig. 2.9. Multiplicative factor, $f(\nu)$ , as a function of Poisson's ratio, $\nu$ ( $R^2 = 0.9999$ ).	31
Fig. 2.10. Additive factor, $g(\rho)$ , vs. tip radius, $\rho$ ( $R^2 = 0.9977$ ).....	32
Fig. 2.11. Comparison of Hay's correction factor, $\zeta$ , and $f(\nu)$ .....	32
Fig. 2.12. Comparison of simulation results with proposed empirical curve fits for various material constants and tip radii of the rigid indenter.....	34
Fig. 2.13. Load-displacement curves for Hertz equation (15) and simulated indentations using spherical and conical indenters on identical specimens.....	38
Fig. 2.14. Percentage error in estimation of Young's modulus, $\varepsilon$ , vs. tip radius, $\rho$ , for $h_{max} = 100$ and $300 \text{ nm}$ .....	41
Fig. 2.15. Load-displacement measurement for the indentation of latex rubber.....	44

Fig. 2.16. Stress-strain relationship for natural latex from quasi-static uniaxial compression experiments.....	45
Fig. 2.17. Comparison of experimental results and predicted load-displacement relations for different $\rho$ (0 nm, 250 nm, 500 nm).....	46
Fig. 3.1. (a) Schematic of an indentation at full load and unload; (b) The corresponding load-displacement curve.....	59
Fig. 3.2. Illustration of the equivalent indentation problem.....	60
Fig. 3.3. Effective half-angle, $\alpha'$ , vs. $E/\sigma_y$ . Error bars represent spread of data for $\nu$ from 0.01 to 0.47.....	64
Fig. 3.4. $E/\sigma_y$ vs. $h_e/h_{max}$ for different materials.....	68
Fig. 3.5. Percentage error of $E$ , $\varepsilon$ vs. $E/\sigma_y$ , for different $\nu$ (0.01, 0.3, 0.47). The spread represents different indenter tip radius ranging between 30 nm and 150 nm.....	69
Fig. 3.6. Loading-reloading curves obtained from nanoindentation experiments on fused quartz (dash-dotted line) and single crystal aluminum (dotted line), and from numerical simulation with $E = 200 \text{ GPa}$ , $\sigma_y = 1 \text{ GPa}$ , $\nu = 0.3$ , and $\rho = 30 \text{ nm}$ (dashed line).....	71
Fig. 3.7. (a) Indentation of a notched specimen. (b) At $h_{max}$ the radius of contact is equal to the radius of the residual imprint.....	72
Fig. 3.8. Load-displacement curves for $\alpha' = 85^\circ$ and $89^\circ$ .....	73
Fig. 3.9. Comparison between the simulated unloading curve and the elastic reloading curves with calculated and 'ideal' $\alpha'$ 's.....	74
Fig. 3.10. (a) Profile of the residual imprint for $E/\sigma_y=10$ . (b) Profile of the residual imprint for $E/\sigma_y=1000$ . (Note the sink-ins and pile-ups.).....	75
Fig. 3.11. Residual equivalent (Mises) stress fields for indentations of elastic, perfectly plastic material with $E = 200 \text{ GPa}$ , $\sigma_y = 2 \text{ GPa}$ , and different $\nu$ ( $= 0.01, 0.3, \text{ and } 0.45$ , respectively).....	77
Fig. 3.12. Schematic of an elastic-plastic indentation.....	82
Fig. 3.13. (a) Load-displacement curves for the indentations of polycrystalline Gold (Au); (b) Corresponding current-displacement curves for the indentations	84

Fig. 3.14. $\varepsilon$ vs. $E/\sigma_y$ , using calculated and “measured” values for $A$ . The bars correspond to the calculated range of $\varepsilon$ for values of $\nu$ ( $= 0.01, 0.3, 0.47$ ) and $\rho$ ( $= 30\text{ nm}, 150\text{ nm}$ ).....	85
Fig. 3.15. $\varepsilon$ vs. $E/\sigma_y$ , using “measured” values for $A$ for $\rho = 30\text{ nm}$ and $150\text{ nm}$ . The bars correspond to the range of $\varepsilon$ for values of $\nu$ ( $= 0.01, 0.3, 0.47$ ).....	86
Fig. 3.16. $\varepsilon$ vs. $E/\sigma_y$ , using “measured” values for $A$ for $\nu$ ( $= 0.01, 0.3$ and $0.47$ ). The bars correspond to the range of $\varepsilon$ for values of $\rho$ ( $= 30\text{ nm}$ and $150\text{ nm}$ ).....	88
Fig. 3.17. Comparison between the correction factor, $f(\nu)$ , between elastic and elastic-plastic indentations.....	88
Fig. 4.1. Illustration for indentation with the AFM.....	109
Fig. 4.2. Indentation load, $P$ , vs. imposed approach distance, $\delta$ , for different cantilever stiffness, $k_c$ .....	111
Fig. 4.3. Cantilever deflection vs. imposed approach displacement, $\delta$ , for different cantilever stiffness, $k_c$ .....	112
Fig. 4.4. Indentation load, $P$ , vs. indentation displacement, $h$ , for different cantilever stiffness, $k_c$ .....	113
Fig. 4.5. Uniaxial true stress-strain curves for natural latex rubber.....	117
Fig. 4.6. Typical measured load-displacement nanoindentation curve for latex rubber using a Berkovich tip.....	118
Fig. 4.7. Comparison between experimental and theoretical load-displacement curves for the indentation of latex.....	121
Fig. 4.8. Deflection vs. imposed approach displacement for different cantilever stiffness. (Curves were deliberately offset for clarity.).....	122
Fig. 4.9. Graphical construction of an AFM force-displacement curve on a rigid specimen with surface forces.....	125
Fig. 4.10. Indentation force vs. imposed approach displacement for different cantilever stiffness. (Curves were deliberately offset for clarity.).....	127
Fig. 4.11. True stress-strain curves for polyacrylamide gel specimens cut from various locations of the Petri dish under uniaxial compression.....	129

Fig. 4.12. Comparison between indentation load-displacement curves for different cantilever stiffness with Hertz prediction.....	131
Fig. 4.13. Schematic of the numerical simulation.....	133
Fig. 4.14. Sketch of the shapes of the deformed cantilever at different stages of indentation. (The deformation was magnified 50 times.).....	134
Fig. 4.15. Indentation force vs. indentation depth from numerical simulations.....	135
Fig. 4.16. Idealized loading-unloading indentation load-displacement curve for soft material with surface forces.....	140
Fig. 4.17. Pull-off force, $P_{off}$ , vs. percentage square error, $\epsilon_s$ .....	140
Fig. 4.18. Experimental load-displacement curve plotted in relation to constructed JKR unloading curve with derived $P_{off}$ and $h_o$ .....	142
Table 3.1. Varying Poisson's ratio, $\nu$ , with $E = 50 \text{ GPa}$ and $\rho = 30 \text{ nm}$ .....	97
Table 3.2. Varying Young's modulus, $E$ , with $\nu = 0.3$ and $\rho = 30 \text{ nm}$ .....	98
Table 3.3. Varying Poisson's ratio, $\nu$ , with $E = 50 \text{ GPa}$ and $\rho = 150 \text{ nm}$ .....	99
Table 3.4. Varying Young's modulus, $E$ , with $\nu = 0.3$ and $\rho = 150 \text{ nm}$ .....	100
Table 3.5. Statistical variation for nanoindentation experiments.....	101
Table 3.6. Calculated $E$ with “measured” $A$ , for different $\nu$ , with $\rho = 30 \text{ nm}$ .....	102
Table 3.7. Calculated $E$ with “measured” $A$ , for different $\nu$ , with $\rho = 150 \text{ nm}$ .....	103

## NOMENCLATURE

$\alpha$	Half angle of the conical indenter
$\alpha'$	Half angle of the equivalent conical indenter
$\alpha^*$	Angle between indenter and residual imprint
$\beta$	Correction factor
$\gamma$	Surface energy per unit area per surface
$\delta$	Approach displacement
$\varepsilon$	Percentage error in Young's modulus
$\varepsilon_s$	Mean of the square of the difference between experimental and JKR curve normalized by the square of JKR curve
$\zeta$	Correction factor for compressible specimen
$\nu$	Poisson's ratio of the specimen
$\rho$	Tip radius
$\sigma_y$	Yield stress of the specimen
$\chi$	Coefficient determined by the indenter geometry
$a$	Contact radius
$A$	Projected area of contact
$A_s$	Surface area of contact
$C$	Constraint factor
$E$	Young's modulus of specimen
$E_c$	Young's modulus derived using conventional method
$E_r$	Reduced modulus

$h$	Indentation displacement/depth
$h_a$	Location of sphere-to-cone transition
$h_b$	Blunting distance
$h_c$	Contact depth
$h_e$	Elastic recoverable displacement
$h_{max}$	Maximum indentation depth
$h_o$	Indentation displacement due to preload
$h_r$	Residual displacement
$h_s$	Height of the specimen
$H$	Hardness of the specimen
$H_c$	Hardness derived using conventional method
$k_c$	Spring constant of the cantilever
$P$	Indentation load
$P_o$	Preload
$P_{off}$	Pull-off force
$r_s$	Radius of the specimen
$R$	Radius of the spherical indenter

## CHAPTER 1: INTRODUCTION

Indentation tests, also commonly known as hardness tests, were likely first developed by mineralogists (Tabor, 1951). The first documented semi-quantitative hardness test was developed by Mohs in 1822. Mohs established a measurement of hardness by ranking the ability of a material to scratch or be scratched by another material (Tabor, 1951). A subsequent development to the Mohs hardness measurement introduced the use of a diamond stylus to scratch the surface of the material of interest. The size of residual scratch imprint on the surface was measured to infer the hardness of the material. The scratch test however, was not suited for the hardness testing of metals, and the results are often complicated by the frictional properties of the surfaces.

In 1900, Brinell introduced the Brinell test (Tabor, 1951), which involved pushing a very hard spherical indenter (made of hard steel, tungsten carbide, or diamond) into the material of interest. The imprint was measured to derive the Brinell hardness number. In 1908, Meyer proposed the measure of hardness as the ratio of the load to the projected area of indentation, which is still the commonly accepted measure for hardness even today. In 1908 and 1925, Ludwik and Vickers hardness tests were introduced; this was when conical and pyramidal indenters were used in hardness tests. These indenter geometries are commonly used today.

The theoretical development for indentation of materials was first studied by Hertz (1881). More commonly known for his important contributions in the field of electromagnetism, Hertz, during the Christmas holiday in 1880, at the age of 23, developed the linear elastic solution for the contact between two spheres to account for

elastic deformation in his study of Newton's interference rings. His work immediately drew considerable attention to the contact mechanics community. Boussinesq (1885) then introduced the methods of potential theory to solve the contact problem between two linearly elastic isotropic solids. This proved to be an important milestone, as Sneddon took this method further, solving the contact problem first for a rigid conical indenter and a semi-infinite half plane (1948), and then for any arbitrary axisymmetric indenter and a semi-infinite half plane (1965).

The research interest in indentation tests became diverse by mid 20<sup>th</sup> century. Researchers examined various aspects of indentation tests such as plasticity (Dumas, 1971; Ford and Alexander, 1963; Hardy, 1972; Hill, 1950), frictional effects (Goodman, 1962; Grunzweig, 1954), viscoelastic and nonlinear elastic solids (Kuznetsov, 1962; Lee and Radok, 1960; Matthews, 1980; Radok, 1957; Yang, 1966) and adhesion (Bradley, 1932; Derjaguin, 1934; Derjaguin et al., 1975; Johnson et al., 1971; Maugis, 1991; Muller et al., 1980; Tabor, 1977). By early 1970s, depth-sensing indentation tests were developed (Bulychev et al., 1975; Loubet et al., 1984; Newey et al., 1982; Pethica et al., 1983; Ternoivskii et al., 1974). These researchers laid the foundation for the subsequent development of nanoindentation, when technological advancements reduced the size of the indenter tips and improved the accuracy and resolution of the depth and load measurements.

Indentation experiments had been traditionally used to measure hardness of a material, until Ternoivskii et al. (1974) introduced the stiffness equation to derive the reduced modulus (coupled term between the Young's modulus and Poisson's ratio) of interest using the measured load-displacement data. The stiffness equation is as follows

$$\frac{dP}{dh} = \frac{2}{\sqrt{\pi}} E_r \sqrt{A} \quad (1)$$

where  $dP/dh$  is the slope of the load-displacement curve,  $E_r$  is the reduced modulus for the material, and  $A$  is the projected contact area of the indent. In 1992, Oliver and Pharr popularized nanoindentation as a technique to extract elastic material properties for materials, by re-introducing the stiffness equation and demonstrating that this equation works for all axisymmetric indenters with any infinitely smooth profile (Oliver and Pharr, 1992; Pharr et al., 1992).

This technique proposed by Oliver and Pharr (1992) received wide acceptance by the community and is the built-in method to retrieve the reduced modulus information, for most modern commercial nanoindenters. This technique involves a number of simplifying assumptions, (i) the specimen is an infinite half-space, (ii) the indenter has an ideal geometry, (iii) the material is linearly elastic and incompressible, and (iv) there are no interaction surface forces during contact such as adhesive or frictional forces. With the advent of more efficient finite elements (FE) simulations and commercial codes, many researchers followed the footsteps of Hardy (1972) and Dumas (1971), who first used FE simulations to study the indentation problem. Some of the work published by researchers examining the indentation problem using FE simulations include — on spherical indenter (Hill et al., 1989; Kral et al., 1993; Storåkers and Larsson, 1994); on conical indenter (Laursen and Simo, 1992); on pyramidal indenters (Giannakopoulos et al., 1994; Larsson and Giannakopoulos, 1996); on the effects of plasticity (Cheng and Cheng, 1999; Pharr and Bolshakov, 2002); on the forward-reverse analysis in nanoindentation (Chen et al., 2007; Dao et al., 2001).

Practical indentations are likely to deviate from the assumptions cited above used in deriving the stiffness equation (Eq. (1)). Any deviations of the extracted elastic properties using nanoindentation from the ones obtained using traditional material characterization techniques, such as the uniaxial tests, are commonly accounted for using a correction factor. This correction factor is commonly derived using two approaches, the phenomenological approach and the mechanistic approach. Using the phenomenological approach, researchers often establish a composite correction factor by comparing the macroscopic material properties obtained using traditional characterization techniques with those obtained using nanoindentation for different classes of materials such as polymers, metals, and ceramics, etc. (Tranchida et al., 2006). This composite correction factor takes into account all the factors that violate the stringent criteria for the stiffness equation. Unfortunately, this approach does not provide an insight to the makeup of the correction factor by different factors, nor does it reflect how the factors affect one another.

In using the mechanistic approach, researchers often isolate one single factor that violates the criteria for the use of the stiffness equation. Using this approach, researchers are able to gain tremendous insight about this isolated factor. For example, in the compressibility of the specimen when  $\nu < 0.5$  — which results in a lateral displacement during indentation, neglected in Sneddon's derivation (Hay et al., 1999) — researchers were able to derive a close form expression for the correction factor that relates to the Poisson's ratio,  $\nu$ . However, using this approach, it is often not clear if this correction factor for a violation of one criterion is applicable to practical indentations that include violations of other criteria as well, i.e., can this factor, derived under linear elastic conditions, be used in elastic-plastic indentations? And, how do different correction

factors relate to each other to form the effective correction factor for each nanoindentation experiment?

The objective of this thesis is to first investigate the effects of some of the most common violations of the assumptions required for the accurate use of the stiffness equation (Eq. (1)) such as finite tip radius, finite specimen geometry, compressible specimen, plasticity, and surface forces. This thesis will also examine the relationship between some of these violations that form the composite correction factor during the indentation of simple solids such as isotropic linearly elastic solids and isotropic elastic, perfectly plastic solids. Finally, this study aims to identify the crucial factors affecting the accuracy of the extracted material properties for indentations under various conditions, and to propose novel techniques to account for these factors. The last part of this study will also consider some additional challenges to extract material properties through nanoindentation of soft materials using an Atomic Force Microscope (AFM). This thesis will be organized into three main chapters: Chapter 2 — an analysis of nanoindentation in linearly elastic solids; Chapter 3 — an analysis of nanoindentation in elasto-plastic solids; and Chapter 4 — an analysis of nanoindentation in soft materials. This thesis will conclude with a brief summary and discussion for future challenges in the final chapter.

## REFERENCES

- Boussinesq, J., 1885. Applications des Potentials a l'Etude de l'Equilibre et du Mouvement des Solides Elastiques. Gauthier-Villars.
- Bradley, R.S., 1932. The Cohesive Force between Solid Surfaces and the Surface Energy of Solids. *Philos. Mag.* 13 (86), 853–862.
- Bulychev, S.I., Alekhin, V.P., Shorshorov, M.K., Ternovskii, A.P., Shnyrev, G.D., 1975. Determining Young's Modulus from the Indentor Penetration Diagram. *Zavodskaya Laboratoriya* 41 (9), 1137–1140.
- Chen, X., Ogasawara, N., Zhao, M., Chiba, N., 2007. On the uniqueness of measuring elastoplastic properties from indentation: The indistinguishable mystical materials. *J. Mech. Phys. Solids* 55, 1618–1660.
- Cheng, Y.T., Cheng, C.M., 1999. Scaling Relationships in Conical Indentation of Elastic Perfectly Plastic Solids. *Int. J. Solids Structures* 36, 1231–1243.
- Dao, M., Chollacoop, N., Vliet, K.J.V., Venkatesh, T.A., Suresh, S., 2001. Computational Modeling of the Forward and Reverse Problems in Instrumented Sharp Indentation. *Acta Materialia* 49, 3899–3918.
- Derjaguin, B.V., 1934. Analysis of Friction and Adhesion IV: The Theory of the Adhesion of Small Particles. *Koll.-Zeit.* 69 (2), 155–164.
- Derjaguin, B.V., Muller, V.M., Toporov, Y.P., 1975. Effect of Contact Deformations on Adhesion of Particles. *J. Coll. Interface Sci.* 53 (2), 314–326.

Dumas, G., 1971. Elastoplastic Indentation of a Half-Space by an Infinitely Long Rigid Circular Cylinder. *Int. J. Mech. Sci.* 13 (6), 519.

Ford, H., Alexander, J.M., 1963. *Advanced Mechanics of Materials*. Longmans, London.

Giannakopoulos, A.E., Larsson, P.L., Vestergaard, R., 1994. Analysis of Vickers Indentation. *Int. J. Solids Structures* 31, 2679–2708.

Goodman, L.E., 1962. Contact Stress Analysis of Normally Loaded Rough Sphere. *Trans. ASME, Series E, J. Appl. Mech.* 29, 515.

Grunzweig, J., 1954. Calculations and Measurements on Wedge-Indentation. *J. Mech. Phys. Solids* 2 (2), 81–86.

Hardy, C., 1972. Indentation of an Elastic-Perfectly-Plastic Half-Space by a Hard Sphere. *J. Basic Eng.* 94 (1), 251.

Hay, J.C., Bolshakov, A., Pharr, G.M., 1999. A Critical Examination of the Fundamental Relations Used in the Analysis of Nanoindentation Data. *J. Mater. Res.* 14, 2296–2305.

Hertz, H., 1881. *Über Die Berührung Fester Elastischer Körper (On the Contact of Elastic Solids)*. *J. Reine Angew. Math.*, 156–171.

Hill, R., 1950. *The Mathematical Theory of Plasticity*. Oxford University Press, London.

Hill, R., Storåkers, B., Zdunek, A.B., 1989. A Theoretical Study of the Brinell Hardness Test. *Proc. R. Soc. Lond.* A423, 301–330.

- Johnson, K.L., Kendall, K., Roberts, A.D., 1971. Surface Energy and the Contact of Elastic Solids. *Proc. R. Soc. Lond. A, Math. Phys. Sci.* 324 (1558), 301–313.
- Kral, E.R., Komvopoulos, K., Bogy, D.B., 1993. Elastic-Plastic Finite Element Analysis of Repeated Indentation of a Half-Space by a Rigid Sphere. *J. Appl. Mech.* 75, 829–841.
- Kuznetsov, A.I., 1962. Penetration of Rigid Dies into a Half-Space with Power-Law Strain Hardening and Nonlinear Creep. *J. Appl. Math. Mech.* 26, 717.
- Larsson, P.L., Giannakopoulos, A.E., 1996. Analysis of Berkovich Indentation. *Int. J. Solids Structures* 33 (2), 221–248.
- Laursen, T.A., Simo, J.C., 1992. A Study of the Mechanics of Microindentation Using Finite Elements. *J. Mater. Res.* 7, 616–618.
- Lee, P.H., Radok, J.R.M., 1960. The Contact Problem for Viscoelastic Bodies. *Trans. ASME, Series E, J. Appl. Mech.* 27, 438.
- Loubet, J.L., Georges, J.M., Marchesini, O., Meille, G., 1984. Vickers Indentation Curves of Magnesium Oxide {MgO}. *J. Tribol-T ASME* 106, 43–48.
- Matthews, J.R., 1980. Indentation Hardness and Hot Pressing. *Acta Metall.* 28 (3), 311–318.
- Maugis, D., 1991. Adhesion of Spheres: The JKR-DMT Transition Using a Dugale Model. *J. Coll. Interface Sci.* 150 (1), 243–269.

Muller, V.M., Yushchenko, V.S., Derjaguin, B.V., 1980. On the Influence of Molecular Forces on the Deformation of an Elastic Sphere and its Sticking to a Rigid Plane. *J. Coll. Interface Sci.* 77 (1), 91–101.

Newey, D., Wilkins, M.A., Pollock, H.M., 1982. An Ultra-Low-Load Penetration Hardness Tester. *J. Phys. E: Sci. Instrum.* 15, 119–122.

Oliver, W.C., Pharr, G.M., 1992. An Improved Technique for Determining Hardness and Elastic Modulus Using Load and Displacement Sensing Indentation Experiments. *J. Mater. Res.* 7, 1564–1583.

Pethica, J.B., Hutchings, R., Oliver, W.C., 1983. Hardness Measurement at Penetration Depths as Small as 20 Nm. *Philos. Mag. A* 48, 593–606.

Pharr, G.M., Bolshakov, A., 2002. Understanding Nanoindentation Unloading Curves. *J. Mater. Res.* 17, 2660–2671.

Pharr, G.M., Oliver, W.C., Brotzen, F.R., 1992. On the Generality of the Relationship Among Contact Stiffness, Contact Area, and the Elastic Modulus During Indentation. *J. Mater. Res.* 7 (3), 613–617.

Radok, J.R.M., 1957. Viscoelastic Stress Analysis. *Q. Appl. Math* 15, 198.

Sneddon, I.N., 1948. Boussinesq's Problem for a Rigid Cone. *Proc. Cambridge Philos. Soc.*, 492–507.

Sneddon, I.N., 1965. The Relation Between Load and Penetration in the Axisymmetric Boussinesq Problem for a Punch of Arbitrary Profile. *Int. J. Engng. Sci.* 3, 47–57.

Storåkers, B., Larsson, P.L., 1994. On Brinell and Boussinesq Indentation of Creeping Solids. *J. Mech. Phys. Solids* 42, 307–332.

Tabor, D., 1951. *The Hardness of Metals*. Oxford University Press, Cambridge, Great Britain.

Tabor, D., 1977. Surface Forces and Surface Interactions. *J. Coll. Interface Sci.* 58 (1), 2–13.

Ternovskii, A.P., Alekhin, V.P., Shorshorov, M.K., Khrushchov, M.M., Skvortsov, V.N., 1974. Micromechanical Testing of Materials by Depression. *Zavodskaya Laboratoriya* 39 (10), 1242–1247.

Tranchida, D., Piccarolo, S., Loos, J., Alexeev, A., 2006. Accurately evaluating Young's modulus of polymers through nanoindentations: A phenomenological correction factor to Oliver and Pharr procedure. *Appl. Phys. Lett* 89, 171901–171905.

Yang, W.H., 1966. The Contact Problem for Viscoelastic bodies. *Trans. ASME, Series E, J. Appl. Mech.* 33, 395.

## CHAPTER 2: AN ANALYSIS OF NANOINDENTATION IN LINEARLY ELASTIC SOLIDS

### ABSTRACT

The conventional method to extract elastic properties in the nanoindentation of linearly elastic solids relies primarily on Sneddon's solution (1948). The underlying assumptions behind Sneddon's derivation, namely (i) an infinitely large specimen and (ii) an infinitely sharp indenter tip, are generally violated in nanoindentation. As such, correction factors are commonly introduced to achieve accurate measurements. However, little is known regarding the relationship between the correction factors and how they affect the overall accuracy. This study first proposes a criterion for the specimen's geometry to comply with the first assumption, and modifies Sneddon's elastic relation to account for the finite tip radius effect. The relationship between the finite tip radius and compressibility of the specimen is then examined and a composite correction factor that involves both factors, derived. The correction factor is found to be a function of indentation depth and a critical depth is derived, beyond which the arbitrary finite tip radius effect is insignificant. Techniques to identify the radius of curvature of the indenter and to decouple the elastic constants ( $E$  and  $\nu$ ) for linear elastic materials are proposed. Finally, experimental results on nanoindentation of natural latex are reported and discussed in light of the proposed modified relation and techniques.

## 2.1. INTRODUCTION

Nanoindentation has become an increasingly popular mechanical characterization technique in the last decade. In addition to measuring the hardness value, the depth-sensing indentation has been routinely used to extract the elastic properties of the specimen, with known indenter geometry and material properties. Nanoindentation was developed in the early 1970s (Bulychev et al., 1975; Loubet et al., 1984; Newey et al., 1982; Pethica et al., 1983; Ternovskii et al., 1974). The technological developments have reduced the size of tips manufactured, and improved the accuracy and resolution of depth and load measurement of the indentation test, which has spurred the development of commercial nanoindenters. Their popularity is primarily due to the increased interest in thin films and specimens with small volumes, as motivated by modern applications, e.g., thin films, microelectronics, MEMS, biomaterials, etc. In addition, nano characterization instruments such as the Atomic Force Microscope (AFM) are being widely used for performing nanoindentation on a wide range of materials (e.g., Bhushan and Koinkar, 1994; Dimitriadis et al., 2002; VanLandingham et al., 2001). When compared to other methods of mechanical testing in the sub-micron range, nanoindentation has a relatively simple setup and specimen preparation. Furthermore, nanoindentation leaves a small imprint and is commonly perceived as relatively non-destructive.

The indentation problem has been studied for over a century, beginning with Hertz's pioneering contribution on the contact between elastic bodies (Hertz, 1881). Boussinesq (1885) subsequently studied the contact problem between two linearly elastic isotropic solids using methods of potential theory, which proved to be a significant

milestone to the understanding of the indentation problem. Sneddon used the approach taken by Bousinesq to derive the load-displacement relationship for a rigid cone indenter (1948), and subsequently derived it for an arbitrary indenter that is a body of revolution (1965). However, the analytical solutions were derived with stringent assumptions — (i) the specimen is an infinite half-space, (ii) the indenter has an ideal geometry with known parameters (perfect cone, sphere, etc.), and (iii) the material is linearly elastic. These assumptions limit the application of these solutions to many problems of practical interest. However, with the advent of finite element simulations and commercial codes, researchers now have a new tool to investigate the indentation problem, e.g., on spherical indenters (Hill, 1989; Kral, 1993; and Storåkers, 1994); on conical indenters (Laursen and Simo, 1992); on pyramidal indenters (Giannakopoulos, 1994; and Larsson, 1996); on effects of plasticity (Pharr et al., 2002; and Cheng and Cheng, 1999); and on forward-reverse analysis in nanoindentation (Dao et al., 2001; and Chen et al., 2007).

Pyramidal indenters (three-sided Berkovich and four-sided Vickers) are commonly used in indentation tests. These indenters are commonly treated as conical indenters with equivalent half angle  $\alpha$ , that gives the same area-to-depth relationship as the pyramidal indenter in question (Fischer-Cripps, 2004; Lichinchi et al., 1998; Oliver and Pharr, 1992; Wang et al., 2006; Yu et al., 2004).

The conventional procedure to derive the elastic properties during an indentation experiment was first proposed by Oliver and Pharr (1992), who made use of Sneddon's solution to retrieve the reduced modulus,  $E_r$ . Due to the stringent assumptions made in Sneddon's theoretical derivation as discussed previously, a correction factor is often

introduced to achieve accurate results. The correction factor is commonly derived using two approaches, (i) phenomenological approach and (ii) mechanistic approach. Using the phenomenological approach, researchers establish a composite correction factor by comparing the macroscopic material properties obtained using traditional characterization techniques, such as uniaxial test, with those obtained using nanoindentation for different classes of materials such as polymers, metals, and ceramics, etc. (Tranchida et al., 2006). This composite correction factor obtained takes into account all the factors that violate the assumptions in the theoretical derivations, however, this approach does not provide insight to the makeup of the correction factor by different factors, nor does it show how the factors affect one another. For the mechanistic approach, researchers often isolate one individual factor not considered in the theoretical derivation. Using this approach, researchers are able to gain tremendous insight about this isolated factor. For example, in the compressibility of the specimen when  $\nu < 0.5$  — which results in a lateral displacement during indentation, neglected in Sneddon's derivation (Hay et al., 1999) — researchers were able to derive a close form expression for the correction factor that relates to the Poisson's ratio,  $\nu$ . However, it is often not clear if this correction factor is applicable to practical indentations that commonly involve other factors as well, i.e., can this factor derived under linear elastic conditions be used in elastic-plastic indentations? And, how do different correction factors relate to each other to form the effective correction factor for the nanoindentation experiment?

This chapter first critically examines the various assumptions used in conventional technique to extract elastic material properties for nanoindentation experiments, using numerical finite element calculations. The various sources of

deviation from theoretical assumptions, such as the finite tip radius and the lateral displacement at the indentation, will be examined carefully. The conventional procedure for extracting the reduced modulus is briefly reviewed in Section 2.2. Results regarding the validity of the various assumptions discussed earlier are presented in Section 2.3. New methodologies and techniques accounting for the errors associated with conventional indentation of isotropic linearly elastic solids are described in Section 2.4. The composite correction factor that involves finite tip radius and compressibility of the specimen is presented in close form, and the significance of each factor will be discussed in detail. Results from nanoindentation experiments on a nominally elastic solid (natural latex) are used to illustrate the application of the suggested techniques for accurate evaluation of material properties. A summary and conclusions of the study are presented in Section 2.5.

## 2.2. CONVENTIONAL EXTRACTION OF ELASTIC PROPERTIES

By assuming a linearly elastic half-space and rigid conical indenter, Sneddon (1948) found that

$$P = \frac{2 E \tan \alpha}{\pi (1 - \nu^2)} h^2 \quad (1)$$

where  $P$  is the load measured by the indenter,  $E$  and  $\nu$  are the Young's modulus and Poisson's ratio of the material that is being indented,  $\alpha$  is the half angle of the indenter, and  $h$  is the penetration depth by the indenter. While the validity of Sneddon's solution is limited to linearly elastic indentations, Eq. (1) is nonetheless routinely applied to elastic-plastic indentations by assuming that the initial unloading segment of the load-displacement curve is linearly elastic. In an elastic indentation where the loading and unloading curves follow the same path, Eq. (1) and subsequent derivations should be valid at all  $h$ .

Differentiating (1) with respect to  $h$ , the slope of the load-displacement curve is given by,

$$\frac{dP}{dh} = \frac{4 E \tan \alpha}{\pi (1 - \nu^2)} h \quad (2)$$

and with further algebraic manipulation (Fischer-Cripps, 2004),

$$\frac{dP}{dh} = \frac{2 \sqrt{A} E}{\sqrt{\pi} (1 - \nu^2)} \quad (3)$$

where  $A$  is the projected area of contact of the indenter. Bulychev et al. (1975) showed that (3) also holds for cylindrical punch and spherical indenters. Subsequently, Pharr et al. (1992) showed that (3) is relevant for all axisymmetric indenters with infinitely

differentiable profile. For a Berkovich/Vickers indenters, the angle  $\alpha = 70.3^\circ$ , and the corresponding projected area,  $A$  is given by,

$$A = \pi \tan^2 \alpha h_c^2 \quad (4)$$

where  $h_c$  refers to the contact depth (Fig. 2.1) and is given by (Fischer-Cripps, 2004),

$$h_c = h - \frac{2(\pi - 2)}{\pi} \frac{P}{dP/dh} . \quad (5)$$

Note that the coefficient of the second term on the right-hand side of (5) can be replaced by  $\chi$ , whose value is dependent on the geometry of the indenter (Pharr and Bolshakov, 2002).

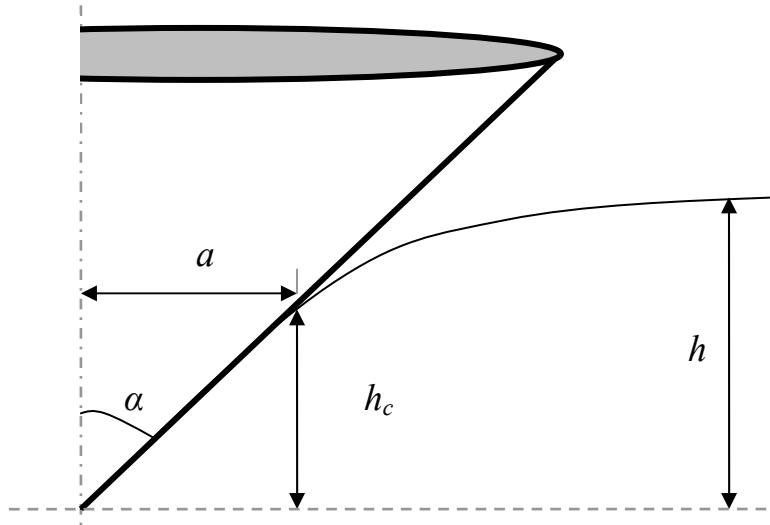


Fig. 2.1. Illustration of an indentation by a rigid cone into a linearly elastic solid

Thus, using the load-displacement curve measured during an indentation, one can obtain the elastic constants of the specimen of interest by rearranging (3) to obtain the stiffness equation given by

$$\frac{E}{(1 - \nu^2)} = \frac{1}{2\beta} \sqrt{\frac{\pi}{A}} \frac{dP}{dh} \quad (6)$$

where  $\beta$  is a non-dimensional correction factor to account for deviations from the original stiffness equation. The factor  $\beta$  is used to account for the treatment of a pyramidal indenter as an equivalent conical indenter —  $\beta$  is unity for axisymmetric indenters and close to unity for pyramidal ones —  $\beta = 1.012$  for square-based indenter, e.g., Vickers, and  $\beta = 1.034$  for a triangular punch, e.g., Berkovich (King, 1987). However, these results are debatable, as Woirgard (2006) demonstrated analytically that  $\beta = 1.061$  and  $\beta = 1.023$  for triangular and square-based indenters, respectively. Hay et al. (1999) considered the elastic radial displacement neglected in Sneddon's formulation and proposed a correction factor that is a function of the indenter's half angle,  $\alpha$  and Poisson's ratio,  $\nu$ . In addition, the correction factor  $\beta$  is also used to account for finite tip radius effect as found in the works of Troyon et al. (2004). The deviation of a pyramidal indenter from a conical one is not relevant to this paper since only the conical indenter is considered. Furthermore, since the objective of this paper is to investigate the applicability of Sneddon's equation on nanoindentation,  $\beta$  is deliberately chosen to be one, so as not to introduce artificial effects into the analysis.

The right-hand side of (6) consists of terms that can be derived using the load-displacement measurements in an indentation experiment. Thus, using this relationship, the term on the left-hand side of the equation consisting of both  $E$  and  $\nu$ , commonly referred to as the reduced modulus,  $E_r$ , can be evaluated. It is important to note that the elastic constants,  $E$  and  $\nu$ , evaluated using this procedure are coupled and thus require *a priori* knowledge of one of them to calculate the other. Also note that when the indenter is not considered as rigid, the reduced modulus,  $E_r$  is given by,

$$\frac{1}{E_r} = \frac{(1 - \nu^2_{specimen})}{E_{specimen}} + \frac{(1 - \nu^2_{indenter})}{E_{indenter}}. \quad (7)$$

The load-displacement relationship derived by Sneddon (1948), given by (1), assumed the specimen as a linearly elastic infinite half space and a conical indenter that is infinitely sharp. While these assumptions simplified the problem, it is important to note that it is virtually impossible to fulfill them in reality. In an experiment, the specimen to be tested is likely to have a finite geometry and so does the radius of curvature of the indenter. Any deviations from the assumptions made in the derivation of Sneddon's solution will be inevitably transferred as errors to the extracted elastic constants.

The goal of this study is to identify the effects of the above-mentioned deviations from the assumptions used in Sneddon's derivation (1948), and quantify the error associated with the calculation of elastic constants using the conventional method proposed by Oliver and Pharr (1992). This paper considers a Berkovich equivalent conical indenter ( $\alpha = 70.3^\circ$ ) for which there is an available analytical solution (given by (1)). The elastic properties will be derived using (6) with  $\beta = 1$ .

## 2.3. NUMERICAL SIMULATIONS

### 2.3.1. Sneddon's Solution and a Rigid Indenter with a Finite Tip Radius

Numerical 'experiments' were performed using the commercial numerical finite element package, ABAQUS. A cylindrical specimen with a radius,  $r_s$ , of  $18 \mu m$  and a height,  $h_s$ , of  $30 \mu m$ , was indented on its top surface, along the axis of symmetry. The cylindrical specimen was modeled as an isotropic deformable solid with  $E = 70 \text{ GPa}$  and  $\nu = 0.3$ . Figure 2.2(a) is a three-dimensional illustration of the numerical simulation performed. The conical indenter was modeled as analytically rigid, with a finite tip radius,  $\rho$ , of  $200 \text{ nm}$ , and was indented into the specimen to a maximum depth,  $h_{max}$ , of  $600 \text{ nm}$  (displacement control). Details of the simulation will be included in the following section.

Figure 2.2(b) shows a snapshot of the Mises equivalent stress field in the specimen when the indenter is at  $h_{max} = 600 \text{ nm}$ . The region with highest stress is directly beneath the indenter tip. The boundary of the high-stress region defined by the outlined area in Fig. 2.2(b) has an equivalent stress larger than or equal to  $3.9 \text{ GPa}$ . This region has a width of  $2.1 \mu m$  and a maximum depth of  $3.3 \mu m$ . This high-stress region is located reasonably far away from the boundaries. The height and width of the area of high stress is close to 10 times smaller than that of the specimen and there is no visible interaction of the stress field with the boundaries of the specimen, which suggests that the specimen can be considered as sufficiently large for practical purposes.

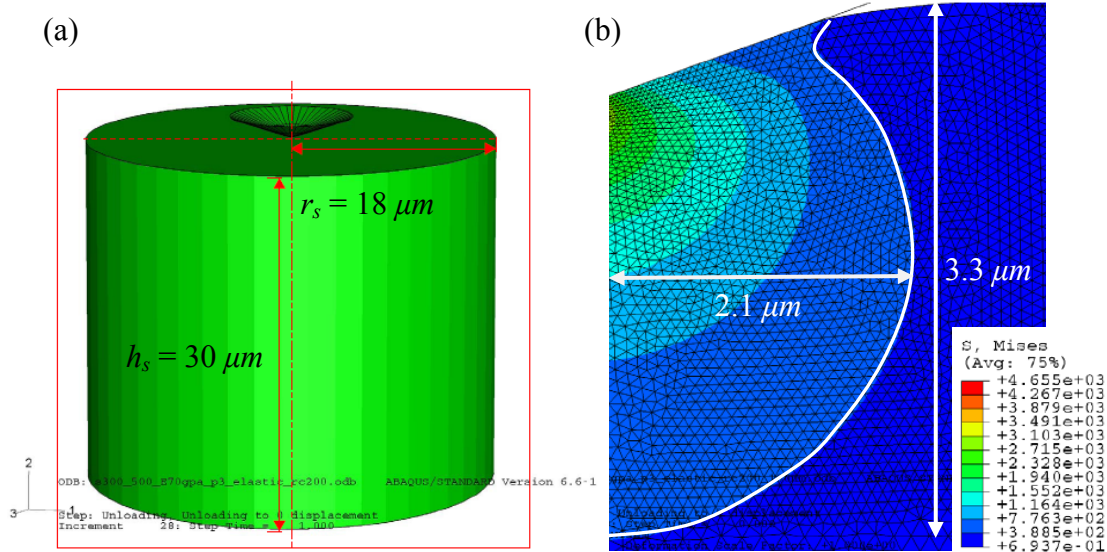


Fig. 2.2. (a) Geometry of indentation of a cylindrical specimen with a rigid conical indenter with finite tip radius; (b) The Mises equivalent stress field in the specimen during indentation at  $h_{max} = 600 \text{ nm}$ . (Note that the stress values must be multiplied by a factor of  $1e7$  to respect the scale of the problem.)

The load-displacement ( $P - h$ ) curves from the numerical simulations are plotted in Fig. 2.3. The continuous solid curve refers to the load-displacement relationship for both the loading and unloading paths (loading and unloading paths coincide since the specimen was modeled as linear elastic) obtained from the simulation, while the dashed curve shows the load-displacement relationship derived from Sneddon, Eq. (1). It can be seen that the two curves are distinctly different. Using the conventional derivation described previously, while assuming that the Poisson's ratio was known *a priori* to be 0.3, the Young's modulus was found to be  $77 \text{ GPa}$ , which is quite different from the value used in the simulation ( $70 \text{ GPa}$ ). This difference motivated the present study in order to first understand the effect of deviations from Sneddon's assumptions, and then to quantify and to correct for the errors associated with them, so as to obtain reliable values of the reduced modulus from experimental measurements.

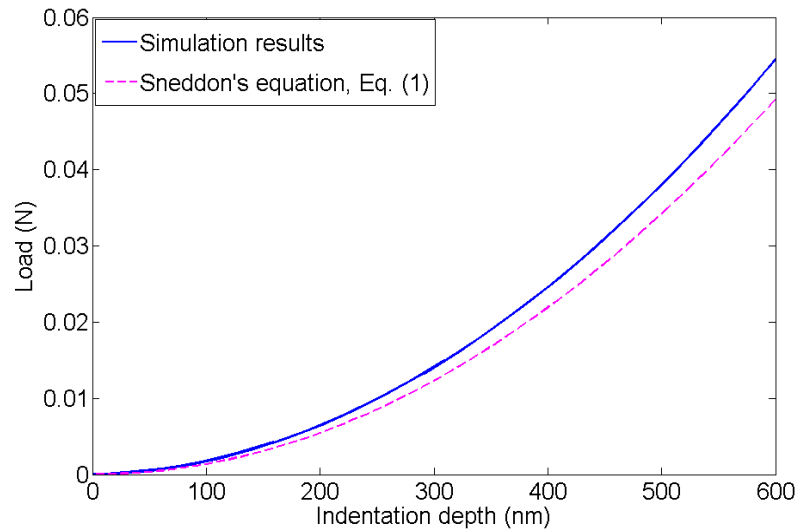


Fig. 2.3. Load-displacement measurements in the numerical experiment with a rigid indenter with a finite tip radius of 200 nm compared with Sneddon's Eq. (1)

### 2.3.2. Converged Specimen Geometry

It has been noted that the geometry of the specimen affects the values of measured load and displacement significantly (Dimitriadis et al., 2002). This is not surprising — consider two specimens loaded uniaxially (load control) with identical uniform stress and strain fields; the displacements of the specimens are not unique but functions of their geometries (i.e., length). This is also true for the measured load in a displacement-controlled experiment.

Numerical simulations were performed to investigate the indentation problem, using the commercial finite element software, ABAQUS. The indentation experiment was modeled as a 2-dimensional axisymmetric problem using a total of 5006 three-node linear axisymmetric triangular elements (CAX3) for a specimen with a geometry  $r_s/h_s$  equals unity and  $h_s/h_{max}$  equals 100 (the actual physical size of the specimen is irrelevant as the simulations are scaled to the indentation depth). The number of nodes used for

individual specimens was scaled up and down for changes in their respective dimensions with respect to indentation depth. A more refined mesh by doubling the number of elements was used for each specimen size but did not yield significantly different results ( $< 1\%$  difference for the range of indentation depth of interest) for each simulation, which suggests convergence of the existing mesh. The mesh is denser at the indentation site and less dense away from the indentation to minimize computational time. In order to isolate the effects of finite specimen size and finite tip radius of the indenters, the simulations were performed using conical indenters with the identical arbitrary tip radius; in addition, friction was also excluded in the contact between the indenter and the specimen. The indenter was also pushed to a maximum indentation depth,  $h_{max}$ , that is much larger than the radius of curvature of the tip,  $\rho$ , in order to minimize any tip-geometry-transition effect — the conical tip is rounded off by a tangent sphere, whose radius gives the radius of curvature of the tip.

Elastic specimens with identical material constants ( $E = 70 \text{ GPa}$  and  $\nu = 0.3$ ) and radius,  $r_s$  ( $18 \mu\text{m}$ ) but different height,  $h_s$  (see Fig. 2(a)) were indented to the same maximum indentation depth,  $h_{max}$  ( $600 \text{ nm}$ ) in the numerical experiments performed. Figure 2.4 shows the load-displacement relationship (both loading and unloading) of each specimen recorded during the simulations. It is observed that a thinner specimen resulted in a higher load measurement for a given displacement or equivalently, at a given load, a smaller displacement. Despite having identical material properties, the specimens with different height,  $h_s$ , have distinctly different load-displacement curves. The first observation is that these differences will inevitably be passed on to the value of the reduced modulus evaluated using the conventional method discussed in the previous

section. Dimitriadis et al. (2002) considered the problem of spherical indentation and corrected for the specimen thickness effect on the load-displacement relation.

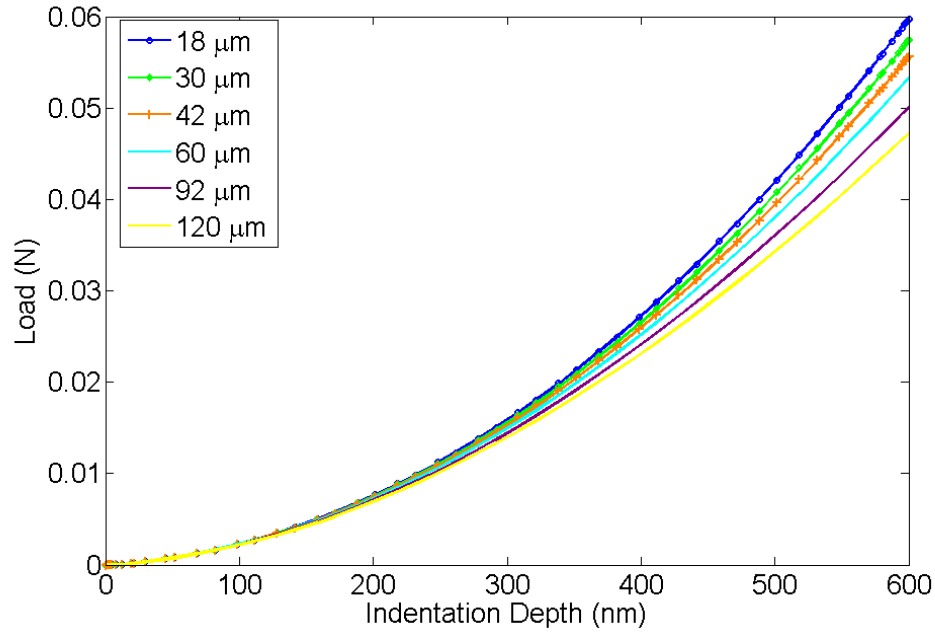


Fig. 2.4. Non-unique load-displacement relationships for specimens with the same radius,  $r_s$ , of  $18 \mu m$  but different height,  $h_s$  ( $18, 30, 40, 60, 92$ , and  $120 \mu m$ )

Keeping  $h_s$  at  $30 \mu m$ , the radius of the specimens,  $r_s$  was varied from  $9 \mu m$  to  $60 \mu m$ . The specimens were indented with the same indenter to the same maximum depth of  $600 nm$ . From Fig. 2.5, it can be observed that the load-displacement curves converge when the aspect ratio,  $r_s/h_s$  equals or exceeds unity. The validity of converged aspect ratio was checked and confirmed for other values of  $h_s$  as well.

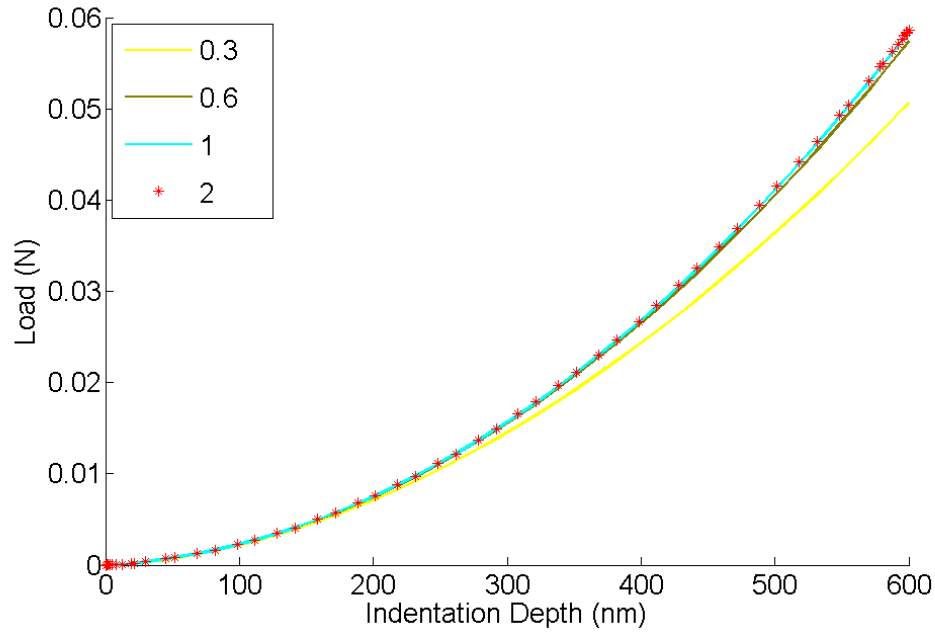


Fig. 2.5. Load-displacement curves for specimens with  $r_s = 30 \mu\text{m}$  and different aspect ratios,  $r_s/h_s$  (0.3, 0.6, 1, and 2). It can be observed that a unique curve was obtained when  $r_s/h_s \geq 1$ , suggesting convergence

Specimens with converged aspect ratio, but different  $h_s/h_{max}$ , were used in subsequent simulations to determine the minimum size of the specimens to achieve convergence. Figure 2.6 plots their corresponding calculated load-displacement curves. It is observed that the load-displacement curves ‘converge’ — i.e., load difference  $< 100 \mu\text{N}$  (which is approximately 1% of the maximum load for the nanoindenter) when the  $h_s/h_{max}$  equals or exceeds 100. From here on, converged specimen geometry will be defined as:

$$\frac{r_s}{h_s} \geq 1$$

and

$$\frac{h_s}{h_{max}} \geq 100 . \quad (8)$$

To save computation time, it is favorable to keep the specimen as small as possible, hence converged specimen geometry is defined as  $r_s/h_s$  equals unity and  $h_s/h_{max}$  equals 100.

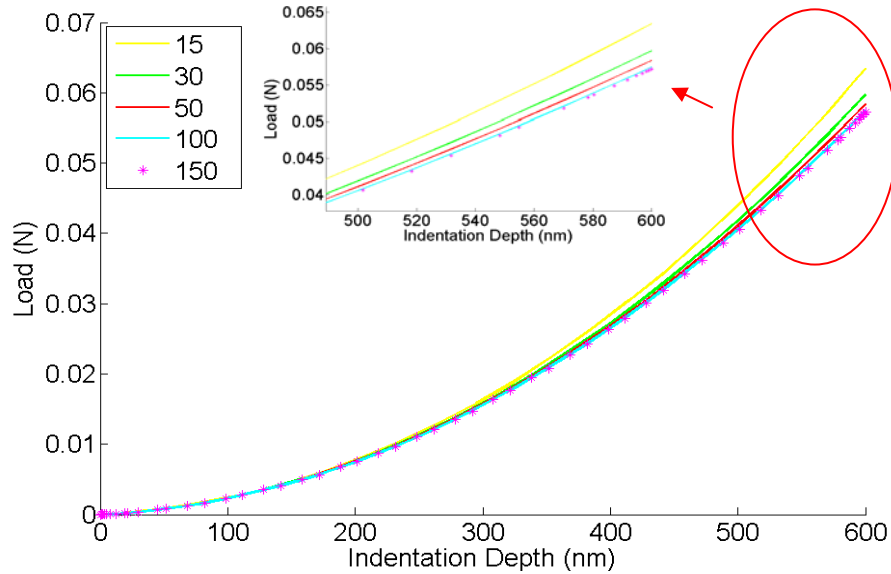


Fig. 2.6. Load-displacement curves for specimens with different  $h_s/h_{max}$ . Insert shows a close-up view of the load-displacement curves at larger indentation depths for different  $h_s/h_{max}$  (15, 30, 50, 100, and 150)

There is a general ‘rule of thumb’ which suggests that convergence is achieved when  $h_s/h_{max}$  is larger than 10 (Fischer-Cripps, 2004). Figure 2.2(b) shows that the depth of high-stress region is about five times that of  $h_{max}$ , all of which may seem to suggest that (8) may be too stringent. However, as shown in Fig. 2.7, *both* criteria shown in (8) have to be fulfilled in order to achieve convergence.

Figure 2.7 shows an enlarged view of a segment of the load-displacement curves. As discussed previously, it is observed that for a given  $h_s/h_{max}$ , the curves converge when  $r_s/h_s > 1$ . It is also observed that for an ‘unconverged’ aspect ratio, i.e.,  $r_s/h_s < 1$ , convergence in the ‘ $h_{max}/h_s$  sense’ occurs much earlier. As seen in Fig. 2.7, for  $r_s/h_s$  of 1/2,

the load-displacement curves for  $h_s/h_{max}$  of 25 to 150 coincide. However, one should note that this is a “pseudo-convergence” — a slight change in the aspect ratio of the specimen will result in a significant change in the load-displacement curves. This “pseudo-convergence” could occur for an even smaller  $h_s/h_{max}$  than 25 (not checked in this series of simulations), which could possibly explain why the conventional “rule of thumb” (which does not consider the aspect ratio) only requires  $h_s/h_{max} > 10$ . It is, however, clear from the Fig. 2.7 that *both*  $r_s/h_s > 1$  and  $h_s/h_{max} > 100$  in order for convergence to be met.

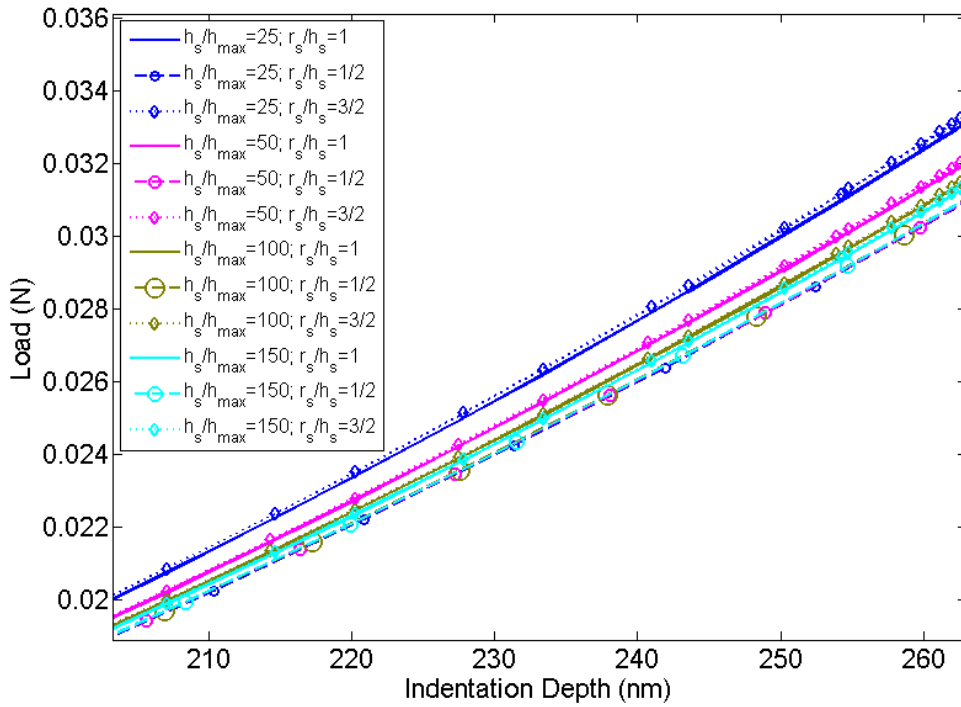


Fig. 2.7. Convergence study for different  $h_{max}/h_s$  and  $r_s/h_s$

### 2.3.3. Finite Tip Radius Effect

When considering the geometry of the indenting cone, Sneddon assumed an infinitely sharp tip. In reality, the tip of the indenter has a finite tip radius of curvature. The finite tip radius effect was observed and explicitly discussed by many researchers

over the years (Doerner and Nix, 1986; Shih et al., 1991; Wang et al., 2006; Yu et al., 2004). These authors generally perceived the finite tip radius effect as a deviation from the estimated projected tip area,  $A$ . Doerner and Nix (1986) calibrated the tip area function,  $A(h_c)$ , of the indenter using careful measurements from transmission electron microscopy (TEM) images (proposed by Pethica et al. (1983)). Shih (1991) and Yu (2004) corrected  $A(h_c)$  by introducing a spherical cap on pyramidal equivalent conical indenters. Shih et al. varied the tip radius to fit the  $A(h_c)$  measurements performed by Doerner and Pethica, while Yu et al. modified  $A(h_c)$  such that it takes the function of a spherical indenter at shallow depth and that of a conical indenter when the indentation is deeper than the transition point,  $h_a$ , given by,

$$h_a = \rho (1 - \sin \alpha) \quad (9)$$

where  $\rho$  is the tip radius of the indenter and  $\alpha$  is the half angle of the cone. More recently, Wang et al. (2006) noted that using indenters with different tip radii resulted in significantly different load-displacement curves. The authors observed that the values of the measured load increase for a tip with a larger radius of curvature at the same indentation depth. They plotted the load-displacement curves for identical specimens using different tip radii and also tabulated some examples of the indenter's tip radius effect on the calculated Young's modulus, and discussed qualitatively some possible sources of error. This study will investigate the effect of finite tip radius on the load-displacement curves of an elastic specimen quantitatively.

The finite tip effect on load-displacement curves was observed in our simulations (Fig. 2.8), and it is consistent with the expectation that a blunt tip will require a greater load to penetrate the specimen to the same depth as compared to a sharp tip. It was noted

that the correction for the finite tip radius effect is crucial for the accurate measurements of material properties especially in shallow indentations (Yu et al., 2004). To identify the effects of a finite tip radius, numerical simulations were performed. The conical tip used in the simulations was modeled to be analytically rigid, and had a tip radius of curvature that ranged from 30 nm to 1  $\mu\text{m}$ . The cylindrical specimens used in the simulations had converged geometries as defined earlier in (8). Their Young's moduli and Poisson's ratios ranged from 10 GPa to 200 GPa, and from 0.01 to 0.49, respectively, in the simulations.

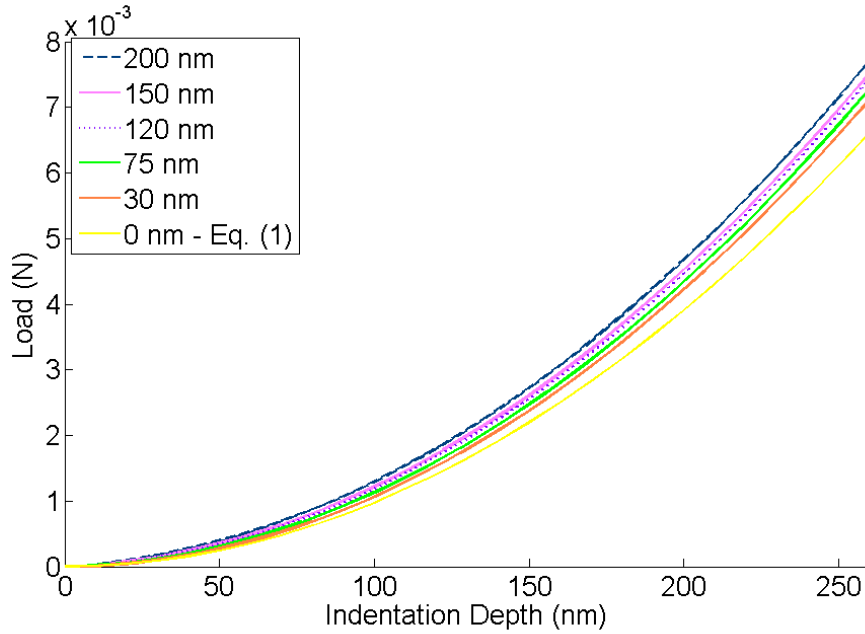


Fig. 2.8. Simulated load-displacement curves of identical elastic cylindrical specimens ( $E = 50 \text{ GPa}$ ,  $\nu = 0.3$ ) indented with rigid conical indenters of different tip radii,  $\rho$  (0, 30, 75, 120, 150, and 200 nm)

Unlike the load displacement relationship derived by Sneddon in (1), where there is only an  $h^2$  term, the load-displacement relationships obtained from these numerical 'experiments' were found to have the following form,

$$P = Kh(h + L) \quad (10)$$

where  $K$  and  $L$  are constant coefficients independent of  $P$  and  $h$ . The results from the simulations suggest that  $K$  is a function of the geometry of the indenter and the elastic constants of specimen similar to that in Sneddon's equation (Eq. (1)), while  $L$  is a function of the radius of curvature of the tip,  $\rho$ . A modified elastic indentation equation was derived empirically for the range of elastic properties and tip radii as mentioned previously,

$$\begin{aligned}
 P &= f(\nu) \frac{2 E \tan(70.3^\circ)}{\pi (1 - \nu^2)} h (h + g(\rho)) \\
 &= (a_1 \nu^2 + a_2 \nu + a_3) \frac{2 E \tan(70.3^\circ)}{\pi (1 - \nu^2)} h (h + c_1 \rho^2 + c_2 \rho)
 \end{aligned} \tag{11}$$

where,  $a_1 = -0.062$ ,  $a_2 = -0.156$ ,  $a_3 = 1.12$  and  $c_1 = 1.50e4 \text{ m}^{-1}$  and  $c_2 = 1.17e-1$ .

This equation fits the results from numerical simulation very well ( $R^2 > 0.99$ ). For simple abbreviation,  $f(\nu)$  and  $g(\rho)$  are referred to as the multiplicative and additive factor, respectively. Figures 2.9 and 2.10 show the curve fit for the multiplicative and additive factor, respectively. It is interesting to note that these are two sources of divergence from Sneddon's solution. Sneddon's solution will be recovered when the multiplicative term equals one (unfortunately, when  $\nu = 0.63$ , which is physically unrealistic) and when the tip radius of curvature,  $\rho$  equals zero.

The multiplicative term,  $f(\nu)$ , similar to that found in the load-displacement relationship found empirically by Larsson et al. (1996) for Berkovich indenters, is likely due to the correction for radial displacements in Sneddon's solution when  $\nu < 0.5$ , as discussed by Hay et al. (1999).

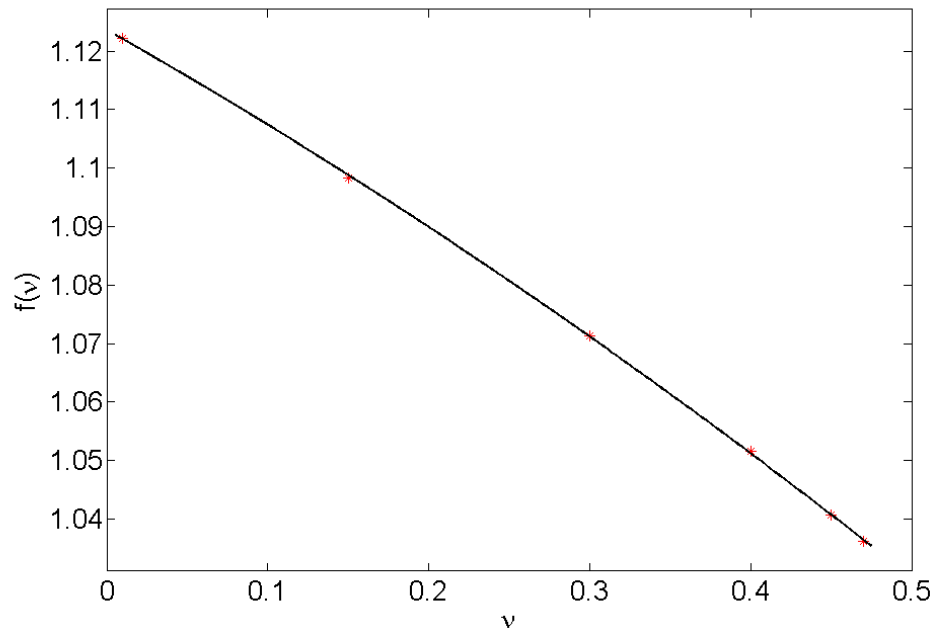


Fig. 2.9. Multiplicative factor,  $f(\nu)$ , as a function of Poisson's ratio,  $\nu$  ( $R^2 = 0.9999$ )

Figure 2.11 compares various correction factors, the correction factors,  $\zeta(\nu)$ , proposed by Hay et al. (1999), with  $f(\nu)$  from (11) for a conical indenter with  $\alpha$  of  $70.3^\circ$ . It can be observed that  $f(\nu)$  in (11) is practically identical to the correction factor,  $\zeta(\nu)$  proposed in Eq. (20) from the work of Hay et al. (1999) for  $\nu$  smaller than 0.2. As  $\nu$  approaches 0.5, this difference becomes larger. As compared to the functions proposed by Hay et al.,  $f(\nu)$  is observed to adequately describe the FEM results performed by Hay et al. at  $\nu$  equals 0, 0.2, and 0.4, respectively. Unfortunately, no FEM results were provided for the correction factor as  $\nu$  approaches 0.5, for comparison with  $f(\nu)$ .

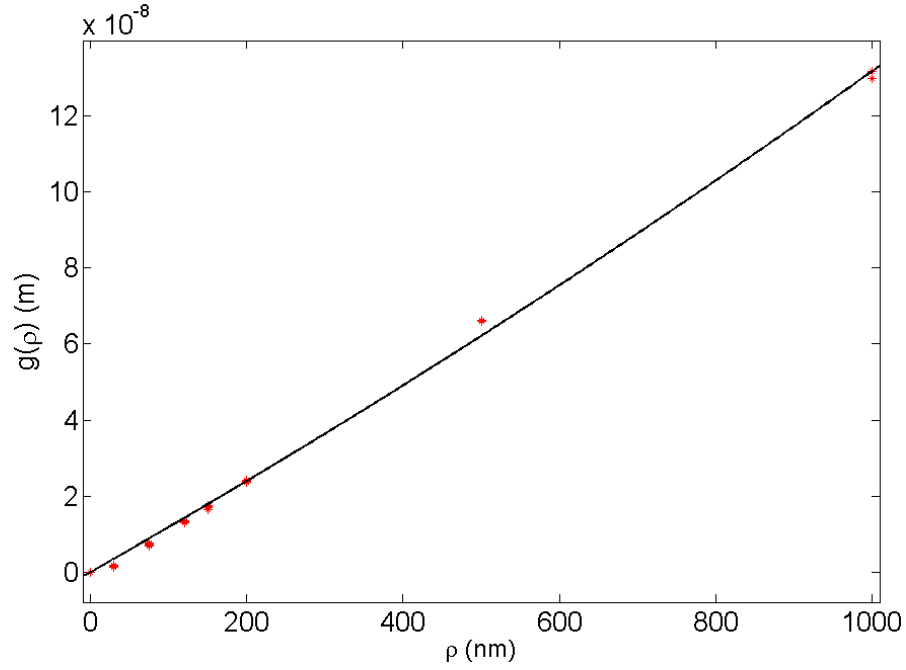


Fig. 2.10. Additive factor,  $g(\rho)$ , vs. tip radius,  $\rho$  ( $R^2 = 0.9977$ )

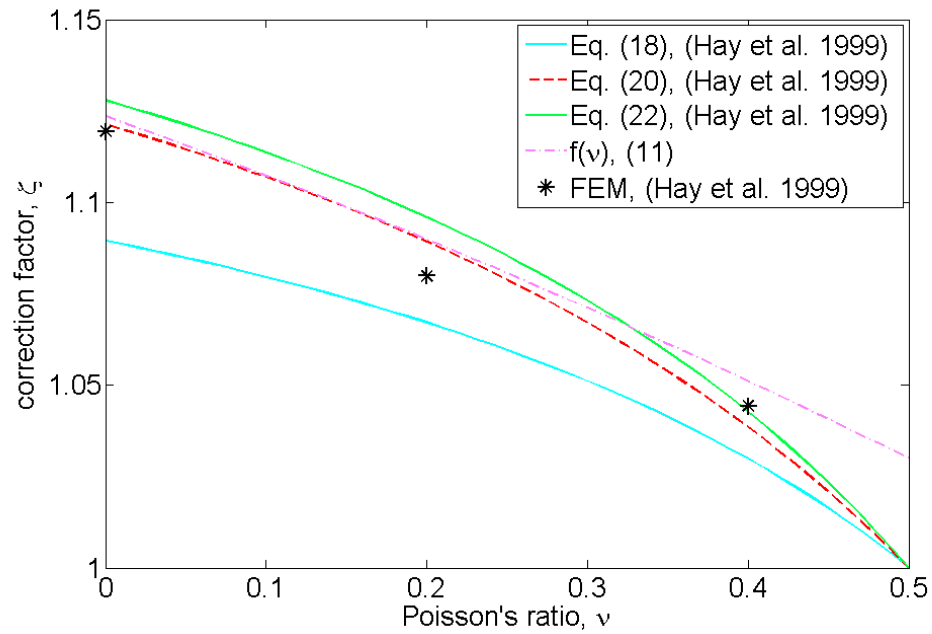


Fig. 2.11. Comparison of Hay's correction factor,  $\zeta$ , and  $f(\nu)$  (after Hay et al., 1999)

Figure 2.12 shows the accurate description of (11), for elastic indentation of compressible specimens with indenters with finite tip radii over a range of elastic constants. The empirically derived load displacement relationship (11) matches the simulation results very well — the dotted lines represent Sneddon's analytical solution (1). With an accurate elastic load-displacement expression that includes the effect of finite tip radius of the indenter, the elastic constants of an elastic specimen of interest can be derived in a straightforward manner. In the spirit of (6), the unknown elastic constants can be expressed as,

$$\frac{E}{1-\nu^2} (a_1\nu^2 + a_2\nu + a_3) = \frac{\pi \cot(70.3^\circ)}{2(2h + c_1\rho^2 + c_2\rho)} \frac{dP}{dh}. \quad (12)$$

It is important to note that (11) can be used directly to solve for the elastic constants. It is not necessary to use the slope of the load-displacement curve,  $dP/dh$ , instead of the direct use of load-displacement measurement. The latter is in fact favorable due to the elimination of uncertainties associated with the measurement of the slope. However, (12) will be used in subsequent parts of the paper to provide a direct comparison of the proposed load-displacement relationship with the existing one, (6).

The first observation in examining (12) is that, similar to the conventional derivation, the Young's modulus,  $E$ , and Poisson's ratio,  $\nu$ , of the specimen are coupled. The second observation is that the coupled term on the left-hand side of the equation can be solved in a straightforward manner, provided the terms on the right-hand side are known, which includes the tip radius. In the following section, viable procedures to identify  $\rho$  using a calibration specimen, and to decouple the elastic constants  $E$  and  $\nu$  will be proposed.

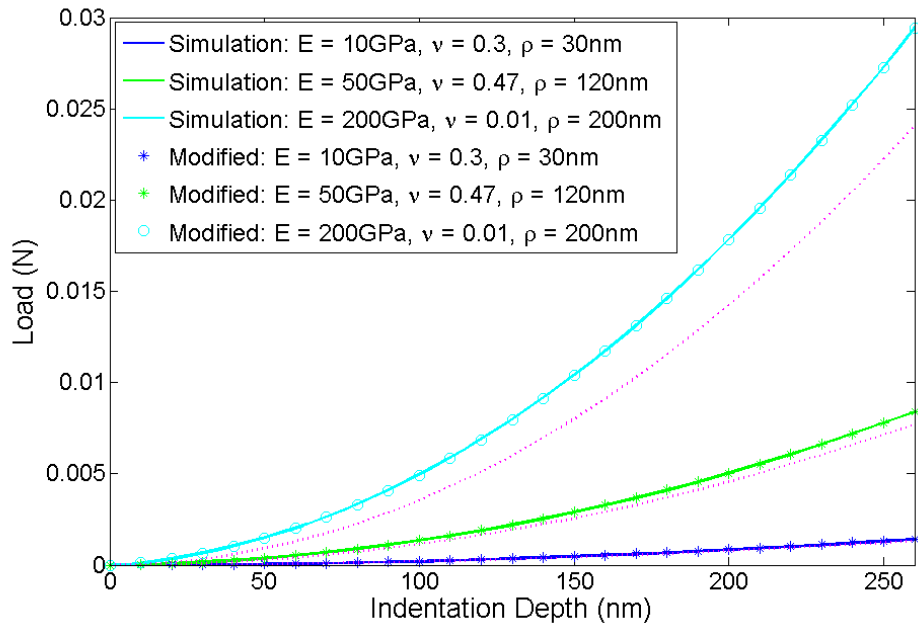


Fig. 2.12. Comparison of simulation results with proposed empirical curve fits for various material constants and tip radii of the rigid indenter

## 2.4. PROPOSED TECHNIQUES AND MODIFICATIONS

### 2.4.1. Technique for Characterizing the Tip Radius of the Indenter

The typical radius for brand new nanoindenter tips are usually in the range of 50-200 *nm*, and it is often difficult to measure accurately — the manufacturer can generally provide the radius of curvature of the indenters up to an uncertainty of 100 *nm*. There have been some suggested methods of retrieving the tip radius of the indenter. Shih et al. (1991) were able to retrieve the tip radius of the indenter by comparing the  $A(h_c)$  of his proposed spherical cap model with that measured experimentally using TEM images, as described by Doerner et al. (1986). Using the measured tip radius, Shih showed that there was good agreement between the results from numerical simulations and experiments. This method, however, is cumbersome to perform, and it is likely to fail for shallow indentations, as it does not consider elastic recovery of the plastic imprint. Yu et al. (2004) proposed a method to retrieve the tip radius that is suitable for shallow indentations, by measuring  $h_a$ , using a "bilocular spherical-conical" fitting method. This method however, is difficult to implement when  $\alpha$  is large, as is the case for Berkovich/Vickers equivalent conical indenters. The large value of  $\alpha$  will result in a small  $h_a$  (shown by (9)), thus making it difficult to accurately distinguish the spherical section from the conical one, using a least-squares fit of this model. The procedure proposed here is suitable for large angle conical indenters ( $\alpha = 70.3^\circ$ ) and does not require cumbersome measurements of the tip area function,  $A(h_c)$  to retrieve the value of the tip radius.

The following example demonstrates how the tip radius of the indenter can be inferred in principle, as the practicality of this technique may be limited by the

availability of a linearly elastic material. Suppose there is a 'sufficiently large' (with converged geometry) linearly elastic specimen with  $E = 50 \text{ GPa}$  and  $\nu = 0.47$ , indented by a rigid Berkovich/Vickers equivalent conical indenter with an unknown  $\rho$  to a maximum depth of  $263 \text{ nm}$ . The measured load-displacement curve is shown in Fig 2.12.

The measured load-displacement curve is fitted with a quadratic curve using least-square fit. The equation of the fitted curve is found to be,

$$P = 1.182e11h^2 + 1597h . \quad (13)$$

From (11), it can be shown that

$$c_1\rho^2 + c_2\rho = 1597/1.182e11 . \quad (14)$$

Solving (14), one obtains the following two roots for the equation,

$$\rho_1 = -7.90 \mu\text{m} \quad \text{and} \quad \rho_2 = 0.114 \mu\text{m} .$$

It can be noted immediately that  $\rho_1$  is inadmissible. One can confidently conclude that  $\rho = 114 \text{ nm}$ , in this case. The indenter used in the simulation has a radius of curvature,  $\rho$  of  $120 \text{ nm}$ , which confirms that this procedure yields fairly accurate results within 5% of the true value. It should be noted that this method does not require a specimen with known material properties. However, the curve fitting process can be optimized over one variable (the coefficient of the  $h$  term), instead of two (the coefficient of the  $h^2$  term is a function of  $E$  and  $\nu$ ), if the material properties of the specimen is known.

#### 2.4.2. Methodology to Decouple the Measurements for Linear Elastic Constants, $E$ and $\nu$

An interesting observation is that the coupled elastic constants ( $E$  and  $\nu$ ) can be decoupled if two different indenters are used, of course assuming that the specimen of interest is linearly elastic, which may be hard to come by. The load-displacement

relationship for an elastic indentation using a spherical indenter is given by the Hertz equation (1881),

$$P = \frac{4}{3} \frac{E}{1 - \nu^2} \sqrt{R} h^{3/2} . \quad (15)$$

Since there is no issue with finite tip radius in the case of spherical indenters, the simulated load-displacement curve is expected to coincide with the Hertz equation. This was validated as shown in Fig. 2.13. As discussed previously, (6) is valid for all bodies of revolution, thus can be used in the case of spherical indenters. The tip area function of a spherical indenter (Fischer-Cripps, 2004) is,

$$A_{sphere} \approx 2\pi R h_c \quad (16)$$

where  $R$  is the radius of the spherical indenter and  $h_c$  is the contact depth. For an indentation with a spherical indenter,  $h_c$ , is given by,

$$h_c = h/2 . \quad (17)$$

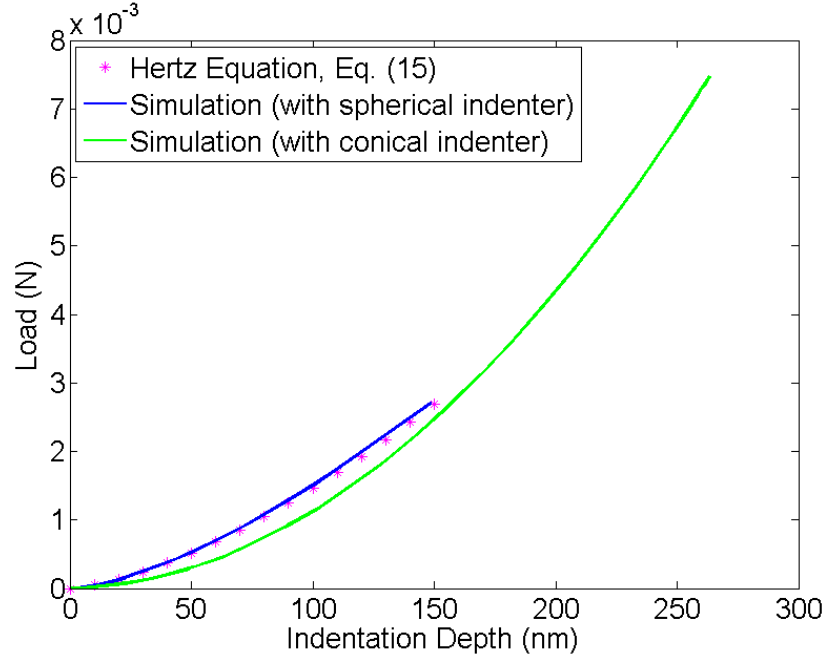


Fig. 2.13. Load-displacement curves for Hertz equation (15) and simulated indentations using spherical and conical indenters on identical specimens

Figure 2.13 illustrates two load-displacement curves corresponding to spherical and conical indenters, respectively. The spherical indenter has a radius,  $R$  of  $400 \text{ nm}$  and the specimen was indented to a maximum indentation depth,  $h_{max}$  of  $150 \text{ nm}$ . At  $h_{max}$ , the slope was found to be  $2.67e4 \text{ N/m}$ , and the projected tip area of contact was found to be  $1.86e-13 \text{ m}^2$ . Using (6),  $E_r$  was found to be,

$$E_r = \frac{E}{1 - \nu^2} = 54.8 \text{ GPa} . \quad (18)$$

The conical indenter has a tip radius,  $\rho$ , of  $75 \text{ nm}$  and the specimen was indented to a maximum depth,  $h_{max}$ , of  $263 \text{ nm}$ . At  $h_{max}$ , the slope was found to be  $5.6e4 \text{ N/m}$ . Using (12),

$$\frac{E}{1 - \nu^2} (a_1 \nu^2 + a_2 \nu + a_3) = 58.9 \text{ GPa} \quad (19)$$

where  $a_i$  are constants as defined in (11). Solving (18) and (19), the Young's modulus,  $E$ , and Poisson's ratio,  $\nu$ , were found to be 50.5 *GPa* and 0.281, respectively. The specimen was modeled with  $E = 50$  *GPa* and  $\nu = 0.3$ . This procedure does not require *a priori* knowledge of one elastic constant to derive the other, and instead it allows both the elastic constants to be calculated independently and simultaneously.

#### 2.4.3. Quantifying Error Due to Finite Tip Radius and Specimen's Compressibility

Figure 2.12 shows that (11) accurately describes the load-displacement measurements of elastic indentations using an indenter with finite tip radius, and there are visible differences with the equation derived by Sneddon (Eq. (1)). It is of interest to quantify the error that is propagated in the derivation of elastic constants due to finite tip radius.

Since it was shown that the load-displacement relationship (using an indenter with a finite tip radius) can be accurately described by (11), one can use this equation to calculate the reduced modulus,  $E_r$ , in the conventional way (6) as described in the previous section. The value of  $E$  can be extracted from  $E_r$  by substituting a known value of  $\nu$ . The slope of the load-displacement curve can be obtained by differentiating (11), to calculate the contact depth,  $h_c$ , and projected area of contact,  $A$ .

Differentiating (11),

$$\frac{dP}{dh} = \frac{2 E \tan(70.3^\circ) f(\nu) (2h + g(\rho))}{\pi (1 - \nu^2)} . \quad (20)$$

Recall (4) and solving for  $h_c$  as defined in (5), at  $h_{max}$ ,

$$A = 24.5 h_c^2 = 24.5 \frac{h_{max}^2 ((\pi - 4) g(\rho) - 4h_{max})^2}{\pi^2 (2 h_{max} + g(\rho))^2} . \quad (21)$$

Thus, one arrives at

$$\frac{E_c}{E} = \frac{0.35809}{h_{max}} f(\nu) (2h_{max} + g(\rho)) \tan(70.3^\circ) \sqrt{\frac{(2 h_{max} + g(\rho))^2}{((\pi - 4)g(\rho) - 4 h_{max})^2}} \quad (22)$$

where  $E_c$  is the derived Young's modulus using the conventional method described in Section 2.2. The ratio would be one if the Young's modulus derived using the conventional method is equal to the actual Young's modulus,  $E$ . Note that, the right-hand side of (22) is essentially equal to the correction factor,  $\beta$ , as discussed by researchers to derive an accurate value for the Young's modulus with nanoindentation. The correction factor in this case, appears to be the product of the first correction factor term,  $f(\nu)$  due to radial displacement (Hay et al., 1999) and a term essentially related to the finite tip effects (the rest of the equation). This confirms the proposition by Troyon and Huang (2004). Without an explicit demonstration, the authors proposed that the overall correction factor is the product of  $\zeta$  (to account for the radial inward displacements) and a form factor related to the geometry of the indenter. However, unlike the correction factor proposed by Troyon and Huang, the right-hand side of (22) is a function of indentation depth. Taking the limit as  $h_{max}$  tends to infinity,

$$\lim_{h_{max} \rightarrow \infty} \frac{E_c}{E} = f(\nu) . \quad (23)$$

Thus, for deep linearly elastic indentations, the only relevant correction factor is  $f(\nu)$ , which accounts for the radial inward displacements; the finite tip radius effects are absent, which is within expectation.

The percentage error,  $\varepsilon$  is defined as

$$\varepsilon = \left( \frac{E_c}{E} - 1 \right) \cdot 100 . \quad (24)$$

The percentage error is plotted as shown in Fig. 2.14 for a specimen with Poisson's ratio,  $\nu$ , of 0.3, which is indented to maximum depths,  $h_{max}$ , of 100 nm and 300 nm, respectively. The percentage error,  $\varepsilon$ , is positive for the entire range of  $\rho$ , which suggests that the conventional method will result in an overestimation of the actual  $E$ . This phenomenon was observed for the range of  $E$ ,  $\nu$ ,  $\rho$ , and  $h_{max}$  used in the simulations.

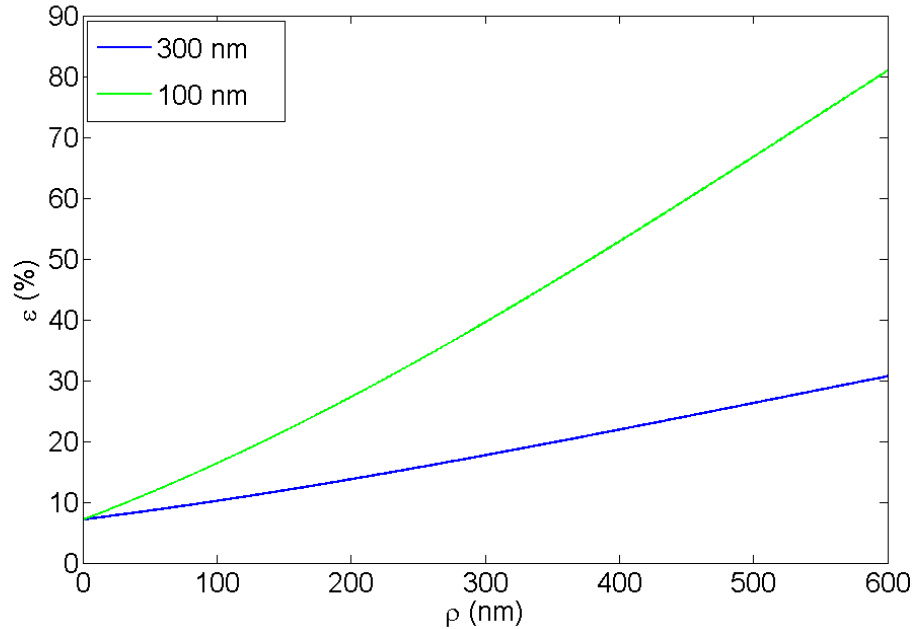


Fig. 2.14. Percentage error in estimation of Young's modulus,  $\varepsilon$ , vs. tip radius,  $\rho$ , for  $h_{max} = 100$  and 300 nm

When  $\rho$  is equal to zero, the error arises from the multiplicative term,  $f(\nu)$ , which is a function of the Poisson's ratio,  $\nu$ . Thus, for specimens with different  $\nu$ , the intercept

would be different. As the tip radius becomes larger, the percentage error increases significantly, which is consistent with expectation. The slope of the  $\varepsilon$  vs.  $\rho$  curve is found to be highly dependent on  $h_{max}$ . Consider the use of an indenter with a tip radius of 150 nm — when the material parameters were obtained at  $h_{max}$  of 300 nm, the conventional derivation will overestimate  $E$  by close to 12%; however when obtained at  $h_{max}$  of 100 nm, the overestimation would be more than 20%. This suggests that the overestimation of  $E$  is more pronounced in shallow indentations, which is consistent with (23) demonstrating that finite tip radius effects are irrelevant in deep indentations. It is important to note that these results were obtained in closed form through algebraic operations as described. The derivation does not take into account any surface and tip-geometry-transition effects, often associated with shallow indentations. This phenomenon is consistent with the observations by Yu et al. (2004), that the effect of “tip roundness” is more severe in shallow indentations.

The tip radius effect affects the accurate determination of the hardness of the material using nanoindentation as well. The additional indentation load,  $\Delta P$ , required by the indenter to attain the same depth due to tip bluntness can be expressed as

$$\frac{\Delta P}{P} = \frac{g'(\rho)\Delta\rho}{h_{max} + g(\rho)}. \quad (25)$$

The measured hardness using a blunt tip,  $H_c$  is given by

$$H_c = \frac{P + \Delta P}{A} = \frac{P}{A} \left( 1 + \frac{g'(\rho)\Delta\rho}{h_{max} + g(\rho)} \right). \quad (26)$$

Thus, the measured hardness over the actual hardness,  $H_c/H$  is given by

$$\frac{H_c}{H} = 1 + \frac{g'(\rho)\Delta\rho}{h_{max} + g(\rho)}. \quad (27)$$

If the tip radius of the indenter tip is zero, the right-hand side of (27) reduces to unity, implying that the measured hardness is accurate. Otherwise, it is evident that the ratio deviates from one.

#### 2.4.4. Sensitivity of the Load-Displacement Measurements to Finite Tip Radius Effect

It has been shown that the finite tip radius effects cause the measured load-displacement curve to deviate from that derived by Sneddon shown by (1). It is of interest to investigate the sensitivity of these effects.

From (25), it is observed that at a given indentation depth, the percentage change in measured load is independent of material properties ( $E$  and  $\nu$ ). This ratio is larger at a shallow indentation (where  $h_{max}$  is small) which is consistent with the previous discussions.

For indentations using a typical tip radius of around 200 nm, a minimum indentation depth of 467 nm is required, in order for the finite tip effects to be insignificant ( $\Delta P/P < 0.05$ ). If the typical maximum load of the nanoindenter of around 10 mN is considered, a material stiffer than 22 GPa will exhibit significant difference between an indentation with an infinitely sharp indenter and that with a finite tip radius of 200 nm.

To investigate this effect, nanoindentation experiments on natural latex rubber were performed. The load-displacement measurement for an indentation on natural latex rubber is shown in Fig. 2.15. The experiment was performed using open loop load-control option on the Hysitron™ Triboindenter. The contact ‘set-point’,  $P_o$ , was set to be 2  $\mu$ N. The indentation sites were scanned and found no residual imprints.

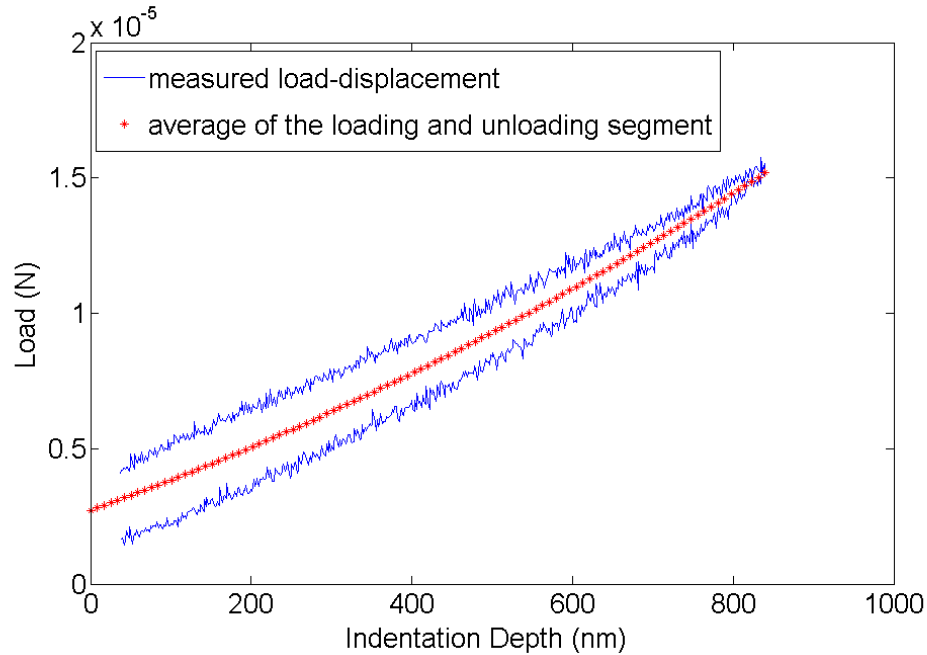


Fig. 2.15. Load-displacement measurement for the indentation of latex rubber

The measured uniaxial stress-strain behavior of latex is shown in Fig. 2.16. It is observed that latex is essentially linearly elastic up to 10% strain. However, hysteresis can be observed in the load-displacement record in Fig. 2.15, which might suggest the attainment of larger strains. To a first approximation, the average behavior of the material is considered as shown in Fig. 2.15.

The averages of the loading and unloading segments of several nanoindentations of natural latex are plotted in Fig. 2.17. The Young's modulus,  $E$ , of the latex was determined to be  $3.46 \text{ MPa}$  from uniaxial experiments, and its Poisson's ratio,  $\nu$  was assumed to be 0.5. Using the values of  $P_o$ ,  $E$ , and  $\nu$ , load-displacement curves for the indentation were plotted for an infinitely sharp tip which corresponds to  $\rho$  of  $0 \text{ nm}$ , and for  $\rho$  of  $200 \text{ nm}$  and  $400 \text{ nm}$ , respectively. It is immediately observed that the effect of  $200 \text{ nm}$  in the tip radius of the indenter does not have such a significant effect on the load-displacement as that illustrated in Fig. 2.8. This confirms that tip radius effects are

generally insignificant for the indentation of relatively soft materials when deep indentation depths can be attained.

Using the average load-displacement curves from all the indentations performed, and assuming that the indenter tip is infinitely sharp, the Young's modulus for the latex indented was found to be 3.26 MPa, which is only about 6% error from the uniaxially measured Young's modulus. However, the effect of preload is very significant in the indentation of soft materials as evidenced in Fig. 2.17. It is crucial that this effect is accounted for in order to accurately extract any elastic properties. This point will be further elaborated in Chapter 4.

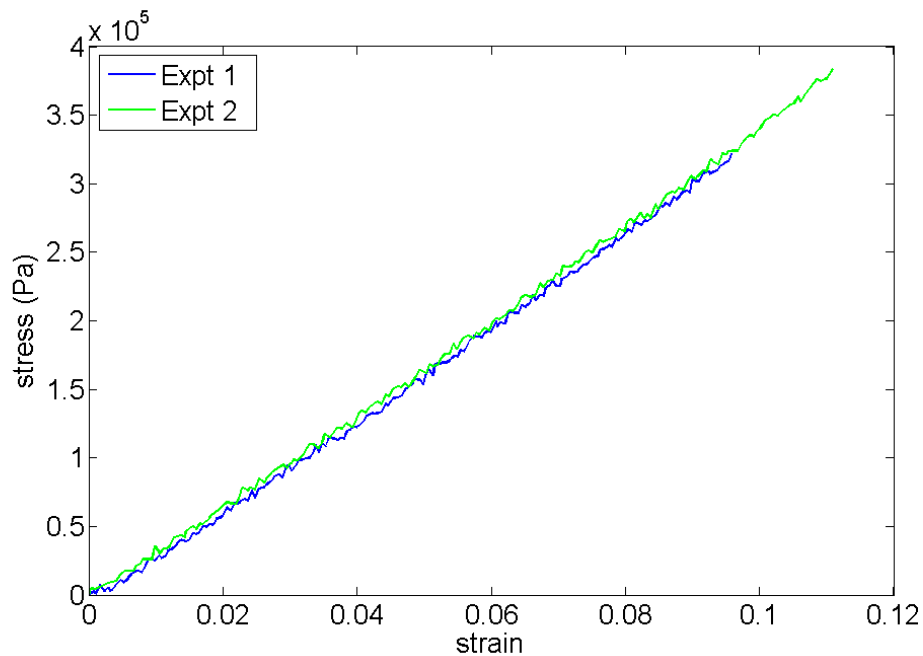


Fig. 2.16. Stress-strain relationship for natural latex from quasi-static uniaxial compression experiments

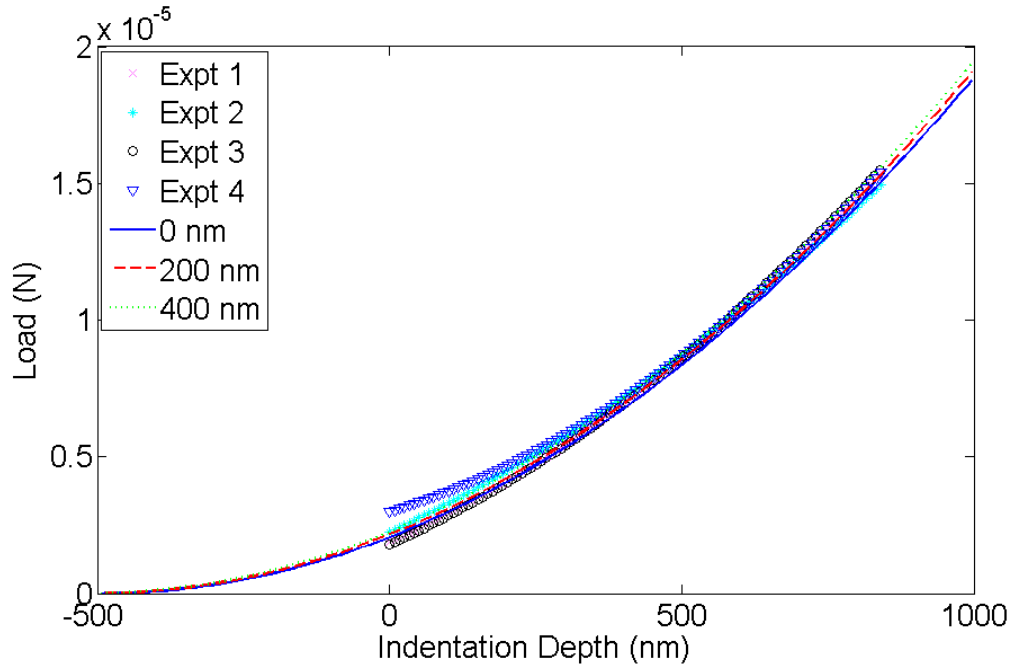


Fig. 2.17. Comparison of experimental results and predicted load-displacement relations for different  $\rho$  (0 nm, 250 nm, 500 nm)

As a final remark, the atomic force microscope (AFM) is commonly used in the indentation of soft materials in the sub- $\mu N$  force range. The tip radius for the AFM typically ranges from 10 nm to 60 nm. Despite the sharp tips used in these indentations, finite tip radius effects can become significant due to the low-load applied in the indentation, resulting in typically shallow indentations. Consider  $\Delta\rho$  of 20 nm and solving around  $\rho$  of 20 nm in (25), the minimum indentation depth,  $h_{crit}$ , for  $\Delta P/P$  to be less than 0.05 is 44.6 nm. Suppose the maximum indentation load is 1  $\mu N$ ; a material stiffer than 196 MPa will result in  $\Delta P/P$  larger than 0.05.

## 2.5. SUMMARY AND CONCLUSIONS

The applicability of Sneddon's solution to the nanoindentation problem has been critically reassessed together with the implications of deviations from the basic assumptions in the analytical derivation, namely having:

1. a specimen with finite dimensions and
2. an indenter tip with a finite tip radius.

This study has clearly defined a criterion for “converged 2-dimensional (axisymmetric) geometry” (8). Geometrical modeling issues are seldom detailed in the literature and this criterion will provide a common basis for comparison. In addition, this study addressed the finite tip effect and developed an accurate empirical load-displacement relationship that takes into account the finite tip radius,  $\rho$  (11). An estimate of the error arising from the neglect of the finite tip effect was provided by performing the conventional derivation procedure based on the load-displacement relation that takes the tip radius into account (11). It was found that the error consistently results in an overestimation of  $E$  (with known  $\nu$ ), which is more pronounced in shallow indentations. The error due to finite tip radius was also found to be more severe in shallow indentations. Finally, nanoindentation on natural latex was performed to experimentally examine the proposed model and techniques introduced in the paper.

Several aspects of nanoindentation have been explored in this work, namely:

1. A procedure to identify the indenter tip radius,  $\rho$ . The tip radius of the indenter is normally not provided by the manufacturers to a great accuracy,

but it has been identified to be crucial for the accurate determination of elastic properties;

2. A procedure using two different indenters has been outlined to decouple the elastic constants,  $E$  and  $\nu$  measured during indentation.

It should however be noted that the proposed procedures are limited to the availability of a linearly elastic material.

This study has shed light on several concepts related to the field of nanoindentation, but many open questions still remain. The ideas proposed in this paper are typically confined to indentations of linearly elastic solids. However, nanoindentation uses sharp indenters that are likely to induce plasticity on the very onset of loading. The validity of these observations in elastic-plastic indentations is addressed in Chapter 3. Elasticity is more commonly observed for softer materials, however additional challenges to accurately extract their material properties remain. These challenges will be carefully examined in Chapter 4.

In conclusion,

- Sneddon's solution was modified to accommodate finite indenter tip radius.
- Valid 2-dimensional specimen geometry for extracting the reduced modulus making use of the converged solutions must satisfy (8).
- The error associated with neglecting the finite indenter tip radius was quantified and an algebraic expression has been developed to account for this effect.
- For a known Poisson's ratio,  $\nu$ , the error consistently results in an overestimation of the Young's modulus,  $E$ .

- The overestimation of  $E$  is more pronounced in shallow indentations.
- An experimental procedure to characterize the indenter's tip radius,  $\rho$ , has been proposed.
- An experimental procedure to decouple the measurement of the linearly elastic constants  $E$  (Young's modulus) and  $\nu$  (Poisson's ratio) has been outlined.

## REFERENCES

- ABAQUS. Hibbit, Karlsson & Sorensen, Inc., Pawtucket, RI.
- Bhushan, B., Koinkar, V.N., 1994. Nanoindentation hardness measurements using atomic force microscopy. *Appl. Phys. Lett* 64, 1653–1655.
- Boussinesq, J., 1885. *Applications des Potentials a l'Etude de l'Equilibre et du Mouvement des Solides Elastiques*. Gauthier-Villars.
- Bulychev, S.I., Alekhin, V.P., Shorshorov, M.K., Ternovskii, A.P., Shnyrev, G.D., 1975. Determining Young's Modulus from the Indentor Penetration Diagram. *Zavodskaya Laboratoriya* 41 (9), 1137–1140.
- Chen, X., Ogasawara, N., Zhao, M., Chiba, N., 2007. On the uniqueness of measuring elastoplastic properties from indentation: The indistinguishable mystical materials. *J. Mech. Phys. Solids* 55, 1618–1660.
- Cheng, Y.T., Cheng, C.M., 1999. Scaling Relationships in Conical Indentation of Elastic Perfectly Plastic Solids. *Int. J. Solids Structures* 36, 1231–1243.
- Dao, M., Chollacoop, N., Vliet, K.J.V., Venkatesh, T.A., Suresh, S., 2001. Computational Modeling of the Forward and Reverse Problems in Instrumented Sharp Indentation. *Acta Materialia* 49, 3899–3918.
- Dimitriadis, E.K., Horkay, F., Maresca, J., Kachar, B., Chadwick, R.S., 2002. Determination of Elastic Moduli of Thin Layers of Soft Material Using the Atomic Force Microscope. *Biophysical Journal* 82, 2798–2810.

Doerner, M.F., Nix, W.D., 1986. A Method for Interpreting the Data from Depth-Sensing Indentation Instruments. *J. Mater. Res.* 1, 601–609.

Fischer-Cripps, A.C., 2004. *Nanoindentation*. Springer.

Giannakopoulos, A.E., Larsson, P.L., Vestergaard, R., 1994. Analysis of Vickers Indentation. *Int. J. Solids Structures* 31, 2679–2708.

Hay, J.C., Bolshakov, A., Pharr, G.M., 1999. A Critical Examination of the Fundamental Relations Used in the Analysis of Nanoindentation Data. *J. Mater. Res.* 14, 2296–2305.

Hertz, H., 1881. *Über Die Berührung Fester Elastischer Körper (On the Contact of Elastic Solids)*. *J. Reine Angew. Math.*, 156–171.

Hill, R., Storåkers, B., Zdunek, A.B., 1989. A Theoretical Study of the Brinell Hardness Test. *Proc. R. Soc. Lond. A*423, 301–330.

King, R.B., 1987. Elastic Analysis Of Some Punch Problems For A Layered Medium. *Int. J. Solids Structures* 23, 1657–1664.

Kral, E.R., Komvopoulos, K., Bogy, D.B., 1993. Elastic-Plastic Finite Element Analysis of Repeated Indentation of a Half-Space by a Rigid Sphere. *J. Appl. Mech.* 75, 829–841.

Larsson, P.L., Giannakopoulos, A.E., 1996. Analysis of Berkovich Indentation. *Int. J. Solids Structures* 33 (2), 221–248.

Laursen, T.A., Simo, J.C., 1992. A Study of the Mechanics of Microindentation Using Finite Elements. *J. Mater. Res.* 7, 616–618.

- Lichinchi, M., Lenardi, C., Haupta, J., Vitalib, R., 1998. Simulation of Berkovich Nanoindentation Experiments on Thin Films Using Finite Element Method. *Thin Solid Films* 312, 240–248.
- Loubet, J.L., Georges, J.M., Marchesini, O., Meille, G., 1984. Vickers Indentation Curves of Magnesium Oxide {MgO}. *J. Tribol-T ASME* 106, 43–48.
- Newey, D., Wilkins, M.A., Pollock, H.M., 1982. An Ultra-Low-Load Penetration Hardness Tester. *J. Phys. E: Sci. Instrum.* 15, 119–122.
- Oliver, W.C., Pharr, G.M., 1992. An Improved Technique for Determining Hardness and Elastic Modulus Using Load and Displacement Sensing Indentation Experiments. *J. Mater. Res.* 7, 1564–1583.
- Pethica, J.B., Hutchings, R., Oliver, W.C., 1983. Hardness Measurement at Penetration Depths as Small as 20 Nm. *Philos. Mag. A* 48, 593–606.
- Pharr, G.M., Bolshakov, A., 2002. Understanding Nanoindentation Unloading Curves. *J. Mater. Res.* 17, 2660–2671.
- Pharr, G.M., Oliver, W.C., Brotzen, F.R., 1992. On the Generality of the Relationship Among Contact Stiffness, Contact Area, and the Elastic Modulus During Indentation. *J. Mater. Res.* 7 (3), 613–617.
- Shih, C.W., Yang, M., Li, J.C.M., 1991. Effect of Tip Radius on Nanoindentation. *J. Mater. Res.* 6, 2623–2628.

Sneddon, I.N., 1948. Boussinesq's Problem for a Rigid Cone. Proc. Cambridge Philos. Soc., 492–507.

Sneddon, I.N., 1965. The Relation Between Load and Penetration in the Axisymmetric Boussinesq Problem for a Punch of Arbitrary Profile. Int. J. Engng. Sci. 3, 47–57.

Storåkers, B., Larsson, P.L., 1994. On Brinell and Boussinesq Indentation of Creeping Solids. J. Mech. Phys. Solids 42, 307–332.

Ternovskii, A.P., Alekhin, V.P., Shorshorov, M.K., Khrushchov, M.M., Skvortsov, V.N., 1974. Micromechanical Testing of Materials by Depression. Zavodskaya Laboratoriya 39 (10), 1242–1247.

Tranchida, D., Piccarolo, S., Loos, J., Alexeev, A., 2006. Accurately evaluating Young's modulus of polymers through nanoindentations: A phenomenological correction factor to Oliver and Pharr procedure. Appl. Phys. Lett 89, 171901–171905.

Troyon, M., Huang, L., 2004. Correction factor for contact area in nanoindentation measurements. J. Mater. Res. 30 (3), 610–617.

VanLandingham, M.R., Villarrubia, Guthrie, W.F., Meyers, G.F., 2001. Nanoindentation of polymers: An overview. In: Tsukruk, V.V., Spencer, N.D. (Eds.), Recent Advances in Scanning Probe Microscopy. Wiley-VCH Verlag GmbH, pp. 15–43.

Wang, T.H., Fang, T.H., Lin, Y.C., 2006. A Numerical Study of Factors Affecting the Characterization of Nanoindentation on Silicon. Mat. Sci. and Engng. 447 (1–2), 244–253.

Woirgard, J., 2006. Some results on the indentation of an elastic half space. *Philos. Mag.* 86 (33–35), 5199–5217.

Yu, N., Polycarpou, A.A., Conry, T.F., 2004. Tip-Radius Effect in Finite Element Modeling of Sub-50 Nm Shallow Nanoindentation. *Thin Solid Films* 450, 295–303.

## CHAPTER 3: AN ANALYSIS OF NANOINDENTATION IN ELASTO-PLASTIC SOLIDS

### ABSTRACT

This chapter examines the accuracy of the extracted elastic properties using the nanoindentation technique on elastic-plastic solids. The application of the correction factor evaluated in the linearly elastic case (in Chapter 2) on elastic-plastic materials is critically examined. It is then established that the accurate determination of the projected area of contact is found to be crucial for the accurate determination of elastic material properties. The conventional method for the accurate determination of contact area is generally limited to ratios of Young's modulus over yield stress,  $E/\sigma_y < 30$  for elastic, perfectly plastic materials, which is too stringent for most materials. Thus, a new electrical resistance method is proposed to measure directly the projected contact area. Using numerical simulations, it is found that with the accurate determination of  $A$ , the error associated with the extracted elastic material properties is reduced by more than 50% in some cases. Using the newly proposed procedure, the error is also found to be independent of  $E/\sigma_y$  and the tip radius,  $\rho$ , and it is only a function of Poisson's ratio,  $\nu$ . This suggests that the errors might be due to the residual stresses at the plastic imprint that are found to depend on  $\nu$  as well.

### 3.1. INTRODUCTION

Motivated by the development of modern applications such as microelectronics, MEMs and biomaterials, there is an increased interest in material characterization in the micro/nano scale in recent years. Nanoindentation has been increasingly popular for its relative ease of use with the advent of modern commercial nanoindenters. Modern depth sensing indentation was first developed in the early 1970s (Bulychev et al., 1975; Loubet et al., 1984; Newey et al., 1982; Pethica et al., 1983; Ternovskii et al., 1974). As the technology improved, manufacturers were able produce smaller indenter tips and load cells with better force resolution, which finally led to the production of commercial nanoindenters.

Nanoindentation was originally developed to measure the elastic properties of the material of interest (Bulychev et al., 1975; Pharr et al., 1992). However, researchers have since developed novel applications, such as acoustic emission testing (Shiwa et al., 1996; Tymiak et al., 2003), impact testing (Fischer-Cripps, 2004), fracture toughness testing (Lawn et al., 1980; Palmqvist, 1957), constant strain rate/creep testing (Bower et al., 1993; Mayo and Nix, 1988; Storåkers and Larsson, 1994), high-temperature testing (Atkins and Tabor, 1966; Kutty et al., 1996; Payzant et al., 1993), and most recently *in situ* electrical measurement testing (Mann et al., 2002; Ruffell et al., 2007) for the nanoindenter.

Nonetheless, the basic determination of the material elastic properties is most often a requirement for further determination of additional mechanical properties. While Chapter 2 considered purely elastic materials to establish some basic facts and

correlations, it is evident that the overwhelming majority of materials display plastic flow to some extent during the nanoindentation process. Plasticity in nanoindentation deviates from the linear elastic assumptions on which Sneddon's derivation is based. Since there is no theoretical solution for general hardening, elastic-plastic materials, the main assumption underlying the extraction of materials properties using nanoindentation is that while the loading stage is elastic-plastic, the unloading stage is purely elastic. Hence, nanoindentation of elastic-plastic solids is still quite suitable for elastic analyses. The elastic unloading assumption is based on the validity of the following two components:

- a. the unloading and subsequent reloading load-displacement curves coincide;
- b. the reloading of a residual imprint can be described as the indentation of a flat surface with an equivalent (thus different) indenter.

Moreover, the factors identified as relevant to linear elastic indentations, such as finite tip radius effect and radial displacement recovery as discussed in Chapter 2, that are not considered in Sneddon's formulation (1948), might still be pertinent towards elastic-plastic indentations as well. Thus, it is important to assess their relevance in the context of the indentation of isotropic, elastic-plastic materials, particularly to examine the validity of the application of the correction factor derived for the linear elastic indentations (Hay et al., 1999; Troyon and Huang, 2004) in elastic-plastic indentations.

This study critically reassesses the various assumptions used in extracting the linearly elastic material properties in an elastic-plastic indentation using experiments and numerical finite element calculations. In addition, the paper proposes viable methods to minimize these errors and obtain an optimal estimation of the elastic and plastic properties. The conventional procedure for extracting the reduced modulus in elastic-

plastic indentation is briefly reviewed in Section 3.2. The results obtained through numerical simulations, the validity of the underlying assumptions, and factors affecting the accuracy of the extracted material properties are all presented in Section 3.3. A novel technique to directly measure the projected contact area is described in Section 3.4. Experimental results from nanoindentation on elastic-plastic solids are used to illustrate the application of the suggested techniques for accurate evaluation of material properties. A summary and conclusions of the study are presented in Section 3.5.

### 3.2. CONVENTIONAL EXTRACTION OF ELASTIC PROPERTIES

Figure 3.1(a) is a schematic of an indentation of an infinitely sharp conical indenter on an elastic-plastic specimen. The thick black line illustrates the indenter tip at its maximum depth, while the thick broken grey line illustrates the indenter tip when fully unloaded. Figure 3.1(b) plots the corresponding load-displacement curve for the indentation. The unloading is assumed to be elastic and  $h_e$  is the recoverable elastic displacement. Upon unloading, the reloading path is expected to follow that of the unloading until  $h_{max}$ , the maximum indentation depth of the previous indentation, is reached.

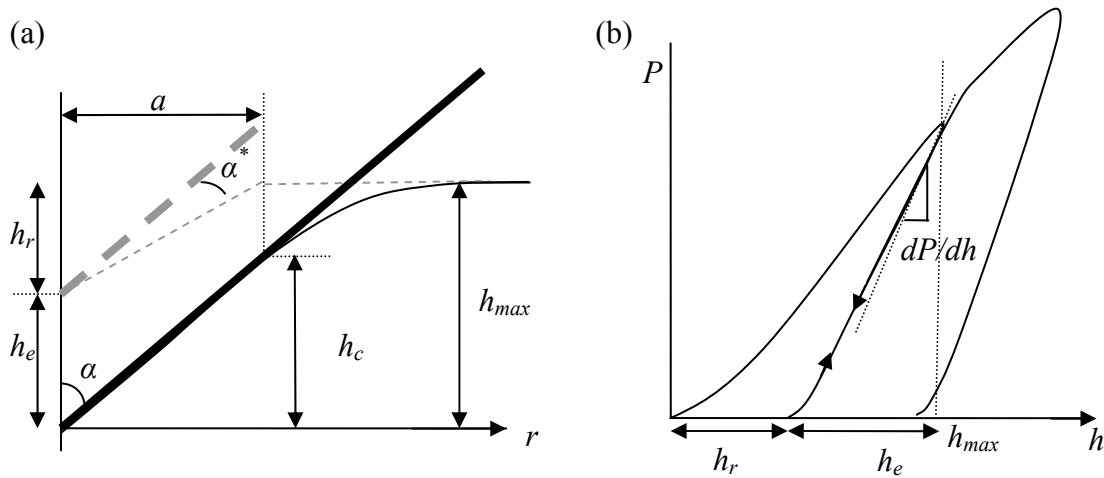


Fig. 3.1. (a) Schematic of an indentation at full load and unload; (b) The corresponding load-displacement curve. (After Fischer-Cripps, 2004)

The elastic unloading path can thus be described by the elastic load-displacement relations derived by Sneddon (1948) assuming an indentation of a rigid conical indenter on a linearly elastic half-plane (see Fischer-Cripps, 2004; Sakai, 2003),

$$P = \frac{2 E \tan \alpha'}{\pi (1 - \nu^2)} h_e^2 \quad (1)$$

where  $P$  is the load measured by the indenter,  $E$  and  $\nu$  are the Young's modulus and Poisson's ratio of the specimen,  $\alpha'$  is the effective half angle of the indenter, and  $h_e$  is the recoverable elastic displacement of the indenter.

Although the reloading path is elastic and follows the previous unloading path until  $h_{max}$ , it is still different from the case of elastic indentation derived by Sneddon (1948). Sneddon assumed that the conical tip is indenting a *flat elastic plane*, whereas during reloading, the conical tip is indenting on a residual imprint. Therefore, the effective half angle,  $\alpha'$  is introduced, which takes into account  $\alpha$ , the half angle of the conical indenter and also the residual imprint left from the previous indentation, as shown in Fig 3.2.

Thus,

$$\alpha' = \frac{\pi}{2} - \alpha^* \quad (2)$$

where  $\alpha^*$  is the angle between the indenter and the residual imprint.

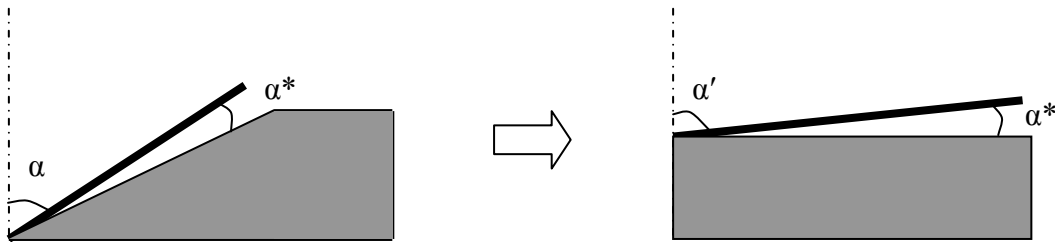


Fig. 3.2. Illustration of the equivalent indentation problem

Using a physical argument that the normal component of the stress at the surface of the specimen remains finite around the contact area with the tip, and an assumption

that both the shear and normal stresses remain zero at the unperturbed surface, Sneddon (Fischer-Cripps, 2004; Sneddon, 1948) found that,

$$h = \left( \frac{\pi}{2} - \frac{r}{a} \right) a \cot \alpha' \quad r \leq a . \quad (3)$$

Thus,

$$h_e = \frac{\pi}{2} a \cot \alpha' . \quad (4)$$

Differentiating (1),

$$\frac{dP}{dh_e} = \frac{4 E \tan \alpha'}{\pi (1 - \nu^2)} h_e . \quad (5)$$

Substituting (4) into (5),

$$\frac{E}{1 - \nu^2} = \frac{1}{2 \beta} \frac{dP}{dh_e} \frac{\sqrt{\pi}}{\sqrt{A}} \quad (6)$$

where  $A$  is the projected contact area and  $\beta$  is the correction factor. The left-hand side of (6) is the reduced modulus,  $E_r$ . In order to reassess the application of Sneddon's equation to nanoindentations, subsequent derivation of  $E_r$  is performed with  $\beta = 1$ .

The conventional relationship used in the extraction of elastic constants in depth-sensing indentation experiments is shown in (6). Bulychev et al. (1975) showed that (6) holds for cylindrical punch and spherical indenters. Subsequently, Pharr et al. (1992) showed that the relationship is true for all indenters that are bodies of revolution. For a Berkovich/Vickers equivalent cone ( $\alpha = 70.3^\circ$ ), the projected contact area,  $A$ , is given by,

$$A = \pi \tan^2 \alpha h_c^2 = 24.5 h_c^2 \quad (7)$$

where  $h_c$  is the contact depth. Note that the projected contact area,  $A$ , is calculated using the half-angle of the indenter,  $\alpha$ . Using (1) and (3),

$$h_c = h_{max} - \chi \frac{P|_{h_{max}}}{dP/dh_e|_{h_{max}}} \quad (8)$$

where  $\chi \approx 0.72$  for conical indenters, and  $\chi = 0.75$  for spherical indenters. Researchers have also proposed that  $\chi$  is a function of the exponent of the unloading curve for the elastic-plastic indentation (Martin and Troyon, 2002; Pharr and Bolshakov, 2002). With the load and displacement of the indenter monitored throughout the indentation,  $h_c$  and  $A$  can be calculated. The value of  $A$  can then be plugged into (6) to derive  $E_r$  for the material of interest. The accuracy of the conventional method is evaluated in the next section by means of numerical simulations.

### 3.3. NUMERICAL SIMULATIONS

Numerical ‘experiments’ were performed using a commercial numerical finite element package, ABAQUS. The indentation experiment was modeled as a 2-dimensional axisymmetric problem using a total of 6252 three-node linear axisymmetric triangular elements (CAX3) for the specimen with converged geometry — i.e.,  $r_s/h_s$  equals unity and  $h_s/h_{max}$  equals 100, where  $r_s$ ,  $h_s$ , and  $h_{max}$  are the radius and thickness of the specimen and maximum indentation depth, respectively. A more refined mesh by doubling the number of elements was used for each specimen size but did not yield significantly different results ( $< 1\%$  difference for the range of indentation depth of interest) for each simulation, which suggests convergence of the existing mesh. The mesh is denser at the indentation site and less dense away from the indentation to minimize computational time. The indenter was modeled as a rigid conical tip with a tip radius,  $\rho$ , of 30 nm and 150 nm. The cylindrical specimen was modeled as an isotropic, deformable elastic, perfectly plastic material, whose  $E/\sigma_y$  ranged from 10 to 1000, and  $\nu$  ranged from 0.01 to 0.47. The results of the numerical simulations are tabulated in Tables 3.1–3.4 in the Appendix.

#### 3.3.1. The Effective Half Angle, $\alpha'$

It is important to examine the relationship between  $\alpha'$  and the mechanical properties of the indented material, as this will provide a relevant range of  $\alpha'$  for typical materials. Figure 3.3 shows the relationship between the effective half-angle,  $\alpha'$ , and  $E/\sigma_y$ . For the linearly elastic case,  $\alpha'$  is equivalent to the half-angle of the indenter,  $\alpha$  (in this

case  $70.3^\circ$ ). As  $E/\sigma_y$  becomes large, i.e., when plasticity becomes dominant,  $\alpha'$  is observed to tend towards  $90^\circ$ . This is consistent with the expectation that when the region of contact is completely plastic, there will be no elastic recovery and thus, the residual imprint will take the shape of the indenter upon unloading, so that  $\alpha^*$  (Fig. 3.2) is  $0^\circ$ , corresponding to  $\alpha'$  of  $90^\circ$ .

The theoretical cohesive strength,  $\sigma_c$  of a solid, is on the order of  $E/10$ . However, it is well documented that this is much larger than the typical strength of solids, which is typically between  $E/100$  and  $E/1000$ . Based on this estimate, the relevant  $\alpha'$  for typical materials ranges between  $88^\circ$  and  $89.7^\circ$ . It should be noted that the elastic, perfectly plastic materials considered here are the limiting case; materials that harden will reduce the extent of plasticity in the specimen under indentation and thus, reduce the effective half-angle,  $\alpha'$  of the equivalent problem.

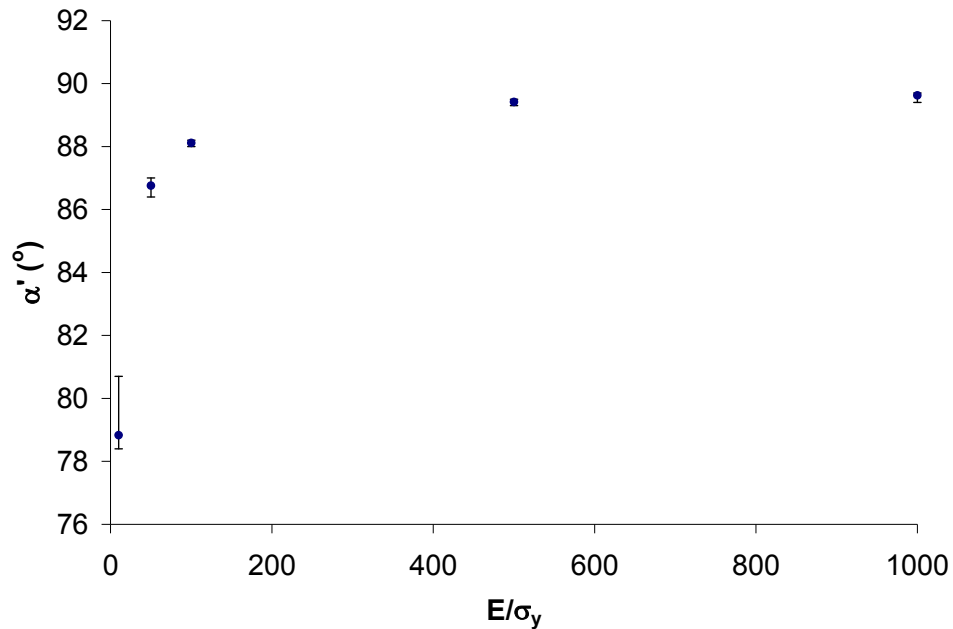


Fig. 3.3. Effective half-angle,  $\alpha'$ , vs.  $E/\sigma_y$ . Error bars represent spread of data for  $\nu$  from 0.01 to 0.47

### 3.3.2. The Relationship Between $h_e/h_{max}$ and $E/\sigma_y$ for Elastic, Perfectly Plastic Materials

The yield stress,  $\sigma_y$  of a rigid perfectly plastic material has been identified to be related to the hardness of the material through (Hill et al., 1947; Tabor, 1948; 1951)

$$H = C\sigma_y \quad (9)$$

For metals in general, it has been shown empirically that the constraint factor  $C \approx 3$ . It would seem that with an accurate measurement of  $H$ ,  $\sigma_y$  can be calculated in a straightforward manner; however  $C$  is dependent on material properties, namely the extent of plasticity measured by  $E/\sigma_y$ , strain hardening,  $n$ , and other strengthening mechanisms such as pressure sensitivity (in polymers and granular materials), etc. (Fischer-Cripps, 2004; Tabor, 1951). As such,  $C$  commonly varies from 1.5–3 and is largely material dependent. The relationship proposed subsequently in this section takes the extent of plasticity,  $E/\sigma_y$ , into account. While the derived value of hardness depends on the actual contact area, which is affected by effects of pile-ups and sink-ins (Miyake et al., 2004), the proposed relation uses the elastic recoverable displacement,  $h_e$  and maximum indentation depth,  $h_{max}$ , to infer the value of the yield stress. These parameters are directly measured during an indentation experiment. For elastic, perfectly plastic solids, the proposed model takes pile-ups around the indentation into consideration by establishing a relationship between  $h_e$  and  $h_{max}$  with respect to  $E/\sigma_y$ . For hardening elastic plastic solids, the amount of pile-ups around the indentation will be lesser than that for elastic, perfectly plastic solids. This is not accounted for by the proposed model, thus it can only provide an upper bound for  $\sigma_y$ .

Using numerical simulations, a relationship is identified between  $E/\sigma_y$  and  $h_e/h_{max}$ , which is given by,

$$\frac{h_e}{h_{max}} = 2.98 \left( \frac{E}{\sigma_y} \right)^{-0.68} . \quad (10)$$

This relationship was obtained through the fitting of mean  $h_e/h_{max}$  at five discrete values of  $E/\sigma_y$ . The fit had a  $R^2$  value of 0.999. The spread illustrated by the error bounds at each  $E/\sigma_y$  represents the range of values for  $\nu$  ranging between 0.01 and 0.47 and for  $\rho$  ranging between 30 nm and 150 nm. The average standard deviation for each spread was approximately 12% of their respective mean.

The yield stress,  $\sigma_y$  can now be calculated for elastic, perfectly plastic materials using (10), since both  $h_e/h_{max}$  (Fig. 3.1) and  $E$  are typically measured or extracted from a typical indentation experiment. For hardening materials, the calculated  $\sigma_y$  using (10) is the upper bound for the actual  $\sigma_y$ . Elastic materials correspond to  $h_e/h_{max}$  of one. Materials that strain or pressure harden will fall within the shaded area between  $h_e/h_{max}$  of one and the line given by (10).

The relation provided by (10) was verified in a series on nanoindentation experiments of single-crystal aluminum oriented in the (100) direction, fused quartz, platinum-based based bulk metallic glass, homalite (a brittle glassy polymer), and single crystal silicon oriented in the (100). Their measured  $h_e/h_{max}$  ratios are plotted against the known ratio  $E/\sigma_y$ , as shown in Fig. 3.4. The experiments were carried out on a Hysitron™ Triboindenter, with a Berkovich diamond tip. The load-displacement displacement curves were obtained following conventional correction techniques for machine compliance and other system calibrations such as thermal drift.

The first observation is that the data points for all materials fall within the shaded region, confirming that (10) is indeed a bound for elastic-plastic materials. The single-crystal aluminum data fall on the elastic, perfectly plastic line, which suggests that this

material does not significantly strain harden under confined flow during indentation. However, it should be noted that while  $h_e$  and  $h_{max}$  were measured directly from the nanoindentation experiments, bulk polycrystalline aluminum values for  $E$  and  $\sigma_y$  were used to determine the location on the x-axis. Due to the lack of grain boundaries,  $\sigma_y$  for single-crystal aluminum is likely to be smaller than that for polycrystalline aluminum, which will shift the experimental points to the right into the shaded region. The single-crystal aluminum was identified as highly anisotropic (Hansen and Huang, 1998), thus the selection of representative  $E$  and  $\sigma_y$  is non-trivial. Nonetheless, the use of bulk polycrystalline aluminum's properties provides some comparison for single crystal aluminum to other materials. Moreover, since the  $\sigma_y$  chosen is likely to overestimate the actual value of  $\sigma_y$  for single-crystal aluminum, these experimental points provide a stringent confirmation that (10) is indeed a bound for elastic-plastic materials. The other materials were found to deviate from the elastic, perfectly plastic line, which can be attributed to the operation of hardening mechanisms, such as work hardening or hardening due to the high hydrostatic pressure created under the indenter tip. The statistical variations for the experiments are summarized in Table 3.5 in the Appendix.

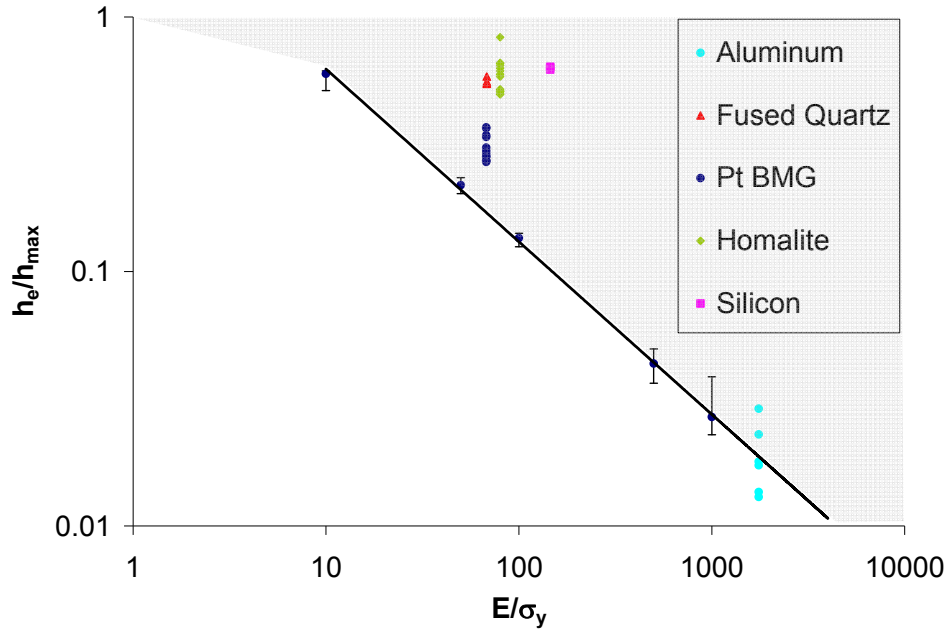


Fig. 3.4.  $E/\sigma_y$  vs.  $h_e/h_{max}$  for different materials

### 3.3.3. Error Involved in the Conventional Derivation

The percentage error,  $\varepsilon$ , in the determination of elastic modulus  $E$  is defined as,

$$\varepsilon = \frac{E_{calculated} - E_{prescribed}}{E_{prescribed}} \cdot 100 \quad (11)$$

The percentage error,  $\varepsilon$ , was found to vary with  $\rho$ ,  $\nu$  and  $E/\sigma_y$ . From Tables 3.1 and 3.3, one can observe that  $\varepsilon$  is directly related to indenter tip radius,  $\rho$  — i.e., the use of a blunt tip results in a larger error using the conventional derivation.

The sensitivity of  $\varepsilon$  to changes in  $\nu$  and  $E/\sigma_y$  can be seen from Fig. 3.5. It is observed that  $\varepsilon$  is larger as  $\nu$  approaches 0. The percentage error on the extracted Young's modulus,  $E$ , was also observed to increase with  $E/\sigma_y$  — i.e., the larger the extent of plasticity, the larger the error observed in the calculated  $E$ . This observation seems to imply the inaccuracy of the underlying elastic unloading assumption, which is central to

the correctness of the conventional method. The elastic unloading assumption is based on the two assumptions listed in the introduction to Section 3.1. These two assumptions are critically examined in the subsequent section.

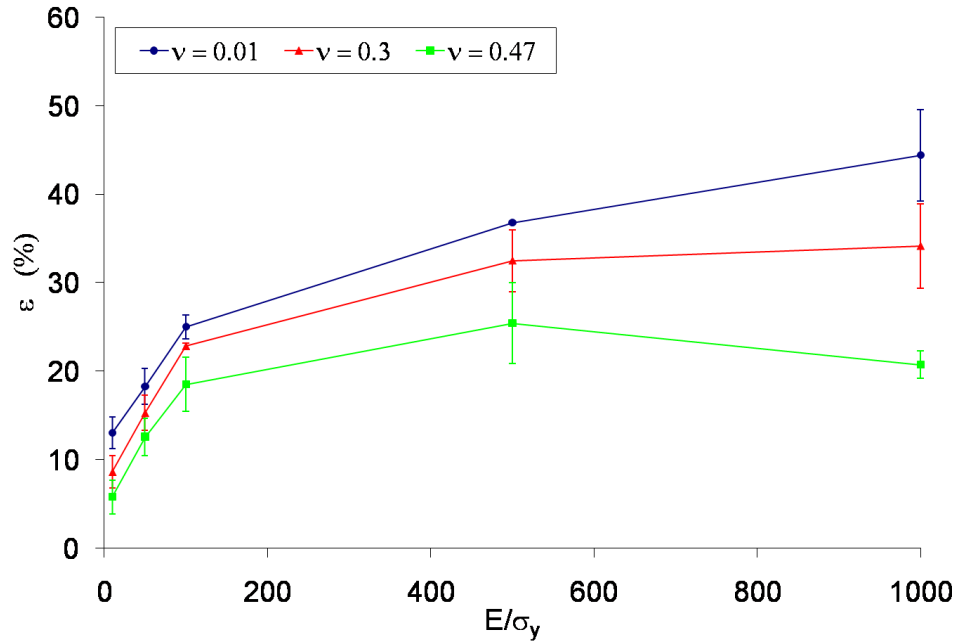


Fig. 3.5. Percentage error of  $E$ ,  $\epsilon$ , vs.  $E/\sigma_y$ , for different  $\nu$  (0.01, 0.3, 0.47). The spread represents different indenter tip radius ranging between 30 nm and 150 nm

### 3.3.4. Examination of the Underlying Assumptions

#### 3.3.4.1. Does the unloading and subsequent reloading load-displacement follow the same path?

The conventional derivation assumes that the unloading is elastic with the expectation that reloading of the indenter will take the prior unloading path until the prior maximum indentation depth,  $h_{max}$  is reached. To verify this assumption, indentation experiments and simulations were performed. Single-crystal aluminum in the (100) orientation and fused quartz were indented with the Hysitron™ Triboindenter. The

experiments were carried out in a load-control mode, using a diamond Berkovich indenter tip. The specimens were indented to a preset load, then unloaded and reloaded to a higher preset load before the final unloading. A similar numerical ‘experiment’ was also performed using ABAQUS. The conical indenter tip was modeled as rigid with  $\alpha = 70.3^\circ$  and  $\rho = 30 \text{ nm}$ . The elastic, perfectly plastic cylindrical specimen was modeled with  $E = 200 \text{ GPa}$ ,  $\sigma_y = 1 \text{ GPa}$ , and  $\nu = 0.3$ .

From Fig. 3.6, it can be observed that the unloading and reloading paths coincide for both the curves obtained through experiments and through numerical simulation. The material properties of the specimens considered were varied and the extent of plasticity in the specimens during indentation was different. Thus, it can be concluded that the unloading curve is indeed elastic and the common assumption for the unloading path to be perceived as an elastic reloading path is valid.

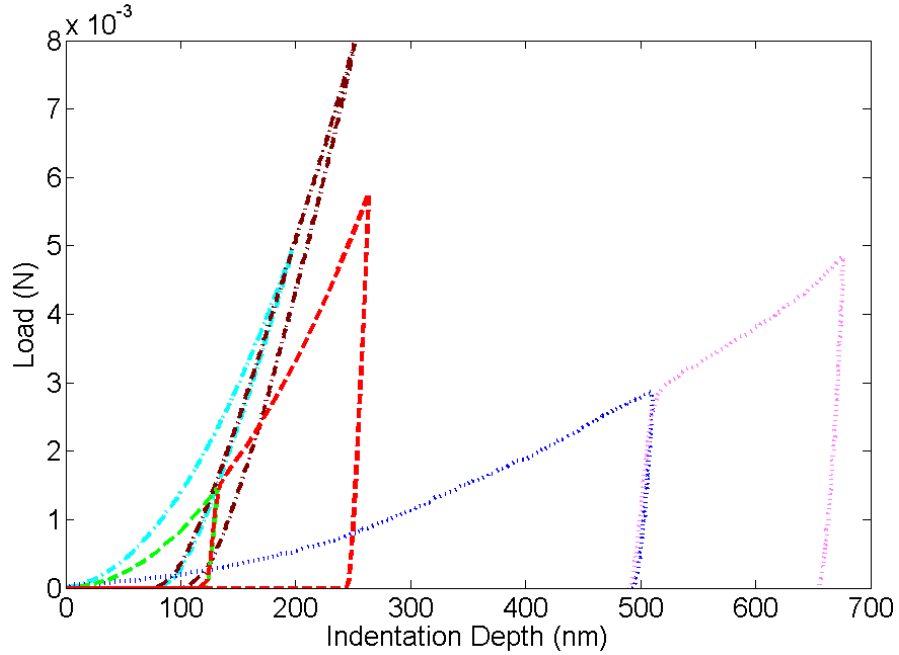


Fig. 3.6. Loading-reloading curves obtained from nanoindentation experiments on fused quartz (dash-dotted line) and single-crystal aluminum (dotted line), and from numerical simulation with  $E = 200 \text{ GPa}$ ,  $\sigma_y = 1 \text{ GPa}$ ,  $\nu = 0.3$ , and  $\rho = 30 \text{ nm}$  (dashed line)

#### 3.3.4.2 Validity of the ‘equivalent’ problem

Having validated the assumption that the elastic unloading curve of the elastic-plastic indentation may be treated as an elastic loading curve of an indentation on a specimen with a plastic imprint, it is imperative to examine the validity of the ‘equivalent’ problem used to solve the latter. Two numerical simulations were performed, with conical tips ( $\alpha = 70.3^\circ$ ) indenting on notched specimens (to emulate plastic imprints), such that  $\alpha'$  equals  $85^\circ$  and  $89^\circ$ , respectively. From Fig. 3.3, the values of  $\alpha'$  chosen correspond to  $E/\sigma_y$  of approximately 25 and 500, respectively, which are representative for a wide range of common materials. Figure 3.7(a) illustrates the indenter and specimen before reloading, while Fig. 3.7(b) shows them at maximum depth,  $h_{max}$ .

Figure 3.8 shows the load-displacement curves for the indentation of notched specimens with  $\alpha'$  equals  $85^\circ$  and  $89^\circ$  (obtained from the numerical simulations), and their comparison with Sneddon's solution (1), plotted with the corresponding  $\alpha'$ . The simulation results were found to coincide with their analytical counterpart for both values of  $\alpha'$ . These results agree with the works of other researchers (Sakai, 2003; Stilwell and Tabor, 1961); Provided (i) the residual impression has flat sides even after elastic recovery and (ii) the reloading of impression is elastic and reversible, then the load-displacement reloading path is quadratic and may be characterized by a single geometrical parameter, in this case  $\alpha'$ . This suggests that the equivalent problem that involved solely geometrical differences is indeed valid; however, the actual unloading of a plastic imprint involves the effects of residual stresses as well, which might suggest that this sole geometrical parameter,  $\alpha'$  is sufficient to describe the equivalent indenter. This point will be discussed in more detail in the subsequent section.

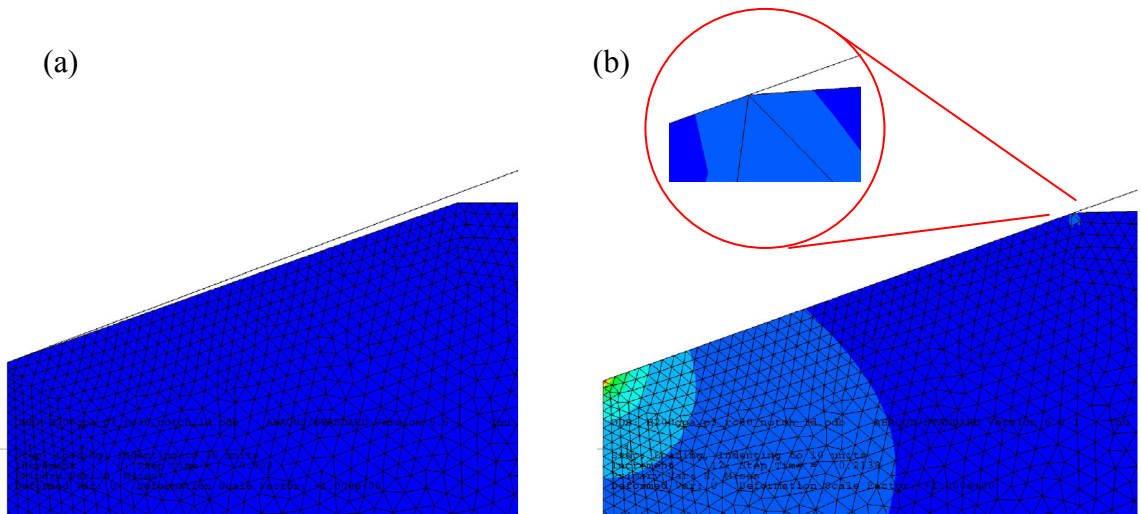


Fig. 3.7. (a) Indentation of a notched specimen. (b) At  $h_{max}$  the radius of contact is equal to the radius of the residual imprint

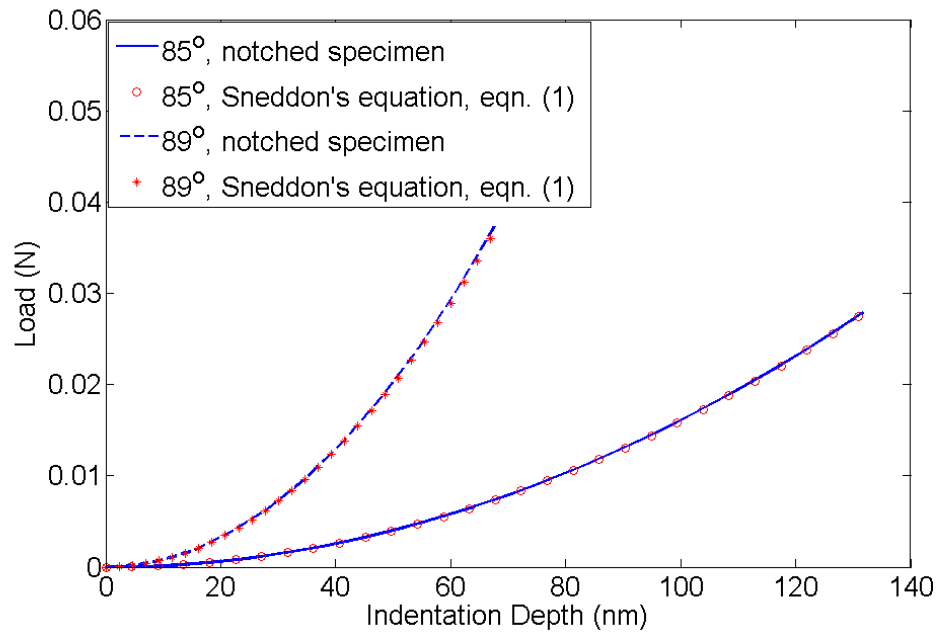


Fig. 3.8. Load-displacement curves for  $\alpha' = 85^\circ$  and  $89^\circ$

### 3.3.5. The Straightforward Application of Sneddon's Equation

Having validated the elastic unloading and equivalent problem assumption, it may seem logical to use Sneddon's elastic relation (1) directly, with an appropriate  $\alpha'$ , to take into account the plastic imprint. This will eliminate the uncertainty introduced in the measurement of the slope of the unloading load-displacement curve,  $dP/dh_e$ , which is a required parameter for the conventional derivation of the elastic modulus, as shown in (6).

The unloading curve from an elastic-plastic indentation was compared with the elastic load-displacement relationship obtained using (1), to examine the accuracy of the straightforward application of Sneddon's equation. Figure 3.9 shows the comparison between the simulated unloading curve and the elastic reloading curves with calculated and 'ideal'  $\alpha'$ s. The calculated  $\alpha'$  refers to the effective angle derived using (4), which is

found to be  $88.1^\circ$ . The ideal  $\alpha'$  refers to the effective angle that will give the correct  $E$  when substituted into (1), which is found to be  $88.9^\circ$ .

The two elastic curves obtained using (1) are observed to be distinctly different from the actual unloading curve. The curve plotted with the ideal  $\alpha'$  only meets the unloading curve at  $h_{max}$ . This suggests that the reason behind the mismatch of the curves is not due to the wrong choice of  $\alpha'$ .

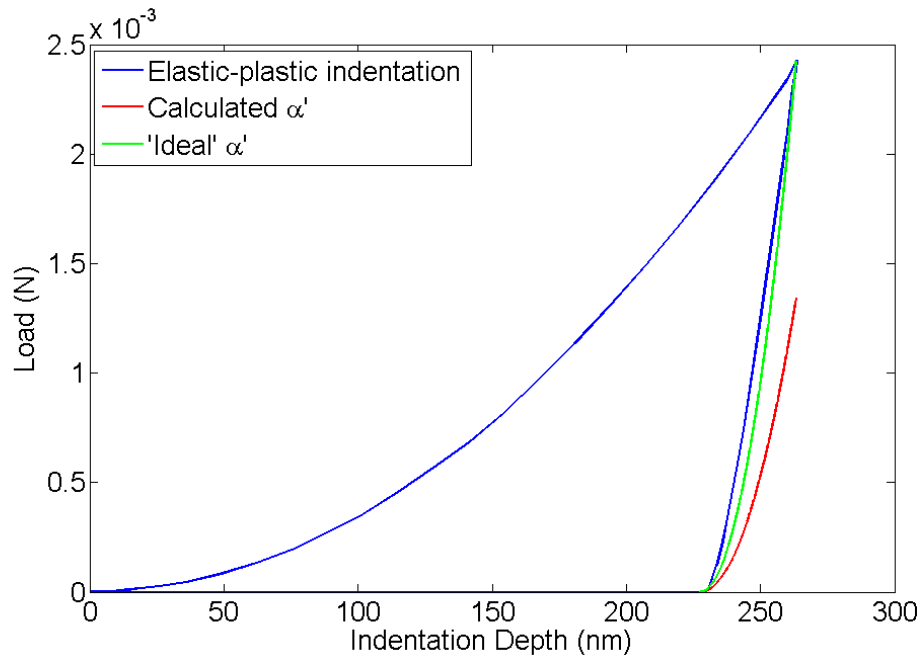


Fig. 3.9. Comparison between the simulated unloading curve and the elastic reloading curves with calculated and ‘ideal’  $\alpha$ 's

One reason for this discrepancy is the curvature of the walls of the imprint. Figure 3.10 shows profiles of the residual imprint for  $E/\sigma_y$  of 10 and 1000, respectively. From Fig. 3.10(a), it is observed that the walls of the residual imprint are not flat as assumed in the ‘equivalent’ problem. Thus, the actual problem cannot be simply described by the indentation of a notched specimen with half-angle  $\alpha$ , as illustrated in Fig. 3.2. According to Pharr et al. (2002), the effective indenter shape in this case is no longer conical, but

instead is a parabola of revolution. This is because the actual problem is now an indentation of a curved surface with a conical indenter, and following the same reasoning as the proposition of the equivalent problem before, it is expected that the equivalent problem is now an indentation of an indenter with a curved profile on a flat surface.

Hence, for elastic-plastic indentations using conical indenters, the straightforward application of Sneddon's elastic relation (1948) as shown in (1) to the unloading curve is not appropriate. The conventionally used stiffness equation, shown by (6), was demonstrated to be applicable to indenters that are bodies of revolution, and have a profile that is  $C^\infty$ , i.e., infinitely smooth (Pharr et al., 1992). Thus, it is suitable for the effective indenter shape, which was established to be a parabola of revolution. The factors affecting the accuracy of (6) are examined next.

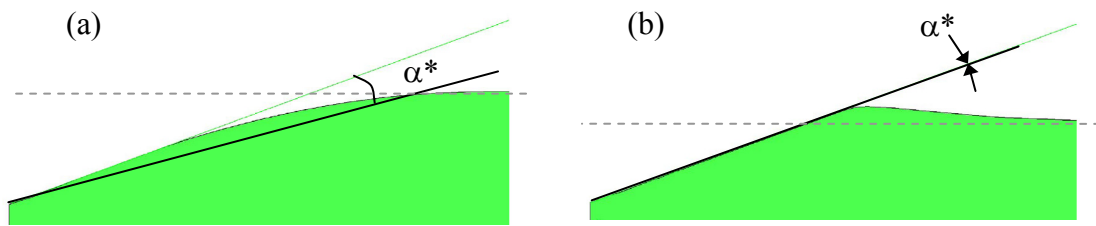


Fig. 3.10. (a) Profile of the residual imprint for  $E/\sigma_y=10$ . (b) Profile of the residual imprint for  $E/\sigma_y=1000$ .

(Note the sink-ins and pile-ups.)

### 3.3.6. Factors Affecting the Accuracy of the Stiffness Equation

#### 3.3.6.1. Residual stresses at the plastic imprint

Residual stresses are present at the plastic imprint during the unloading process of the elastic plastic indentation and they cannot be neglected. Pharr and Bolshakov (2002) introduced the concept of the effective indenter to account for the surface distortion and pressure distribution under the indenter, however, the interaction between the residual

stresses and the surface geometry of the plastic imprint and their combined effects on the shape of the effective indenter through the exponent of the unloading load-displacement relationship is not clear.

The Poisson's ratio,  $\nu$ , of the specimen is an important parameter that dictates the level of residual stresses present at the plastic imprint, as can be observed in Fig. 3.11. This figure shows that as  $\nu$  tends towards 0.5, the extent of residual equivalent stress present at the plastic imprint decreases significantly. This can be qualitatively understood in terms of the elastic constraint exerted on the plastic zone. This observation may also possibly explain why the percentage error for the extracted  $E$  using the conventional method is so much dependent on  $\nu$ , and why it decreases as  $\nu$  approaches 0.5, as observed in Fig. 3.5.

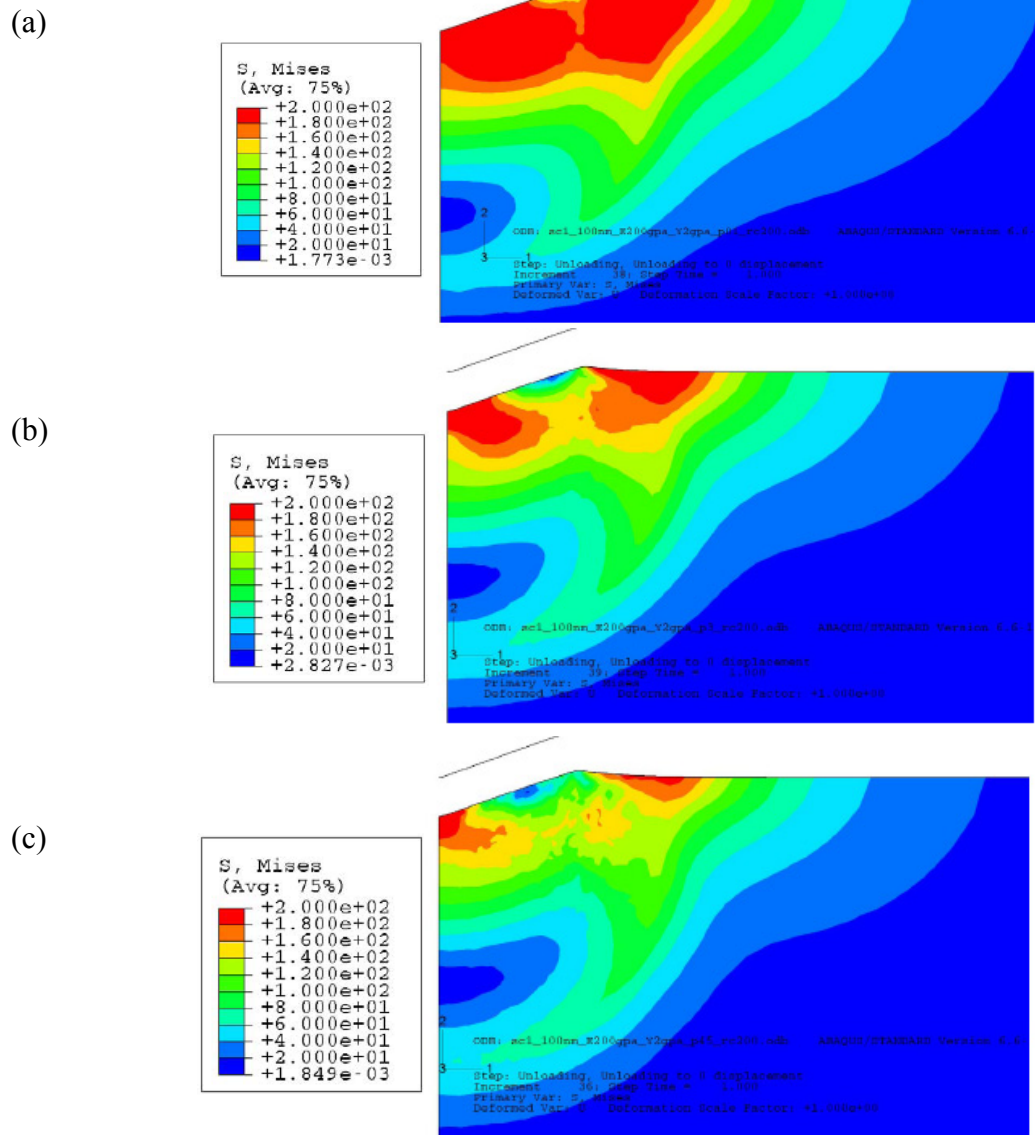


Fig. 3.11. Residual equivalent (Mises) stress fields for indentations of elastic, perfectly plastic material with  $E = 200 \text{ GPa}$ ,  $\sigma_y = 2 \text{ GPa}$ , and different  $\nu$  ( $= 0.01, 0.3$ , and  $0.45$ , respectively). (Note that the stress values must be multiplied by a factor of  $1e7$  to respect the scale of the problem.)

### 3.3.6.2. Accurate determination of $A$

#### *3.3.6.2.1. The contact depth, $h_c$*

The projected contact area,  $A$  is a function of the contact depth,  $h_c$ , through the known or measured geometry of the indenter. Thus, the accurate determination of  $h_c$  is crucial for the extraction of elastic constants using (6).

It is observed from Fig. 3.10(b) that when  $E/\sigma_y$  is large and the hardening coefficient  $n$  is small, there are pile-ups around the plastic imprint. This will result in the actual contact depth,  $h_c$ , deviating significantly from that derived by (8). This deviation has been studied extensively and found to be more than 30% in some cases (Cheng and Cheng, 2004). While some researchers may argue that pile-ups are only significant when  $h_r/h_{max} > 0.7$  (Oliver and Pharr, 2004), this criterion corresponds to  $E/\sigma_y > 30$ , for elastic-perfectly plastic materials, using (10), and is also evidenced by the numerical simulations of Pharr and Bolshakov (2002). This stringent criterion severely limits the applicability of (8) to accurately determine  $h_c$  for typical materials.

#### *3.3.6.2.2. Finite tip radius of the indenter*

It has been established in the previous chapter that in the case of a linearly elastic indentation, finite tip radius effects are significant. Unlike the elastic case, the loading and unloading segments for the elastic-plastic indentation do not coincide. Thus, the effects of the finite tip radius of the indenter,  $\rho$ , will be discussed separately for the loading and unloading stages of the elastic-plastic indentation.

The loading curve of the elastic-plastic indentation is expected to be sensitive to finite tip radius effects. Similar to the arguments for the indentation of linearly elastic solids, a blunt indenter is expected to require a larger force to penetrate to a fixed

arbitrary depth. In addition,  $\rho$  will affect the projected contact area,  $A$ , at the maximum indentation depth. These effects have been extensively studied by researchers (Cheng and Cheng, 1998; Troyon and Huang, 2004).

On the other hand, the unloading curve of the elastic-plastic indentation is expected to be insensitive to finite tip radius effects. This is evidenced by two observations. First, it is observed that for a typical range of  $E/\sigma_y$  between 100 and 1000, the effective half-angle,  $\alpha'$  is between  $88^\circ$  and  $89.7^\circ$ . As  $\alpha'$  tends to  $90^\circ$ , the effect of  $\rho$  is expected to become less dominant. This phenomenon can be interpreted from the location of the transition point,  $h_a$ , given by,

$$h_a = \rho (1 - \sin \alpha') \quad (12)$$

where  $h_a$  is defined as the depth which the spherical tip (with radius =  $\rho$ ) is tangential to the sides of the cone with half-angle,  $\alpha'$ . As  $\alpha'$  tends towards  $90^\circ$ ,  $h_a$  becomes vanishingly small, regardless of the tip radius. This suggests that the finite tip radius of the indenter does not play a dominant role in the elastic unloading/reloading process of the indentation.

For situations where the walls of the plastic imprint may not be described by a single geometrical parameter,  $\alpha'$ , the effect of  $\rho$  can be explained with the pressure distribution under the indenter. Pharr and Bolshakov (2002) demonstrated that the pressure distribution under the indenter at peak load is relatively constant and suggested that the equivalent problem amounts to the indentation of an elastic flat half-space with an effective parabolic indenter. The effective parabolic indenter takes no account of the local  $\rho$ , which also suggests that the finite tip radius effects are unlikely to affect the elastic unloading curve significantly.

However, one should keep in mind that unloading follows active loading for which the finite tip radius does indeed affect the projected area of contact,  $A$ . The latter, in turn, determines the accuracy of the conventional method for the extraction of elastic properties of the material. These results are tabulated in Tables 3.1 and 3.3 in the Appendix.

### 3.4. PROPOSED TECHNIQUE

Load and displacement measurements are recorded during nanoindentation experiments. The slope of the unloading segment can be easily derived from the load-displacement curve leaving the projected contact area,  $A$ , as the only unknown in (6). Therefore, the primary challenge to reduce the errors involved in the derivation of the reduced modulus  $E_r$ , lies in the accurate measurements of the projected contact area,  $A$ .

As discussed in the previous section, the accurate determination of  $A$  is dependent on the accurate derivation of  $h_c$  and  $\rho$ . Pile-ups, as shown in Fig. 3.12, underestimate  $h_c$  and thus underestimate the actual projected contact area,  $A$ . For elastic-plastic materials that strain-harden, it has been shown that the extent of hardening reduces the amount of pile-ups, and it is even possible for the material to sink-in (Cheng and Cheng, 1999), i.e., (8) overestimates  $h_c$ .

The neglect of finite tip radius effects will result in the underestimation of  $A$  as well. Suppose a conical indenter with a finite tip radius may be represented by a cone with a spherical cap; the projected contact area,  $A$ , is given by (Troyon and Huang, 2004),

$$A = \pi \tan^2 \alpha (h_c + h_b)^2 \quad (13)$$

where  $h_b$  is the blunting distance, which is the distance between the supposed apex of the cone and the spherical cap. Since  $h_b$  is a positive variable that represents the finite tip radius effects, if neglected it will result in an underestimation of the projected contact area,  $A$ .

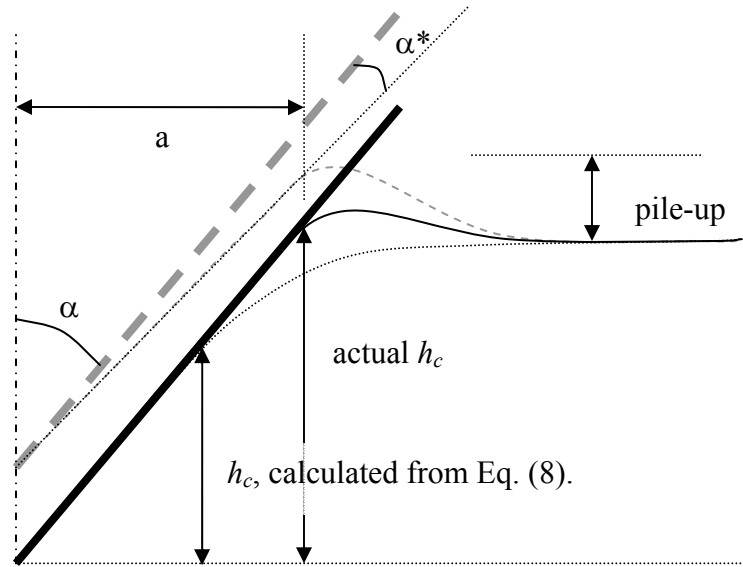


Fig. 3.12. Schematic of an elastic-plastic indentation

Although it is clear that the accurate determination of the projected contact area,  $A$ , is central to the accurate extraction of  $E_r$ , such a determination is currently missing. The accurate determination of the tip radius of the indenter,  $\rho$ , is not a trivial task, yet, even with an accurate knowledge of  $\rho$ , one still requires the knowledge of  $h_c$  to accurately determine  $A$ . It is established that  $h_c$  is affected by pile-ups and sink-ins that are themselves determined by the material constitutive behavior, which is precisely what one seeks to characterize using nanoindentations. Proposed methods to approximate  $h_c$ , are often valid for a certain range of material properties, which might result in a severe overestimation or underestimation of the material property values (Tranchida et al., 2006). Thus, the subsequent section proposes an experimental technique to measure the projected contact area,  $A$ , *directly* without any assumptions or restrictions on material properties.

### 3.4.1. Measurement of the Projected Contact Area using Electrical Resistance Method

A simple methodology is proposed for the *in situ* measurement of the contact area,

A. It is based on the following 2 steps:

- a. Determine  $r$ , the specific electrical contact resistance between the tip and the substrate. For this, bring a cylindrical (or equivalently well defined) conductive tip of known cross-sectional area in contact with the sample.
- b. Using a conventional tip (such as Berkovich) with the same material as the tip used in the calibration, the measured current is directly related to the surface area of contact,  $A_s$ , using the relation  $I = A_s r$ . The projected area of contact,  $A$ , can then be inferred from  $A_s$ , based on the known geometry of the indenter.

The proposed method is simple and straightforward. The measured projected area takes into account any pile-ups or sink-ins associated with the properties of the sample.

Figure 3.13(a) shows the load-displacement curves for the indentations of polycrystalline gold, using a Berkovich tip, and Fig. 3.13(b) shows the corresponding *in situ* measurement of the current-displacement curves. Figure 3.13(b) was discretized and fitted with a quadratic curve with no linear term. The current-displacement relation is well described by the fitted quadratic curve, as expected ( $R^2 = 0.994$ ). The current is expected to increase with surface contact area, which varies with the square of indentation depth. Thus, the current measured across the tip/specimen contact should vary proportionally with the square of the indentation depth. It is also observed that at shallow indentation depths, the current does not fit as well to the quadratic curve. This is probably due to the finite tip radius of the indenter. Granted  $r$ , the tip radius of the

indenter,  $\rho$ , can be inferred from the current measurements as well. This preliminary analysis shows that the proposed methodology for the measurement of projected contact area,  $A$ , is very promising.

While this proposed technique assumes that the electrical resistance of the material and indenter tip does not change during indentation, it is important to note this assumption may not hold for some materials. For these materials, phase changing or formation of shear bands, or even presence of surface asperities were found to affect the contact resistance measurement, as discussed by researchers such as Mann et al. (2002) and Ruffell et al. (2007).

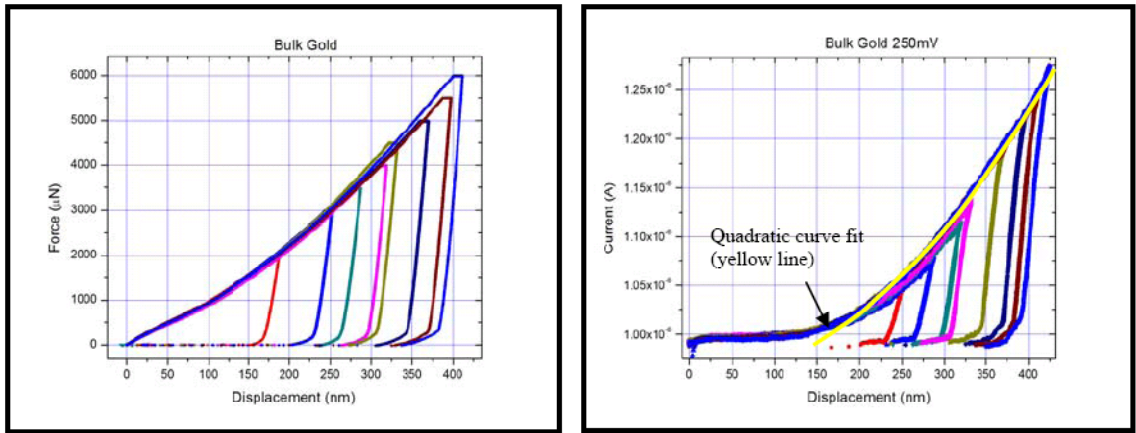


Fig. 3.13. (a) Load-displacement curves for the indentations of polycrystalline Gold (Au); (b) Corresponding current-displacement curves for the indentations (courtesy of Hysitron (Vodnick, 2007))

### 3.4.2. Reduction of Errors with Accurate Measurement of $A$

To investigate the reduction of errors from the accurate measurement of  $A$ , the Young's modulus,  $E$  (with *a priori* knowledge of  $\nu$ ), was calculated using (6) with accurate measurements of  $A$  from the numerical simulations. The results are tabulated in Tables 3.6 and 3.7 in the Appendix.

Figure 3.14 plots the percentage error,  $\varepsilon$ , vs.  $E/\sigma_y$  for the range of  $\nu$  (0.01, 0.3, and 0.47) and  $\rho$  (30 nm and 150 nm), using  $A$ , calculated from (7) and measured directly in the simulations. It is observed that for the range of  $E/\sigma_y$  relevant to most materials, i.e., between 100 and 1000,  $\varepsilon$  is reduced by more than 50%. It is also observed that when  $E/\sigma_y$  is small, the difference between  $A$  calculated using (7) and that measured in the simulation is not significant. When  $E/\sigma_y$  is small (say,  $< 30$ ), the extent of plasticity is not prevalent and the  $h_r/h_{max} < 0.7$  criterion for the accurate use of (8) is fulfilled. Hence, the measured value of  $A$  is expected to be similar to that derived using elastic relations. In addition, when the accurate value of  $A$  is used,  $\varepsilon$  is observed to be relatively insensitive to  $E/\sigma_y$ , which suggests an accurate determination of  $A$  eliminates the effects from plasticity.

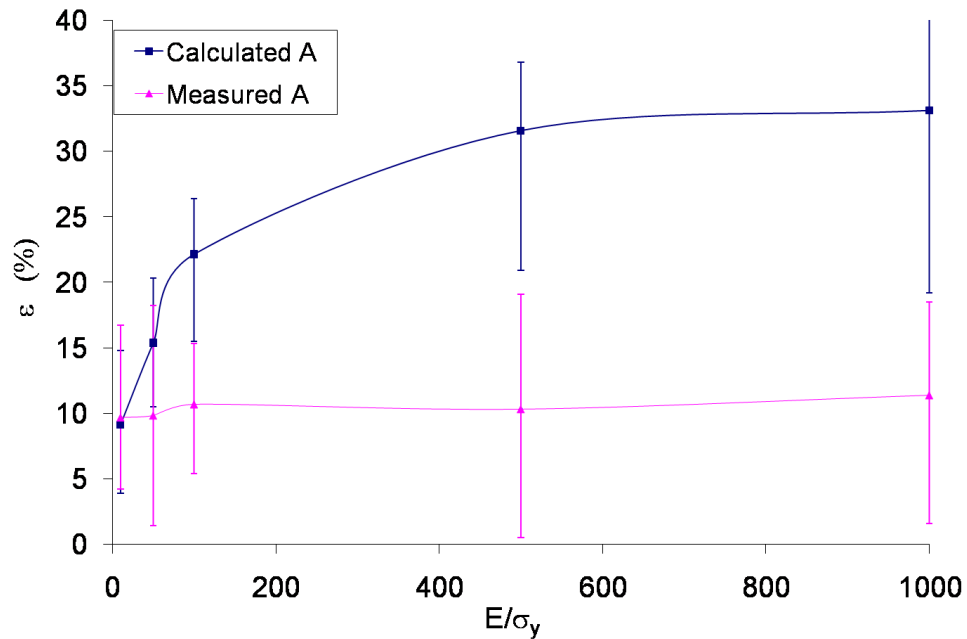


Fig. 3.14.  $\varepsilon$  vs.  $E/\sigma_y$ , using calculated and “measured” values for  $A$ . The bars correspond to the calculated range of  $\varepsilon$  for values of  $\nu$  ( $= 0.01, 0.3, 0.47$ ) and  $\rho$  ( $= 30 \text{ nm}, 150 \text{ nm}$ ). Exact values are tabulated in Tables

3.1, 3.3, 3.6, and 3.7

The percentage error of the extracted  $E$ ,  $\varepsilon$ , is also found to be insensitive to the tip radius of the indenter when the accurate projected area,  $A$ , was used in the extraction of  $E$ , as can be observed from Fig. 3.15. This result confirms the previous hypothesis that the finite tip radius of the indenter only affects the accurate determination of  $A$ .

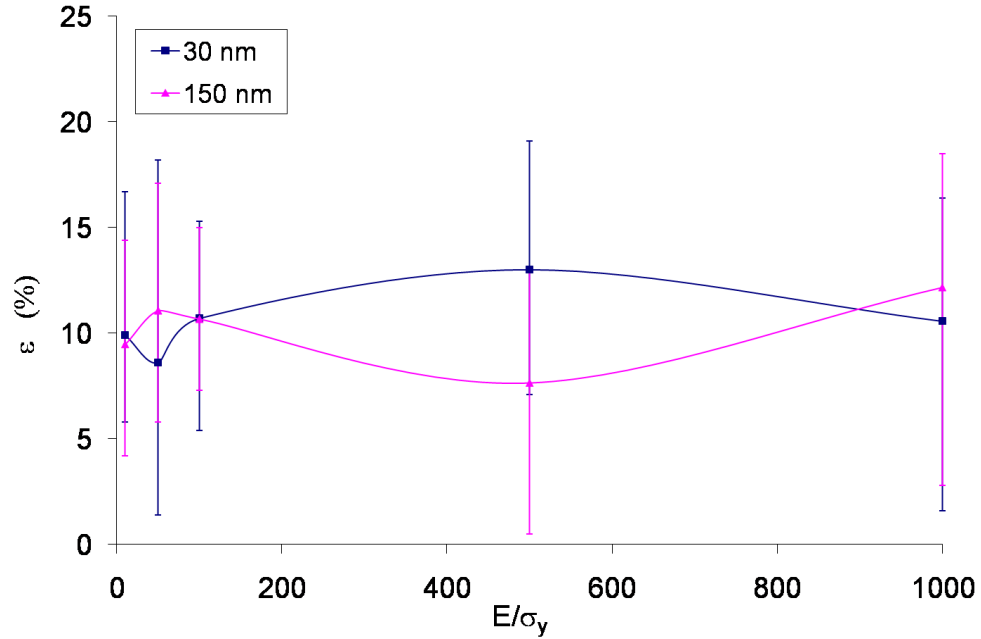


Fig. 3.15.  $\varepsilon$  vs.  $E/\sigma_y$ , using “measured” values for  $A$  for  $\rho = 30 \text{ nm}$  and  $150 \text{ nm}$ . The bars correspond to the range of  $\varepsilon$  for values of  $\nu$  ( $= 0.01, 0.3, 0.47$ ). Exact values are tabulated in Tables 3.6 and 3.7

From Fig. 3.16, it is observed that the percentage error of the extracted  $E$ , using the measured  $A$ , remains sensitive to  $\nu$ . This suggests that this error associated with  $\nu$  is independent of the accurate determination of  $A$ . Though it has been shown that the extent of residual stress at the plastic imprint is sensitive to  $\nu$  of the indented material, it is not clear how the residual stresses affect the accuracy of the extracted elastic properties of interest.

For linearly elastic indentations, it was established in Chapter 2 that the correction factor,  $\beta$ , is the product of the first correction factor term,  $f(\nu)$  due to radial displacement

(Hay et al., 1999) and a form factor essentially related to the geometry of contact. For elastic-plastic indentations, the present discussion assumed that the projected contact area,  $A$  is accurately determined. Hence, in the context of  $\beta$  in the linearly elastic case, the form factor is effectively unity. Furthermore,  $\varepsilon$  for the elastic-plastic indentations is observed to be relatively insensitive to  $E/\sigma_y$  and  $\rho$ , such that  $\varepsilon$  may be interpreted as a function of only  $\nu$ . Figure 3.17 compares the correction factor,  $f(\nu)$  associated with  $\nu$  in elastic and elastic-plastic indentations. It is observed that  $f(\nu)$  for both cases are rather similar, although  $f(\nu)_{\text{elastic-plastic}}$  is observed to be consistently larger than  $f(\nu)_{\text{elastic}}$ . It is important to note that  $f(\nu)_{\text{elastic}}$  is attributed to the negligence of radial displacement in Sneddon's derivation, whereas  $f(\nu)_{\text{elastic-plastic}}$  is likely associated with the residual stress field around the plastic imprint due to elastic confinement. In the case for elastic-plastic indentations, the effective half-angle,  $\alpha'$  is very large ( $> 88^\circ$  for common materials) for the elastic unloading curve, thus the error dependent on  $\nu$  is unlikely due to the negligence of lateral displacement as demonstrated by the work of Hay et al. (1999). Moreover, it is clear that in the limiting case of a flat punch, the induced lateral displacement would be zero. The slight difference between the correction factors in Fig. 3.17 could suggest why significant errors are not observed even when these correction factors are used interchangeably.

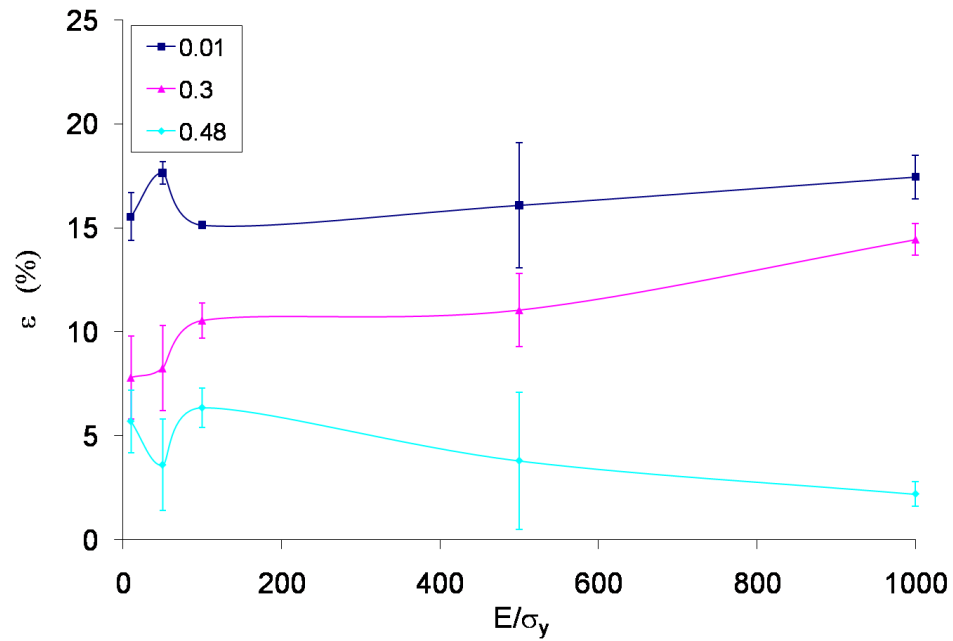


Fig. 3.16.  $\varepsilon$  vs.  $E/\sigma_y$  using “measured” values for  $A$  for  $\nu$  ( $= 0.01, 0.3$  and  $0.47$ ). The bars correspond to the range of  $\varepsilon$  for values of  $\rho$  ( $= 30 \text{ nm}$  and  $150 \text{ nm}$ ). Exact values are tabulated in Tables 3.6 and 3.7

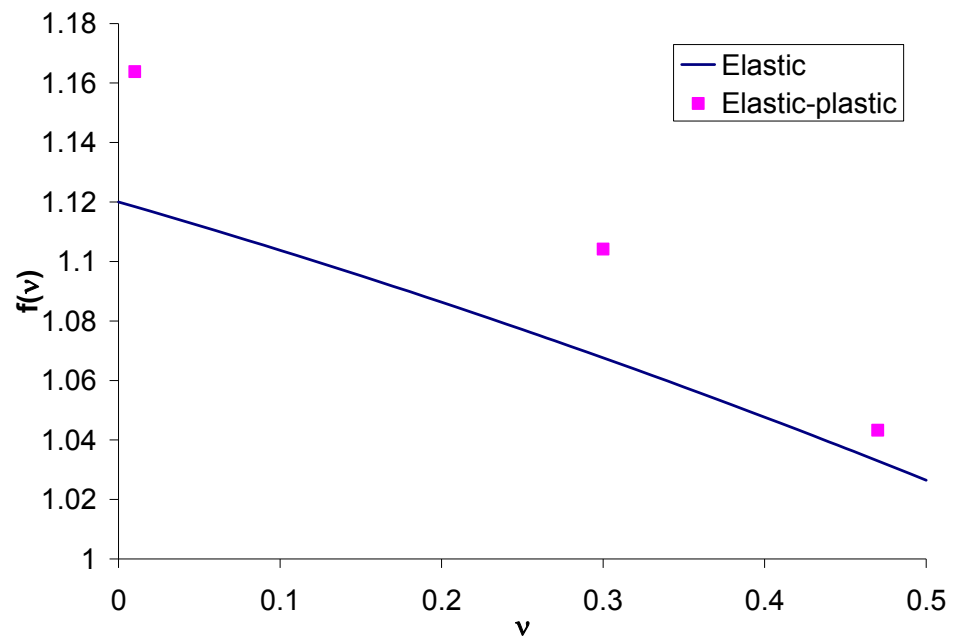


Fig. 3.17. Comparison between the correction factor,  $f(\nu)$ , between elastic and elastic-plastic indentations

It is important to note that there are still secondary sources of error in the derivation of elastic constants. One important source of error lies in the measurement of the slope of the unloading curve. Despite measures taken to reduce them, such as curve fitting, an uncertainty of up to 5% can be introduced to the measurement of the slope. This uncertainty will then be propagated to the value of  $E_r$ .

### 3.5. SUMMARY AND CONCLUSIONS

The conventional method of deriving elastic constants using nanoindentation of elastic-plastic materials has been critically examined using numerical simulations and experiments. The main results of this study are summarized below:

The effective half-angle,  $\alpha'$  has been identified to be a function of  $E/\sigma_y$ , as shown in Fig. 3.3. For a typical material,  $E/\sigma_y$  ranges between 100 and 1000, thus its corresponding  $\alpha'$  ranges between  $88^\circ$  and  $89.7^\circ$ . However, this single geometrical parameter  $\alpha'$  cannot adequately represent the residual stress field, which is a function of Poisson's ratio of the specimen,  $\nu$  that characterizes the unloading stage of the elastic-plastic imprint. Consequently, Sneddon's load-displacement relationship for the conical indenter (1) cannot effectively describe the elastic unloading curve of an elastic-plastic indentation. Therefore, it seems preferable to use the elastic relationship for axially symmetric indenters with a smooth profile (6). Yet, (6) requires an accurate determination of the projected area of contact,  $A$ . The latter may be inferred analytically provided  $h_r/h_{max} < 0.7$ , but for an elastic-perfectly plastic material, this criterion is equivalent to  $E/\sigma_y < 30$ , which is quite limited in scope for most materials of interest. Pile-ups and sink-ins will also affect the accuracy of  $h_c$ , and thus  $A$ , but they are in turn determined by the very mechanical properties of the investigated material, which are to be determined. In addition,  $A$  is also found to be a function of the indenter's tip-radius,  $\rho$ , through the elastic-plastic loading stage of the indentation cycle. Therefore, an alternative approach is proposed, in which  $A$  is measured directly, using electrical methods. The viability of this method has been verified based on experimental results. Once  $A$  is

accurately determined, one observes that the percentage error of the extracted Young's modulus is insensitive to  $E/\sigma_y$  and  $\rho$  as expected, but it is still sensitive to  $\nu$ .

Concerning the determination of the yield strength of the material, a power law relationship was identified between  $h_e/h_{max}$  and  $E/\sigma_y$  in (10). This relation was verified experimentally and found to provide an upper bound for the yield stress of pressure sensitive and/or strain hardening materials.

In conclusion,

- The direct application of Sneddon's solution for elastic-plastic indentations is not as appropriate as the conventional method (6).
- The residual stress field around the plastic imprint is found to be sensitive to the Poisson's ratio,  $\nu$ . Higher values of  $\nu$  correspond to lower residual stresses.
- An accurate determination of the projected contact area,  $A$ , will reduce the errors in the extracted value of  $E$  by more than 50% for typical elastic-plastic solids.
- The projected contact area,  $A$ , is found to be not only related to  $h_c$  but also to  $E/\sigma_y$  and  $\rho$  as well.
- A new experimental procedure to directly measure the projected contact area,  $A$  is proposed.
- A new methodology to extract the yield stress of materials using nanoindentation has been proposed.

## REFERENCES

- Atkins, A.G., Tabor, D., 1966. Hardness and deformation properties of solids at very high temperatures. *Proc. Roy. Soc. A292*, 441–459.
- Bower, A.F., Fleck, N.A., Neddleman, A., Ogbonna, N., 1993. Indentation of a power-law creeping solid. *Proc. R. Soc. A441*, 97–124.
- Bulychev, S.I., Alekhin, V.P., Shorshorov, M.K., Ternovskii, A.P., Shnyrev, G.D., 1975. Determining Young's Modulus from the Indentor Penetration Diagram. *Zavodskaya Laboratoriya* 41 (9), 1137–1140.
- Cheng, Y.T., Cheng, C.M., 1998. Further analysis of indentation loading curves: Effects of tip rounding on mechanical property measurements. *J. Mater. Res.* 13 (4), 1059–1064.
- Cheng, Y.T., Cheng, C.M., 1999. Scaling Relationships in Conical Indentation of Elastic Perfectly Plastic Solids. *Int. J. Solids Structures* 36, 1231–1243.
- Cheng, Y.T., Cheng, C.M., 2004. Scaling, dimensional analysis, and indentation measurements. *Mat. Sci. and Engng. R* 44, 91–149.
- Fischer-Cripps, A.C., 2004. *Nanoindentation*. Springer.
- Hansen, N., Huang, X., 1998. Microstructure and Flow stress of Polycrystals and Single Crystals. *Acta Materialia* 46 (5), 1827–1836.
- Hay, J.C., Bolshakov, A., Pharr, G.M., 1999. A Critical Examination of the Fundamental Relations Used in the Analysis of Nanoindentation Data. *J. Mater. Res.* 14, 2296–2305.

Hill, R., Lee, E.H., Tupper, S., 1947. The Theory of Wedge Indentation of Ductile Materials. Proc. R. Soc. Lond. A 188 (1013), 273–289.

Kutty, T.R.G., Ganguly, C., Sastry, D.H., 1996. Development of creep curves from hot indentation hardness data. Scripta Materialia 34 (12), 1833–1838.

Lawn, B.R., Evans, A.G., Marshall, D.B., 1980. Elastic/plastic indentation damage in ceramics: The median/radial crack system. J. American Ceramic Soc. 63 (9–10), 574–581.

Loubet, J.L., Georges, J.M., Marchesini, O., Meille, G., 1984. Vickers Indentation Curves of Magnesium Oxide {MgO}. J. Tribol-T ASME 106, 43–48.

Mann, A.B., Heerden, D.V., Pethica, J.B., Bowes, P., Weihs, T.P., 2002. Contact resistance and phase transformations during nanoindentation of silicon. Philos. Mag. A 83 (10), 1921–1929.

Martin, M., Troyon, M., 2002. Fundamental relations used in nanoindentation: Critical examination based on experimental measurements. J. Mater. Res. 17 (9), 2227–2234.

Mayo, M.J., Nix, W.D., 1988. A microindentation study of superplasticity in Pb, Sn, and Sn-38wt%Pb. Acta Metall. 36 (8), 2183–2192.

Miyake, K., Fujisawa, S., Korenaga, A., Ishida, T., Sasaki, S., 2004. The Effect of Pile-up and Contact Area on Hardness Test by Nanoindentation. Jap. J. of Appl. Phys. 43 (7B), 4602–4605.

Newey, D., Wilkins, M.A., Pollock, H.M., 1982. An Ultra-Low-Load Penetration Hardness Tester. J. Phys. E: Sci. Instrum. 15, 119–122.

Oliver, W.C., Pharr, G.M., 2004. Review: Measurement of Hardness and Elastic Modulus by Instrumented Indentation: Advances in Understanding and Refinements to Methodology. *J. Mater. Res.* 19, 3–20.

Palmqvist, S., 1957. A method to determine the toughness of brittle materials, especially hard materials. *Jernkontorets Ann.* 141, 303–307.

Payzant, E.A., King, H.W., Gupta, S.D., Jacobs, J.K., 1993. Hot hardness of ceramic cutting tools using depth of penetration measurements. In: Mostaghaci, H., Drew, R.A.L. (Eds.), *Development and Applications of Ceramics and New Metal Alloys*. Canadian Institute of Mining and Metallurgy, Montreal, pp. 399–408.

Pethica, J.B., Hutchings, R., Oliver, W.C., 1983. Hardness Measurement at Penetration Depths as Small as 20 Nm. *Philos. Mag. A* 48, 593–606.

Pharr, G.M., Bolshakov, A., 2002. Understanding Nanoindentation Unloading Curves. *J. Mater. Res.* 17, 2660–2671.

Pharr, G.M., Oliver, W.C., Brotzen, F.R., 1992. On the Generality of the Relationship Among Contact Stiffness, Contact Area, and the Elastic Modulus During Indentation. *J. Mater. Res.* 7 (3), 613–617.

Ruffell, S., Bradby, J.E., Williams, J.S., Warren, O.L., 2007. An in situ electrical measurement technique via a conducting diamond tip for nanoindentation in silicon. *J. Mater. Res.* 22 (3), 578–586.

Sakai, M., 2003. Elastic recovery in the unloading process of pyramidal microindentation. *J. Mater. Res.* 18 (7), 1631–1640.

Shiwa, M., Weppelmann, E.R., Munz, D., Swain, M.V., Kishi, T., 1996. Acoustic emission and precision force-displacement observations on pointed and spherical indentation of silicon and TiN film on silicon. *J. Mater. Sci.* 31, 5985–5991.

Sneddon, I.N., 1948. Boussinesq's Problem for a Rigid Cone. *Proc. Cambridge Philos. Soc.*, 492–507.

Stilwell, N.A., Tabor, D., 1961. Elastic recovery of conical indentations. *Proceedings of the Physical Society of London* 78 (500), 169.

Storåkers, B., Larsson, P.L., 1994. On Brinell and Boussinesq Indentation of Creeping Solids. *J. Mech. Phys. Solids* 42, 307–332.

Tabor, D., 1948. A Simple Theory of Static and Dynamic Hardness. *Proc. R. Soc. Lond.* A 192 (1029), 247–274.

Tabor, D., 1951. *The Hardness of Metals*. Oxford University Press, Cambridge, Great Britain.

Ternovskii, A.P., Alekhin, V.P., Shorshorov, M.K., Khrushchov, M.M., Skvortsov, V.N., 1974. Micromechanical Testing of Materials by Depression. *Zavodskaya Laboratoriya* 39 (10), 1242–1247.

Tranchida, D., Piccarolo, S., Loos, J., Alexeev, A., 2006. Accurately evaluating Young's modulus of polymers through nanoindentations: A phenomenological correction factor to Oliver and Pharr procedure. *Appl. Phys. Lett* 89, 171901–171905.

Troyon, M., Huang, L., 2004. Correction factor for contact area in nanoindentation measurements. *J. Mater. Res.* 30 (3), 610–617.

Tymiak, N.I., Daugela, A., Wyrobek, T.J., Warren, O.L., 2003. Highly localized acoustic emission monitoring of nanoscale indentation contacts. *J. Mater. Res.* 18 (4), 784–796.

Vodnick, D.J., 2007. Force vs. Displacement and Current vs. Displacement plots for polycrystalline Gold. Personal communication.

## APPENDIX

$E/\sigma_y$	$h_e$ (nm)	$\alpha'$	Calculated $E$ (GPa)	% Error
<b><math>E = 50</math> GPa, <math>\nu = 0.01</math>, <math>\rho = 30</math> nm</b>				
10	135.3	$80.7^\circ$	55.6	11.3
50	55.53	$86.9^\circ$	58.1	16.3
100	34.15	$88.2^\circ$	61.8	23.7
500	10.48	$89.5^\circ$	68.4	36.8
1000	7.03	$89.7^\circ$	69.6	39.3
<b><math>E = 50</math> GPa, <math>\nu = 0.3</math>, <math>\rho = 30</math> nm</b>				
10	161.68	$78.6^\circ$	53.4	6.8
50	56.48	$86.8^\circ$	56.7	13.3
100	35.95	$88.1^\circ$	61.3	22.5
500	11.95	$89.4^\circ$	64.5	29.0
1000	7.41	$89.6^\circ$	64.7	29.4
<b><math>E = 50</math> GPa, <math>\nu = 0.47</math>, <math>\rho = 30</math> nm</b>				
10	161.68	$78.5^\circ$	51.9	3.9
50	61.57	$86.5^\circ$	55.2	10.5
100	32.95	$88.2^\circ$	60.8	21.6
500	9.57	$89.5^\circ$	64.9	30.0
1000	6.47	$89.4^\circ$	59.6	19.2

**Table 3.1.** Varying Poisson's ratio,  $\nu$ , with  $E = 50$  GPa and  $\rho = 30$  nm

$E/\sigma_y$	$h_e$ (nm)	$\alpha'$	Calculated $E$ (GPa)	% Error
<b><math>E = 10</math> GPa, <math>\nu = 0.3</math>, <math>\rho = 30</math> nm</b>				
10	161.68	78.6°	10.7	6.61
50	56.47	86.8°	11.5	14.7
100	35.95	88.1°	12.4	24.3
500	11.95	89.4°	13.2	32
1000	7.41	89.6°	13.1	31
<b><math>E = 50</math> GPa, <math>\nu = 0.3</math>, <math>\rho = 30</math> nm</b>				
10	161.68	78.6°	53.4	6.8
50	56.48	86.8°	56.7	13.3
100	35.95	88.1°	61.3	22.5
500	11.95	89.4°	64.5	29.0
1000	7.41	89.6°	64.7	29.4
<b><math>E = 100</math> GPa, <math>\nu = 0.3</math>, <math>\rho = 30</math> nm</b>				
10	161.68	78.6°	106.1	6.1
50	56.47	86.8°	113.3	13.3
100	35.95	88.1°	123.6	23.6
500	11.95	89.4°	129.9	29.9
1000	7.41	89.6°	131.4	31.4

**Table 3.2. Varying Young's modulus,  $E$ , with  $\nu = 0.3$  and  $\rho = 30$  nm**

$E/\sigma_y$	$h_e$ (nm)	$\alpha'$	Calculated $E$ (GPa)	% Error
<b><math>E = 50</math> GPa, <math>\nu = 0.01</math>, <math>\rho = 150</math> nm</b>				
10	138.64	80.4°	57.4	14.8
50	53.26	87.0°	60.1	20.3
100	34.50	88.2°	63.2	26.4
500	10.48	89.5°	68.4	36.8
1000	6.02	89.7°	74.8	49.6
<b><math>E = 50</math> GPa, <math>\nu = 0.3</math>, <math>\rho = 150</math> nm</b>				
10	161.68	78.4°	55.3	10.5
50	58.82	86.7°	58.6	17.3
100	36.33	88.1°	61.6	23.2
500	11.50	89.4°	68.0	36.0
1000	6.36	89.7°	69.4	38.9
<b><math>E = 50</math> GPa, <math>\nu = 0.47</math>, <math>\rho = 150</math> nm</b>				
10	161.68	78.4°	53.8	7.7
50	58.79	86.7°	57.3	14.7
100	37.22	88.0°	57.8	15.5
500	13.05	89.3°	60.5	20.9
1000	10.14	89.5°	61.2	22.3

**Table 3.3. Varying Poisson's ratio,  $\nu$ , with  $E = 50$  GPa and  $\rho = 150$  nm**

$E/\sigma_y$	$h_e$ (nm)	$\alpha'$	Calculated $E$ (GPa)	% Error
<b><math>E = 10</math> GPa, <math>\nu = 0.3</math>, <math>\rho = 150</math> nm</b>				
10	161.68	78.4°	11.0	10.4
50	58.82	86.7°	11.7	16.6
100	36.33	88.1°	12.4	24.1
500	11.50	89.4°	13.8	38.0
1000	6.36	89.7°	14.5	44.9
<b><math>E = 50</math> GPa, <math>\nu = 0.3</math>, <math>\rho = 150</math> nm</b>				
10	161.68	78.4°	55.3	10.5
50	58.82	86.7°	58.6	17.3
100	36.33	88.1°	61.6	23.2
500	11.50	89.4°	68.0	36.0
1000	6.36	89.7°	69.4	38.9
<b><math>E = 100</math> GPa, <math>\nu = 0.3</math>, <math>\rho = 150</math> nm</b>				
10	161.68	78.4°	110.4	10.4
50	58.82	86.7°	117.3	17.3
100	36.33	88.1°	125.3	25.3
500	11.50	89.4°	138.0	38.0
1000	6.36	89.7°	139.9	39.9

**Table 3.4. Varying Young's modulus,  $E$ , with  $\nu = 0.3$  and  $\rho = 150$  nm**

<b>Specimen</b>	<b>Number of experiments</b>	<b><math>E/\sigma_y</math> (from known values)</b>	<b>Mean (<math>h_e/h_{max}</math> from experiments)</b>	<b>Standard Deviation (<math>h_e/h_{max}</math> from experiments)</b>
<b>Aluminum</b>	12	1750	0.0181	0.0055
<b>Fused Quartz</b>	6	68.2	0.5609	0.0171
<b>Pt BMG</b>	12	67.7	0.2516	0.0356
<b>Homalite</b>	14	79.9	0.5900	0.0938
<b>Silicon</b>	3	145.5	0.6305	0.0087

**Table 3.5. Statistical variation for nanoindentation experiments**

$E/\sigma_y$	Calculated $A$ ( $\mu\text{m}^2$ )	“Measured” $A$ ( $\mu\text{m}^2$ )	Calculated $E$ (with “measured” $A$ ) (GPa)	% Error
<b><math>E = 50 \text{ GPa}, \nu = 0.01, \rho = 30 \text{ nm}</math></b>				
10	0.87	0.79	58.4	16.7
50	1.33	1.28	59.1	18.2
100	1.47	1.69	57.7	15.3
500	1.64	2.17	59.5	19.1
1000	1.67	2.39	58.2	16.4
<b><math>E = 50 \text{ GPa}, \nu = 0.3, \rho = 30 \text{ nm}</math></b>				
10	0.81	0.82	52.9	5.8
50	1.3	1.48	53.1	6.2
100	1.46	1.77	55.7	11.4
500	1.64	2.16	56.2	12.8
1000	1.67	2.16	56.9	13.7
<b><math>E = 50 \text{ GPa}, \nu = 0.47, \rho = 30 \text{ nm}</math></b>				
10	0.81	0.76	53.6	7.2
50	1.31	1.56	50.7	1.4
100	1.48	1.97	52.7	5.4
500	1.65	2.42	53.6	7.1
1000	1.67	2.45	49.2	1.6

**Table 3.6.** Calculated  $E$  with “measured”  $A$ , for different  $\nu$ , with  $\rho = 30 \text{ nm}$

$E/\sigma_y$	Calculated $A$ ( $\mu\text{m}^2$ )	“Measured” $A$ ( $\mu\text{m}^2$ )	Calculated $E$ (with “measured” $A$ ) (GPa)	% Error
<b><math>E = 50 \text{ GPa}, \nu = 0.01, \rho = 150 \text{ nm}</math></b>				
10	0.85	0.86	57.2	14.4
50	1.32	1.41	58.5	17.1
100	1.46	1.76	57.5	15.0
500	1.64	2.42	56.5	13.1
1000	1.67	2.66	59.3	18.5
<b><math>E = 50 \text{ GPa}, \nu = 0.3, \rho = 150 \text{ nm}</math></b>				
10	0.79	0.80	54.9	9.8
50	1.3	1.46	55.1	10.3
100	1.45	1.86	54.9	9.7
500	1.64	2.62	54.7	9.3
1000	1.67	2.63	57.6	15.2
<b><math>E = 50 \text{ GPa}, \nu = 0.47, \rho = 150 \text{ nm}</math></b>				
10	0.79	0.85	52.1	4.2
50	1.30	1.53	52.9	5.8
100	1.47	1.79	53.7	7.3
500	1.64	2.43	49.7	0.5
1000	1.67	2.64	48.6	2.8

**Table 3.7. Calculated  $E$  with “measured”  $A$ , for different  $\nu$ , with  $\rho = 150 \text{ nm}$**

## CHAPTER 4: AN ANALYSIS OF NANOINDENTATION IN SOFT MATERIALS

### ABSTRACT

The effects of cantilever stiffness, preload, and surface interaction forces on the load-displacement relation for soft materials are critically examined in this study. During the indentation of soft materials with an Atomic Force Microscope (AFM), these effects are usually coupled and are observed to influence the deflection-approach displacement measurements. These effects have a particularly significant influence on the accurate extraction of material properties in soft materials. To understand these effects, three separate experiments were performed, (i) the indentation with a 'rigid cantilever' on a soft material with no surface forces, (ii) the indentation with a compliant cantilever on a rigid material with surface forces and, (iii) the indentation with a compliant cantilever on a soft material with surface forces. For the first experiment, it is observed that the effects of preload resemble a shift of the measured nanoindentation load-displacement curve to the right of the tip-specimen contact point. The second experiment examines the influence of the cantilever stiffness on the surface forces measured by the deflection-approach displacement records of the AFM. The third experiment most closely resembles practical nanoindentation of soft materials. In this experiment, all the three effects were present and coupled. A novel technique to account for these effects is proposed, in order to accurately extract the material properties of interest.

## 4.1. INTRODUCTION

In recent years, the importance for the mechanical characterization of biological materials has become evident in the field of biology, ranging from the diagnosis of diseases (Paszek et al., 2005; Suresh et al., 2005) to the understanding of cell-biology (Ingber et al., 1994; Lo et al., 2000; Wang et al., 2003; Wells, 2008). Biological materials are commonly soft and viscoelastic in nature and characterized by means of traditional techniques such as the uniaxial test. For small area and volume specimens such as thin protein films, tissues, cells, etc., or when local mechanical properties are of interest, nanoindentation is commonly used to extract their stiffness values. Since the indentation force required in these indentations is usually small, they are commonly performed using the atomic force microscope (AFM) because of its superior force resolution compared to a typical force resolution of approximately 100 *nN* of a nanoindenter. Unlike a nanoindenter, the AFM does not require a load cell to measure the indentation load. Instead, the AFM derives the indentation force by multiplying the measured deflection of the cantilever with its spring constant. Thus, with the selection of an appropriate soft cantilever, the AFM is able to measure low indentation force down to the 1 *pN* range, which makes it particularly suitable for soft materials.

Soft materials such as rubber and gel are commonly incompressible and exhibit elastic deformations which satisfy the prerequisite for the accurate application of the stiffness equation. Moreover, since deep indentations are usually achieved during the nanoindentation of soft materials, it was concluded in Chapter 2 that the finite tip radius effect is not significant. These unique mechanical characteristics all seem to suggest that

the conventional method to extract material properties using nanoindentation is very appropriate for soft materials, which will be investigated in this study.

Many soft materials are non-linearly elastic, viscoelastic, and hysteretic (Mullin's effect), which will undoubtedly affect the applicability of the stiffness equation in the indentation on such materials. However, such effects are not considered in this study. The materials chosen for this study (latex and polyacrylamide gel) are rate-insensitive and linearly elastic, as evidenced by their uniaxial stress-strain curves. Nevertheless, even when such soft linearly elastic materials are used, there are still challenges impeding the accurate extraction of material properties using the stiffness equation. Surface interaction forces between the tip and the specimen are particularly significant in the indentation of soft materials, which were not considered in the theoretical derivation of the stiffness equation. The effect of preload in the indentation of soft materials was identified in Chapter 2 to be crucial for the accurate extract of material properties as well. Moreover, the use of the AFM introduced an additional variable, the stiffness of the cantilever, which can influence the measurements during the nanoindentation experiment.

This chapter will be organized as follows. The study will first discuss the effects of the stiffness of cantilever tip, the tip-specimen contact point and the surface forces in Section 4.2. The interaction between these effects and their influences on the overall accuracy of the extracted material properties will be investigated in detail in the experiments presented in Section 4.3. This study explores three indentation scenarios, (i) the indentation with a 'rigid cantilever' on a soft material with negligible surface forces, (ii) the indentation with a compliant cantilever on a rigid material with surface forces and finally, (iii) the indentation with a compliant cantilever on a soft material with surface

forces. The first two experiments isolate some of these effects for a closer examination while the third experiment most closely resembles a typical practical nanoindentation of soft materials, where all the effects are present and coupled. Techniques to account for the effects are presented in their respective sections for each indentation scenario. Finally, summary and conclusions for this study will be presented in Section 4.4.

## 4.2. ACCURACY OF THE EXTRACTED MATERIAL PROPERTIES

Nanoindentation of soft materials using the AFM poses a different set of challenges than the ones already discussed in the previous chapters. As illustrated in Fig. 4.1, nanoindentation using the AFM is a ‘displacement controlled’ experiment, where the user imposes an approach displacement,  $\delta$ , between the tip and specimen that usually follows a ramp function. This approach is actuated by piezoelectric transducers located either at the indenter head or at the stage and is monitored throughout the indentation.

Another parameter monitored during the experiment is the deflection by the cantilever,  $\delta - h$ , where  $h$  is the indentation depth. A laser beam is reflected off the tip of the cantilever, thus any changes to the slope at this location will be detected by the photo-detector monitoring the reflected laser beam. The conversion factor between the changes in the slope of the cantilever to changes in the deflection of the cantilever generally depends on the geometry of the cantilever. It is usually calibrated through an indentation on a ‘rigid surface’ (a specimen that is as stiff as the indenter tip but much stiffer than the spring constant of the cantilever). In this case, the deflection will equal the approach distance and thus the slope-to-deflection factor for the cantilever can be calculated.

The stiffness or spring constant of the cantilever is commonly derived through the measured intensity of the thermal noise during the excitation of the cantilever with thermal fluctuations (Hutter and Bechhoefer, 1993). The indentation force is then inferred by the product of the spring constant of the cantilever and its deflection. The stiffness of the cantilever affects the force resolution of the indentation, the penetration depth of the tip, the amount of preload on the specimen and the effects of surface forces on the

indentation load-displacement curve. Each of these effects will be discussed individually in the subsequent subsections. In this study, the indenter tips (made of glass or diamond) are much stiffer than the soft specimens tested, and thus are assumed to be rigid; the specimens, on the other hand, are sufficiently large to meet the converged geometry criteria established in Chapter 2.

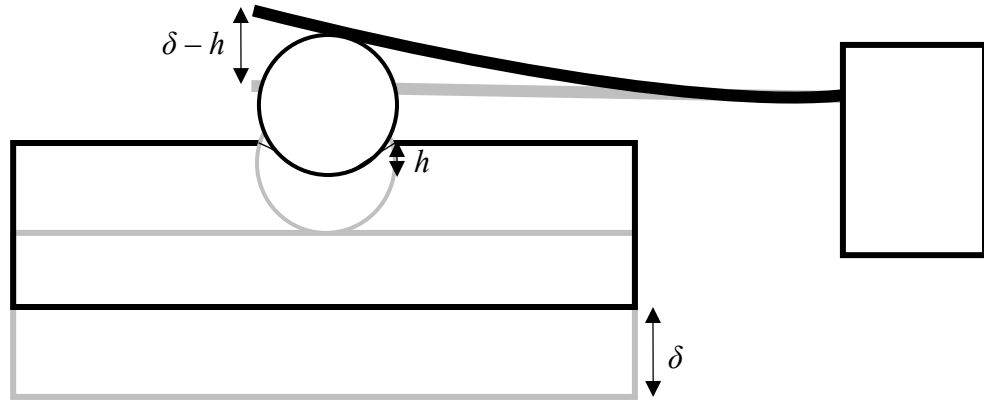


Fig. 4.1. Illustration of indentation with the AFM

#### 4.2.1. Stiffness of the Cantilever

The indentation problem between a rigid spherical indenter and a linearly elastic half-plane was first studied by Hertz (1881). The total indentation force,  $P$  is given by

$$P = \frac{4 a^3 E}{3 R (1 - \nu^2)} = k_c (\delta - h) \quad (1)$$

where  $a$  is the radius of the contact area,  $R$  is the radius of the spherical indenter,  $E$  and  $\nu$  are the Young's modulus and Poisson's ratio of the specimen, and  $k_c$  is the spring constant of the cantilever. At equilibrium, the indentation force on the specimen must equal the restoration force,  $k_c (\delta - h)$  of the cantilever, acting in the opposite direction to the deflection of the cantilever. The indentation depth,  $h$  is given by

$$h = \frac{a^2}{R} . \quad (2)$$

Eqs. (1) and (2) can be solved simultaneously to obtain an expressions with: (i) indentation load,  $P$ , as a function of imposed approach displacement,  $\delta$ , (ii) cantilever deflection ( $\delta - h$ ) as a function of the imposed approach displacement,  $\delta$ , and (iii) indentation force,  $P$ , as a function of indentation depth,  $h$ .

Figures 4.2, 4.3 and 4.4 show the effects of the stiffness of the cantilever on  $P$ ,  $\delta - h$ ,  $\delta$ , and  $h$ . In these plots, the material constants  $E$  and  $\nu$  were arbitrarily chosen to be 100  $kPa$  and 0.5, respectively, which are within the typical range of values for many soft biological materials. The stiffness of the cantilever for the AFM is typically between 0.05  $N/m$  and 0.5  $N/m$ , however a larger range of stiffness (between 0.0001  $N/m$  and 1  $N/m$ ) was used in these plots to better illustrate the effect of varying cantilever stiffness. The radius of curvature of the spherical indenter was arbitrarily selected to be 2.5  $\mu m$  for this example. The imposed approach distance,  $\delta$ , a parameter usually assigned by the user during an indentation, was arbitrarily chosen to be 2  $\mu m$  for all the indentations.

Figure 4.2 shows  $P$  vs.  $\delta$  for various  $k_c$ . In this figure, it is observed that softer cantilevers offer better force resolution. The slope of the curves decreases with decreasing cantilever stiffness, thus every unit of  $\delta$ , the softer cantilever measures a smaller unit of  $P$  as compared to a stiffer one. This plot also shows that the amount of force the tip exerts on the specimen depends significantly on the stiffness of the cantilever used.

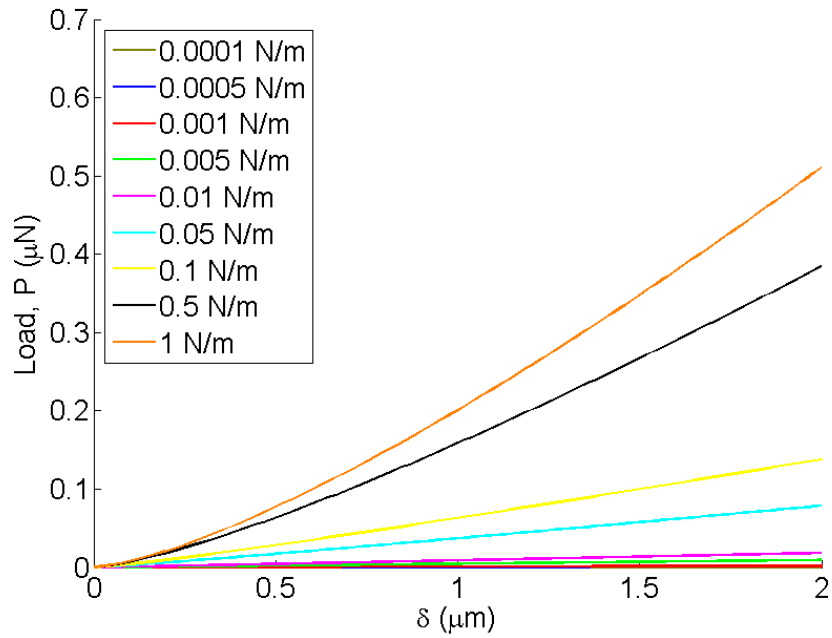


Fig. 4.2. Indentation load,  $P$ , vs. imposed approach distance,  $\delta$ , for different cantilever stiffness,  $k_c$

Figure 4.3 shows  $(\delta - h)$  vs.  $\delta$  for different  $k_c$ . This figure shows that as the cantilevers become softer, the slope of the curves tends towards unity. As observed in Fig. 4.2, the soft cantilevers barely exert any force on the specimen, hence, the imposed approach displacement  $\delta$  is entirely translated to tip deflection  $(\delta - h)$ .

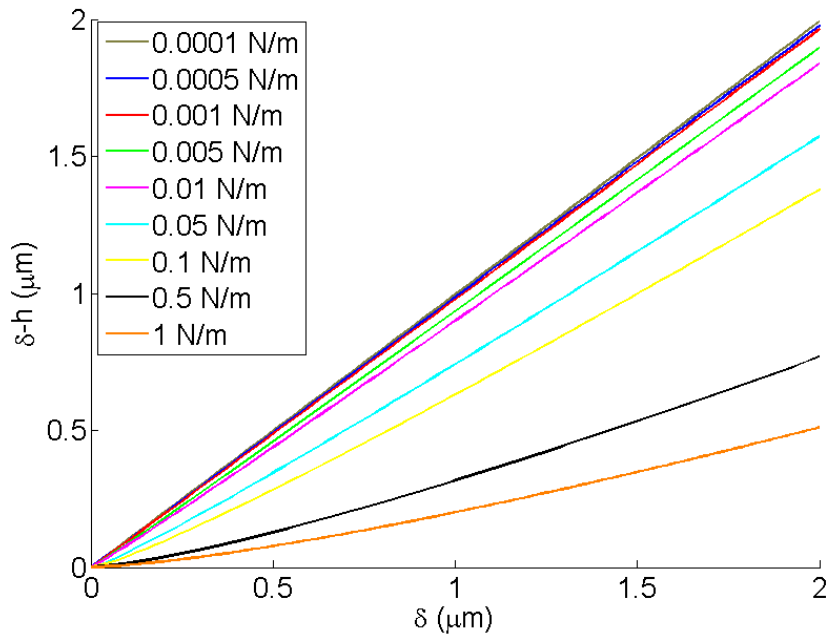


Fig. 4.3. Cantilever deflection vs. imposed approach displacement,  $\delta$ , for different cantilever stiffness,  $k_c$

Figure 4.4 shows  $P$  vs.  $h$  for various  $k_c$ . This figure shows that the indentation depth,  $h$ , is dependent on the cantilever stiffness,  $k_c$ . As concluded by the previous figures, a softer cantilever exerts a smaller indentation load on the specimen, hence reaching a shallower penetration depth. Therefore, it is evident that nanoindentation using the AFM is not exactly a ‘displacement controlled’ experiment, since the actual indentation depth is largely dependent on the stiffness of the cantilever used.

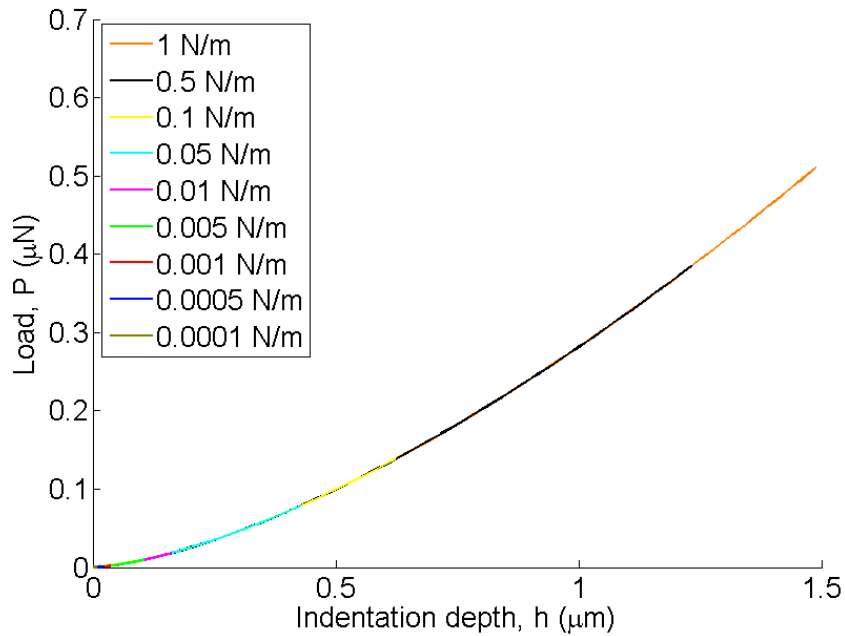


Fig. 4.4. Indentation load,  $P$ , vs. indentation displacement,  $h$ , for different cantilever stiffness,  $k_c$

#### 4.2.2. Tip-Specimen Contact Point

For the indentation of soft materials, the identification of the point of contact between the tip and specimen, without any penetration into the specimen, is generally non-trivial. Firstly, in order for the nanoindenter or AFM to detect any contact, a finite amount of force (for the load cell in the nanoindenter) or a finite deflection of the cantilever is usually required. This value can be minimized through careful calibration *but will always remain finite*. For the indentation of a stiff specimen, this finite force exerted on the specimen normally result in negligible displacement, however, for a soft specimen, this force can results in a large indentation depth by the indenter tip. Without the presence of any surface forces, this preload can usually be inferred from the ‘set point’ — for the nanoindenter, the preset load point that defines contact; for the AFM, the preset deflection by the cantilever that defines contact. It should be noted, however, for

some modern AFM, this effect is eliminated by retracting the tip some distance away from the specimen before the indentation. This preload is crucial for the accurate extraction of material properties, which will be discussed in detail in Section 4.3.1.

The identification of the contact point is further complicated by the presence of surface forces. The different types of surface forces will be discussed in detail in Section 4.2.3. In this section, surface force is treated as an attractive force between the tip and the specimen. As the tip and the specimen come into contact, the attractive force will pull the tip towards the specimen which can result in an indentation for soft materials. Unlike the preload resulting from a finite ‘set point’ to establish contact by the equipment, it is usually more difficult to infer the preload due to surface forces between the tip and specimen. A novel method to extract this value of preload due to surface forces in soft materials will be presented in Section 4.3.3.2.

#### 4.2.3. Surface Forces

The surface force between the tip and specimen can arise from several different sources. The most common considerations include the Van der Waals force, the electrostatic force or the Coulomb force, and the capillary force (Burnham and Colton, 1989; Cappella et al., 1997; Mann and Pethica, 1996; Ouyang et al., 2000; Zammaretti et al., 2000). Unfortunately, it is often difficult to identify the most critical force of all since the effects from each of these forces differ for different tip-specimen configurations (Ouyang et al., 2000). Researchers have explored multiple ways to isolate these forces by examining the tip-specimen contact under various conditions — in air, all the three forces are in play during indentation; in water, the electrostatic and capillary forces are removed,

however, a repulsive double-layer force (due to the charging of both sample and tip surfaces in liquids) may be introduced; under ion showers, the electrostatic force is removed (Cappella et al., 1997; Ouyang et al., 2000).

The effect from surface forces between the tip and the specimen is more significant during the indentation of soft materials. Firstly, this is because the amount of force required to indent softer materials is smaller, thus any other artificial effects from the tip-specimen interactions are significantly amplified; and secondly, the asperities on the soft material tend to conform to the indenting surface, which increases the effective surface area of the contact. This often intensifies the effect of surface forces between the two surfaces.

In this study, the surface forces are treated as a single entity composed of the long-range attractive force and the short-range adhesive force. The long-range attractive force is observed before the snap-in of the cantilever (the sudden deflection by the cantilever as the tip comes into contact with the specimen). The short-range adhesive force is directly observed by the pull-off force required to separate the tip from the specimen. The effect of surface forces observed during nanoindentation will be discussed in detail in Section 4.3.2.

## 4.3. EXPERIMENTS

The effects from cantilever stiffness, preload, and surface forces discussed in the previous sections all affect the accurate extraction of the material properties using nanoindentation. To better understand their individual effects, three indentation experiments were designed to isolate them. The first is the indentation with a ‘rigid cantilever’ on a soft material with negligible surface forces to isolate any effects from cantilever stiffness and surface forces. This experiment examines the effects of preload (identification of the zero penetration depth contact point) on the accurate determination of material properties. The second experiment is the indentation with a compliant cantilever on a rigid material with surface forces to study the effects of the cantilever stiffness and the surface forces, and the interaction between them. The third experiment is the indentation with a compliant cantilever on a soft material with surface forces. This experiment most closely resembles practical indentations on soft biological materials to extract material properties. The objective of this experiment will be to develop a method to account for the effects from surfaces forces and preload conditions, so as to be able to extract the material properties accurately.

### 4.3.1. Indentation with a ‘Rigid Cantilever’ on a Soft Material with negligible Surface Forces

Indentation with an AFM cannot be performed using a rigid cantilever. The rigid cantilever will not deflect during the indentation. While  $h$  will be equal to the prescribed  $\delta$ , the measurement for  $P$  is not possible. Hence, to isolate the effects from the cantilever

stiffness, a nanoindenter was used for this experiment. During the indentation, the indenter tip was moved towards the specimen with piezoelectric transducers, while the specimen sits on a stationary stage. The indentation load,  $P$  was measured using a load cell. The nanoindenter is unable to achieve the force resolution of the AFM but it eliminates any complications arising from the cantilever stiffness.

In this experiment, natural latex rubber was used. The latex rubber was first tested uniaxially using the servo-hydraulic Materials Testing System (MTS 358 series) with 30-*kip* (13.3 *kN*) load cartridge. The measured compressive uniaxial stress-strain behavior of latex is shown in Fig. 4.5. The cubic specimens (12 *mm* on each side) were loaded repeatedly at various strain rates without significant changes to the measured stress-strain behavior. It is observed that latex is essentially linearly elastic up to 10% strain.

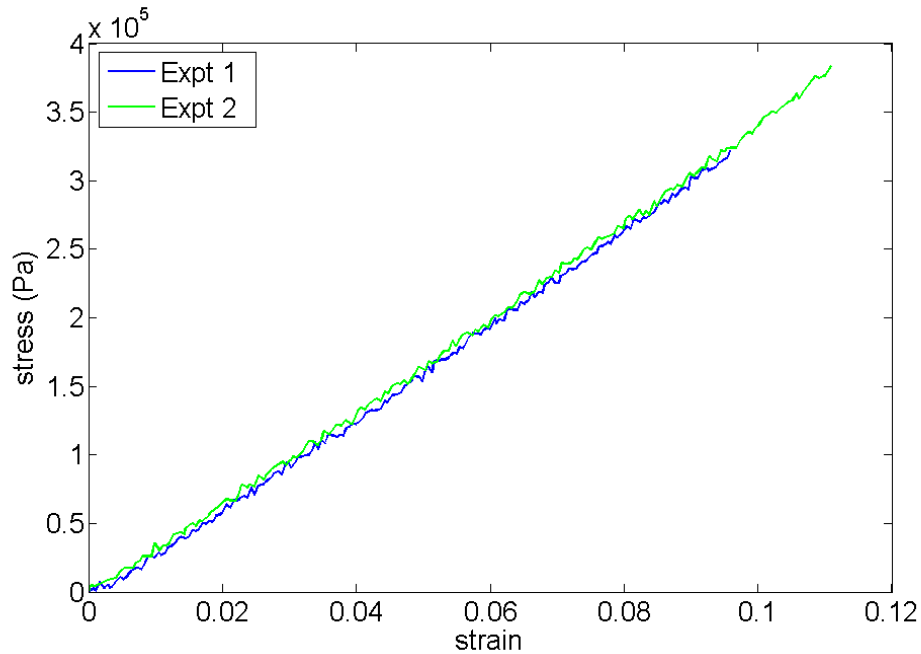


Fig. 4.5. Uniaxial true stress-strain curves for natural latex rubber

The nanoindentation experiment was then performed on the latex rubber using a diamond Berkovich tip on the Hysitron™ Triboindenter. The loading function was

created with the open loop load-control option. The contact ‘set-point’,  $P_o$  (the load threshold to establish contact) was set at the default of  $2 \mu N$ . The indentation sites were scanned after each indentation and showed no residual imprints. A typical load-displacement curve measured during the experiments is shown in Fig. 4.6. Unlike the uniaxial response, hysteresis was observed in the load-displacement measurements suggesting the attainment of larger strains. To a first approximation, the average behavior of the material is considered as shown in Fig. 4.6.

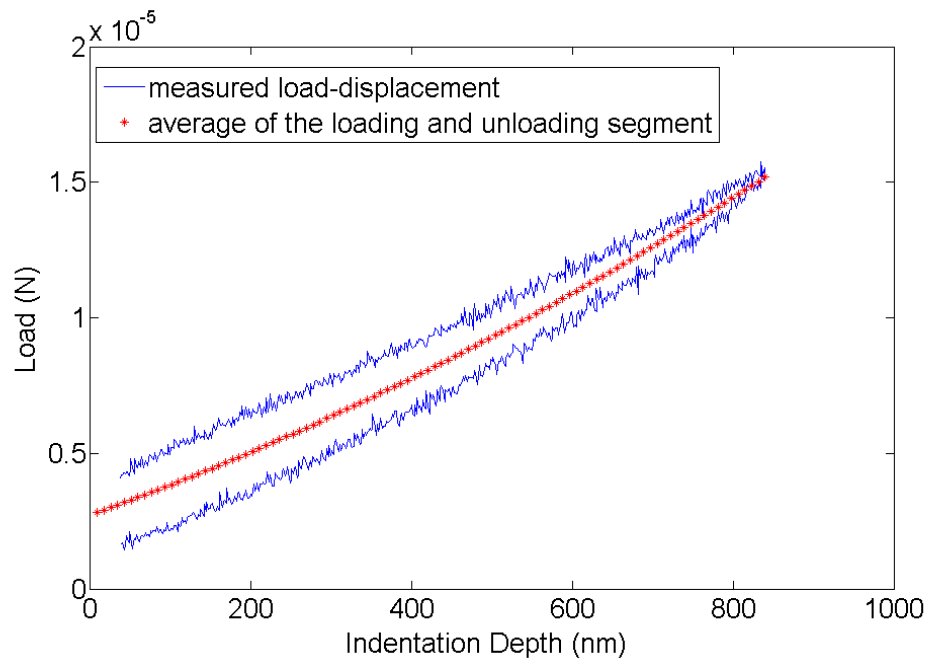


Fig. 4.6. Typical measured load-displacement nanoindentation curve for latex rubber using a Berkovich tip

The averages of the loading and unloading segments of several nanoindentations of natural latex are plotted in Fig 4.7. The Young’s modulus,  $E$ , of the latex was determined to be  $3.46 \text{ MPa}$  from uniaxial experiments in Fig. 4.5, and its Poisson’s ratio,  $\nu$ , was assumed to be 0.5. Using the values of  $P_o$ ,  $E$ , and  $\nu$ , a theoretical load-displacement curve is derived using Sneddon’s equation (1948) for a conical tip with a half-angle of  $70.3^\circ$  — the equivalent of the actual pyramidal indenter (in this case a

Berkovich tip) to a conical tip with the same projected area-to-depth relationship is widely accepted by the research community (Fischer-Cripps, 2004; Lichinchi et al., 1998; Oliver and Pharr, 1992; Wang et al., 2006; Yu et al., 2004). From Fig. 4.7, the experimental load-displacement curves were observed to match the theoretical load-displacement curve well.

During the indentation of stiffer materials such as aluminum, fused quartz, and metallic glass in Chapter 3, the same preload of  $2 \mu N$  results in negligible indentation into material as such  $h$  equals zero is taken to coincide with the location where the tip just touches the specimen without any penetration. This is evidently not the case for the indentation of soft materials as shown in Fig. 4.7. The location in which the tip just touches the specimen without any penetration is at the negative  $500 \text{ nm}$  mark. The approximately  $2 \mu N$  of load required for the load-cell to establish contact resulted in about  $500 \text{ nm}$  of indentation depth in the specimen. Considering that the typical range for nanoindentation depth is between  $200 \text{ nm}$  to  $1 \mu m$ , this preload displacement,  $h_o$  of  $500 \text{ nm}$  is very significant.

For an indentation with a conical tip, the preload,  $P_o$ , effectively shifts the measured load-displacement curve to the right of tip-specimen contact point by  $h_o$ , as follows

$$(P - P_o) = \frac{2 E \tan \alpha}{\pi (1 - \nu^2)} (h - h_o)^2 \quad (3)$$

where  $\alpha$  is the half angle of the conical indenter. As discussed in the earlier chapters, the slope of the load-displacement curve is commonly used by the stiffness equation to extract the elastic properties of the material of interest. The slope of the load-displacement curve for the preloaded specimen is given by

$$\frac{dP}{dh} = \frac{4 E \tan \alpha}{\pi (1 - \nu^2)} (h - h_o). \quad (4)$$

If the effects of the preload are not accounted for from (4), the slope of the load-displacement curve will be overestimated (since  $h_o$  is positive). This error will be propagated to the accuracy of the extracted material properties when the erroneous slope for the load-displacement curve is used in the stiffness equation. This error will lead to an overestimation for the extracted reduced modulus. The green line in Fig. 4.7 illustrates the load-displacement curve if the preload is not taken into account. It is evident that the green line is distinctly steeper than the red one. Similar effects can be demonstrated for other indenter geometries as well.

However, as shown in Fig. 4.7, if  $P_o$  and  $h_o$ , are appropriately accounted for, the linear elastic theory coincides rather well with the experimental results. This ensures that the stiffness equation can be used to accurately extract the reduced modulus of interest through the nanoindentation load-displacement measurements.

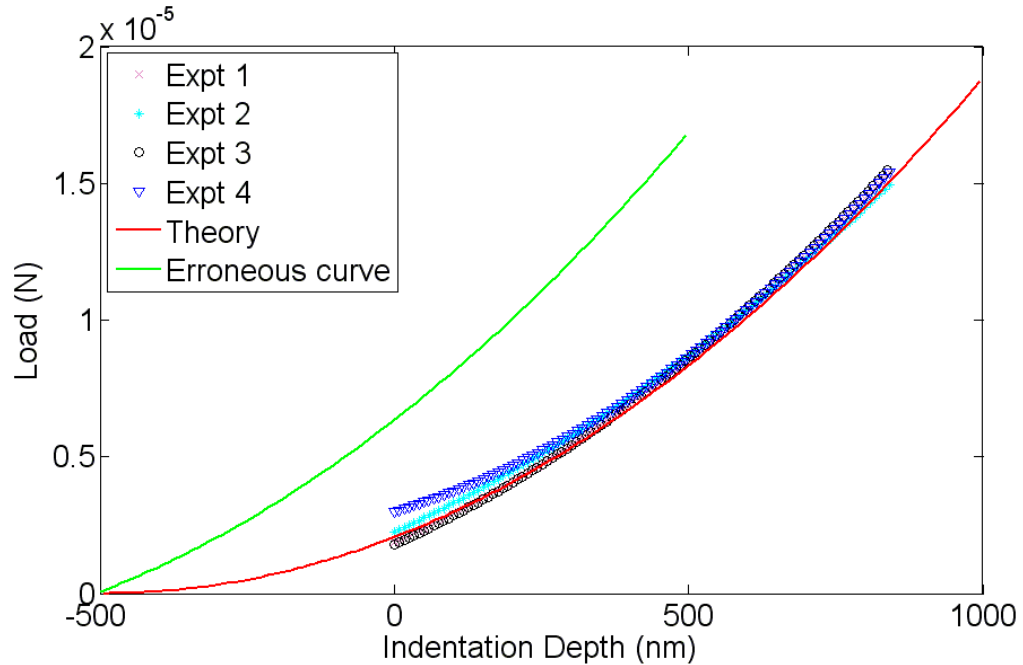


Fig. 4.7. Comparison between experimental and theoretical load-displacement curves for the indentation of latex

#### 4.3.2. Indentation with a Compliant Cantilever on a Rigid Material with Surface Forces

To investigate the effects of cantilever stiffness and surface forces, nanoindentations were performed using the Asylum Research MFP-3D-BIO™ AFM. Two separate cantilevers were used in the experiments with stiffness of  $0.2735 \text{ N/m}$  and  $0.0766 \text{ N/m}$ , respectively. The spring constants for the cantilevers were calibrated automatically using the thermal calibration option (Hutter and Bechhoefer, 1993). Both cantilevers have a glass spherical tip with a radius of  $2.5 \mu\text{m}$ . In this series of experiments, glass slides were being ‘indented’. Since glass is much stiffer than the cantilevers, it is assumed to behave effectively as a ‘rigid’ material.

Figure 4.8 shows the relationship between the cantilever’s deflection ( $\delta - h$ ), and the imposed approach displacement,  $\delta$ . The slopes of the curves from both cantilevers

were approximately one, which suggests that all of the imposed approach displacements were translated into cantilever deflection. Hence, there can be no indentation into the specimen, which confirms that the glass was indeed a ‘rigid’ material.

The contact point (where the tip initially touches the specimen without any indentation) can be easily identified in these indentations. Since there was no indentation into the glass slide, there can be no preload and the contact point must coincide with the snap-in point (marked by the small dip along the loading path) on the curves.

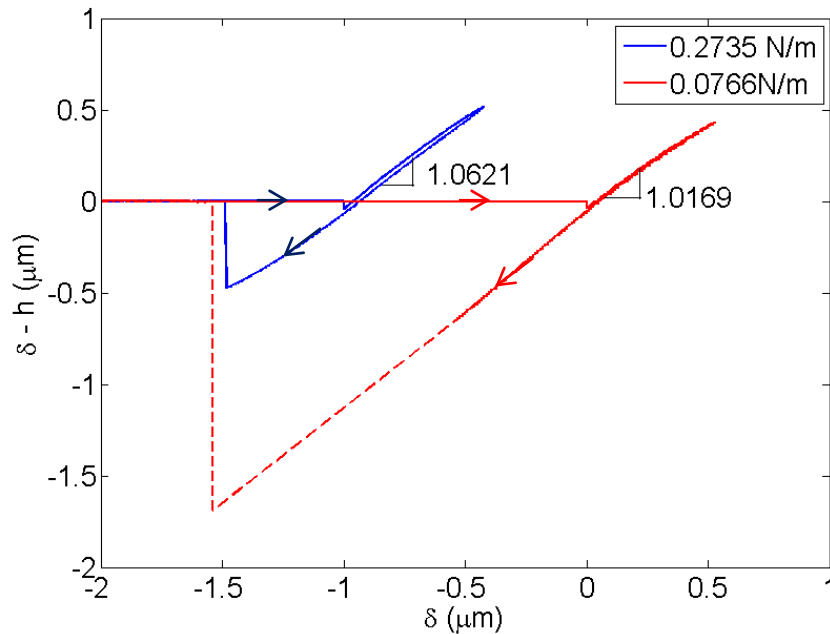


Fig. 4.8. Deflection vs. imposed approach displacement for different cantilever stiffnesses. (Curves are deliberately offset for clarity.)

From Fig. 4.8, it is observed that the loading and unloading deflection-approach displacement curves do not follow the same paths. This hysteresis has been studied extensively by researchers (Burnham et al., 1991; Butt et al., 2005; Cappella et al., 1997) and was best discussed by Cappella et al. as shown in Fig. 4.9. Figure 4.9(a) shows the tip-specimen interaction force vs. the distance between them. This interaction force was

modeled using an inter-atomic Lennard-Jones force for simplicity. The tip-specimen interaction achieves force equilibrium when the force on the specimen equals that exerted by the cantilever. The force by the cantilever is dependent on its stiffness, as shown by both lines marked 1 and 2 in Fig. 4.9(a). The loading process can be described by the shift of the cantilever force curve from right to left. Force equilibrium is achieved whenever the cantilever force curve intersects the tip-specimen interaction force curve. From Fig. 4.9, it is observed that the indentation is stable until the distance between the tip and the specimen reaches point 'a'. It is observed that the force curve at line 1 intersects the tip-specimen interaction force curve at both point 'a' and 'b', thus upon arriving at point 'a', the tip jumps instantaneously to point 'b', resulting in the snap-in phenomenon observed in the corresponding force-approach displacement plot in Fig. 4.9(b). This phenomenon occurs as soon as the gradient of the attractive force exceeds the spring constant of the cantilever (Burnham et al., 1991) as observed in Fig. 4.9(a). Beyond point 'b', the indentation remains stable until it arrives at point 'c' during retraction. Upon arriving at point 'c', the tip jumps to point 'd', resulting in a pull-force of  $f_c$  observed in Fig. 4.9(b). This explains the hysteresis in the deflection-approach displacement observed in Fig. 4.8.

From Fig. 4.9(a), it is observed that the size of the hysteresis depends on the stiffness of the cantilever used. If a sufficiently stiff cantilever is used, there will be no hysteresis between the approach and retraction paths. This is evidently true in Fig. 4.8, as the hysteresis loop measured using the stiffer cantilever is smaller than that measured with the softer one.

While Cappella et al. considered a single force function in Fig. 4.9, different forces could be in play during the approach and retraction stages of the actual indentation test. During the approach, long-range attractive forces such as Van der Waals and electrostatic forces are likely to pull the cantilever tip towards the specimen, eventually causing the snap-in. However, once the tip and specimen come into contact, shorter-range forces, such as capillary forces, take over. Capillary forces are likely to be more dominant during nanoindentation in air due to the moisture accumulated on the surfaces (Cappella et al., 1997), thus requiring a much larger force to separate the tip from the specimen after contact. This hypothesis forms the basis for the decomposition of the surface forces into long- and short-range forces in the subsequent discussions.

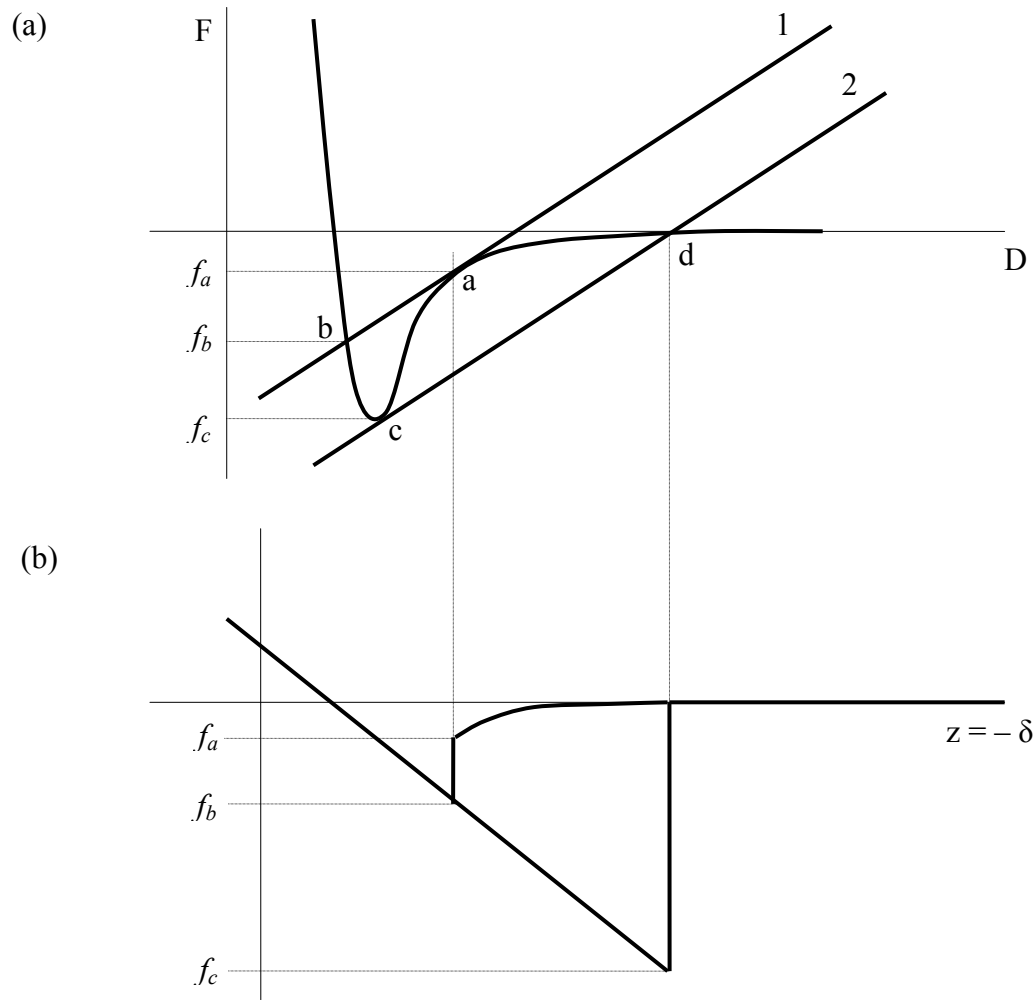


Fig. 4.9. Graphical construction of an AFM force-displacement curve on a rigid specimen with surface forces (after Capella et al. (1997))

Figure 4.10 shows the indentation force vs. the approach displacement. The indentation force,  $P$ , is calculated by multiplying the cantilever deflections with their respective spring constants. The AFM was unable to record the pull-off force during the indentation with the softer cantilever because its deflection went out of the range of measurement. Thus, the final portion of the curves for the soft cantilever in Figs. 4.8 and 4.9 were constructed (dashed lines) assuming that the pull-off force for the soft cantilever equals that of the stiff cantilever. Even though both the cantilevers have identical tips (in

both material and geometry), the pull-off force measured from the two cantilevers may not be the same, as researchers have shown that it is highly dependent on surface roughness of both the tip and the specimen (Ando and Ino, 1996; Hodges et al., 2002; Jang et al., 2007). The surface quality of the two tips was not examined during the experiments. However, for the purpose of comparison in this study, an equivalent pull-off force was assumed.

The adhesion between two rigid bodies was first studied by Bradley (1932). The attractive force,  $F_{ad}$ , between two rigid spheres, is found by integrating a  $\lambda/x^n$  force law between two molecules, given by (Maugis, 1991),

$$F_{ad} = 4\pi\gamma \frac{R_1 + R_2}{R_1 R_2} \quad (5)$$

where  $\gamma$  is the surface energy per unit area of each surface and  $R_1$  and  $R_2$  are the radius of the two spheres, respectively. This expression can be applied to calculate the attractive force between a sphere and a plane by limiting one of the radii to infinity, and to arrive at

$$F_{ad} = 4\pi\gamma R \quad (6)$$

where  $R$  is the radius of the sphere. This expression is subsequently derived by Derjaguin (1934) using geometrical considerations, which was subsequently used in the famous Derjaguin-Muller-Toporov (DMT) model (Derjaguin et al., 1975). The pull-off force measured by the stiff cantilever was approximately 130 nN. Thus from (6), the surface energy per unit area for glass,  $\gamma_{glass}$ , in air was approximately 4.14e-3 N/m.

From Fig. 4.9, it can be observed again that the hysteresis loop from the stiff cantilever is smaller than that from the softer one. This observation agrees with the work of Cappella et al. (1997) as shown in Fig. 4.9.

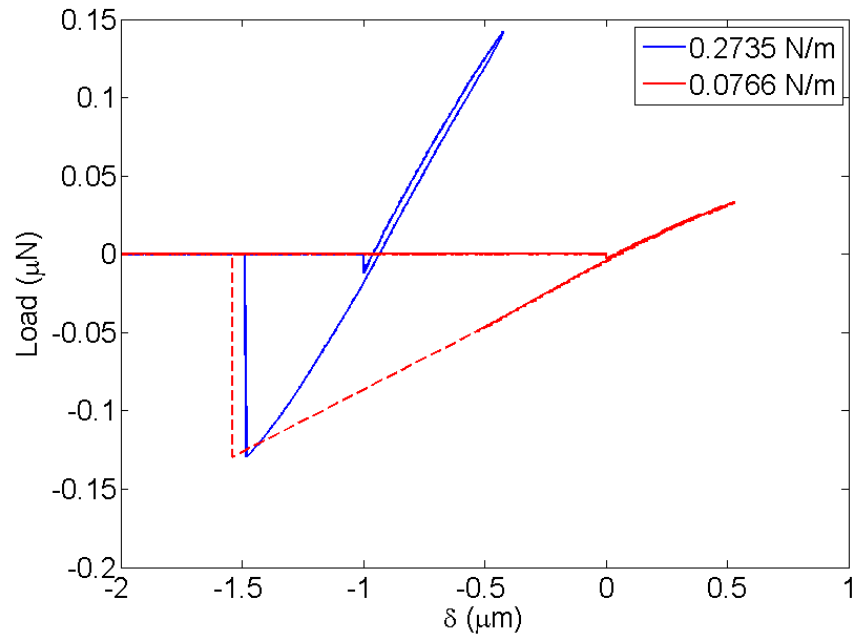


Fig. 4.10. Indentation force vs. imposed approach displacement for different cantilever stiffnesses. (Curves are deliberately offset for clarity.)

#### 4.3.3. Indentation with a Compliant Cantilever on a Soft Material with Surface Forces

The effects of cantilever stiffness, preload, and surface forces were decoupled and studied in detail in the previous experiments. In this experiment however, all three effects will be coupled and the objective is to develop a method to account for these effects so as to accurately extract the reduced modulus for the soft material.

Uniaxial compression experiments were first performed to determine the Young's modulus of the specimen. These experiments were carried out using an Instron single column uniaxial testing machine (5540 series) with a 5 N load cell. The nanoindentation experiments, on the other hand, were performed with the Asylum Research MFP-3D-BIO™ AFM. Two separate cantilevers were used in the experiments with stiffness of 0.2735 N/m and 0.0766 N/m, respectively. The cantilever stiffness was calibrated

automatically using the thermal calibration option (Hutter and Bechhoefer, 1993). Both cantilevers had a glass spherical tip with a radius of  $2.5 \mu\text{m}$ .

A 12% polyacrylamide gel was tested in these experiments. This gel is soft and is hydrophilic in nature. It is commonly used in commercial biological applications such as in the manufacturing of contact lenses and as subdermal filler for aesthetic facial surgeries. The polyacrylamide gel was cast simultaneously in a Petri dish (thickness of approximately  $10 \text{ mm}$ ) and in between two glass plates in a vertical GE Healthcare gel caster (thickness of approximately  $3 \text{ mm}$ ). The gel in the Petri dish was carved into cylinders using a cylindrical coring tool (works like a cookie cutter). The diameter-to-thickness ratio of these cylinders was approximately one. These specimens were used in the uniaxial tests. The gel film in the gel caster, on the other hand, was used for the nanoindentation experiments. Cast between two glass slides, this gel film had a smooth surface for indentation which is an important consideration in nanoindentation experiments. The specimens for the uniaxial compression tests, on the contrary, are less sensitive to the surface roughness than the aspect ratio of its geometry. The asperities on the surfaces were likely to flatten out upon contact since the size of the asperities was much smaller than the surface area of contact. The diameter-to-thickness ratio of the geometry on the other hand, is a crucial parameter because a small ratio might cause the specimen to buckle under the slightest misalignment while a large ratio will not only reduce the resolution of strain measurement but also enhance any frictional effects along the loading surfaces.

Figure 4.11 shows the true stress-strain curves for three different cylindrical polyacrylamide gel specimens carved from different locations on the Petri dish. The

specimens were loaded repeatedly at different strain rates without any significant changes in the stress-strain behavior. The first observation is that polyacrylamide gel is practically linearly elastic up to 20% strain. However, the Young's modulus,  $E$ , of the gel is not homogeneous across the Petri dish in which it was cast. The largest  $E$  measured for the gel was approximately 153  $kPa$  (blue line) and the smallest measured was approximately 137  $kPa$  (green line). Taking the average of all the specimens tested,  $E$  for polyacrylamide gel is approximately 144  $kPa$ . To ensure that the time lag between the uniaxial experiment and nanoindentation experiment ( $< 5$  hours) did not affect the overall mechanical properties of the polyacrylamide gel, the cylindrical specimens were retested after 24 hours and their stress-strain curves yielded no significant differences.

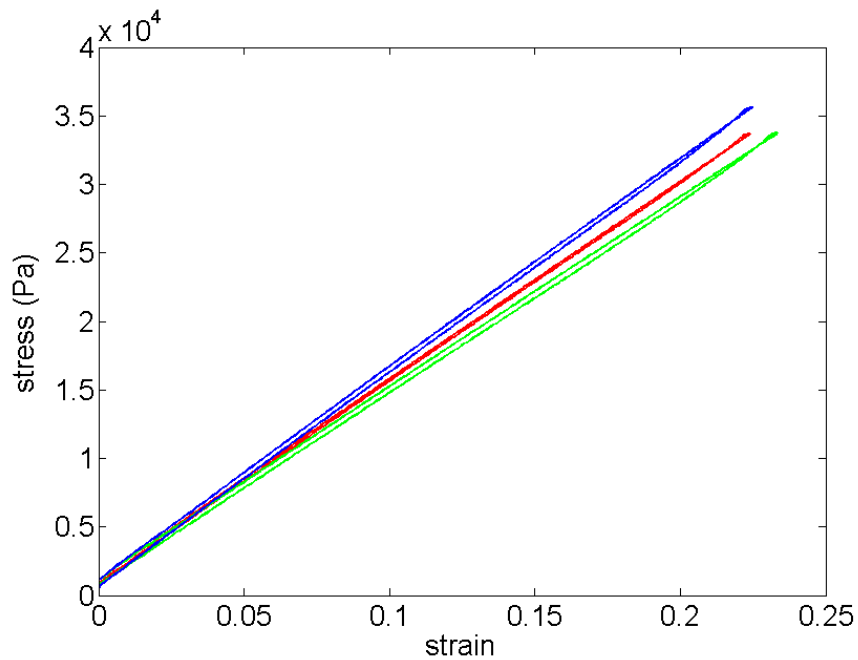


Fig. 4.11. True stress-strain curves for polyacrylamide gel specimens cut from various locations of the Petri dish under uniaxial compression

Figure 4.12 shows the indentation load-displacement curves for the two cantilevers used. Using  $E$ ,  $\nu$ , and  $R$  of 144  $kPa$ , 0.5, and 2.5  $\mu m$ , Hertz's solution, shown

in (1), was plotted for comparison. The Hertz curve, shown by the green line in Fig. 4.12, is plotted with the assumption that there is no preload ( $h$  equals zero corresponds to the contact point), which is unlikely the case, as discussed earlier. Snap in for both the soft and stiff cantilevers is marked by the decrease of  $f_1$  and  $f_2$ , respectively. It is evident that  $f_1 > f_2$ , which agrees with the previous experiment. The snap-in forces  $f_1$  and  $f_2$  measured the amount of force each cantilever was exerting against the attractive surface force to pull the tip away from the specimen. Hence, the amount of preload exerted on the specimen due to the surface forces is inversely related to the snap-in force. If the tip-specimen surface interaction force for both the soft and stiff cantilevers can be assumed to be equivalent, then the amount of preload due to the surface forces was larger when the soft cantilever was used.

From Fig. 4.12, it is evident that the measured load-displacement curves for both the stiff and soft cantilevers are distinctly different from the Hertz prediction. It should be noted that the linear elastic Hertz solution can be algebraically manipulated into the stiffness equation, since the latter was shown to be applicable for all axisymmetric indenters with an infinitely smooth profile (Pharr, et al., 1992). Therefore, the difference between the experimentally measured load-displacement curves and Hertz's linear elastic solution demonstrates that the application of the stiffness equation will inevitably yield inaccurate extracted material properties for this material. The load-displacement curves for each cantilever will be discussed in detail in the subsequent sections.

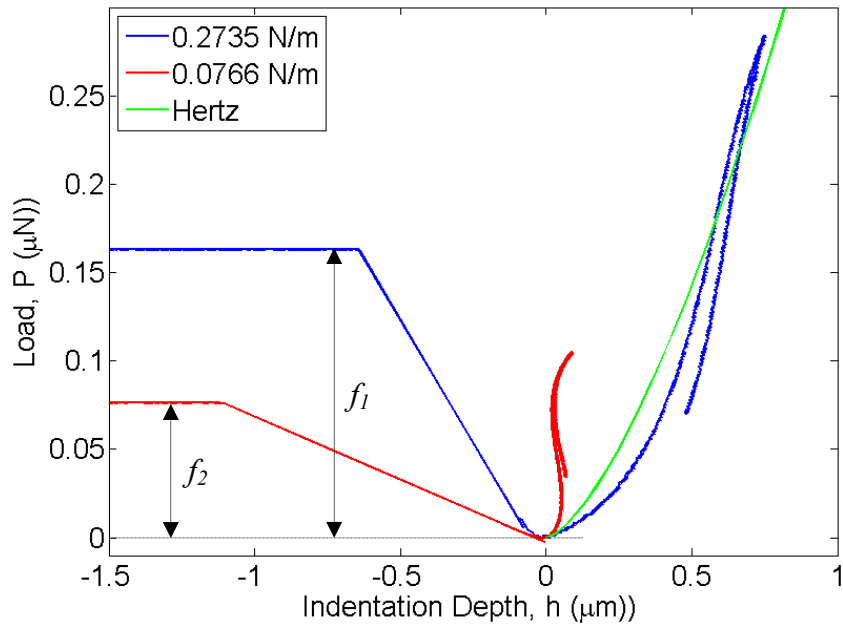


Fig. 4.12. Comparison between indentation load-displacement curves for different cantilever stiffness with Hertz prediction

#### 4.3.3.1. Indentation with the soft cantilever

The load-displacement curve for the soft cantilever resembles an S-shaped curve, which does not exhibit the  $P=f(h^{3/2})$  relationship, shown in (1), predicted by Hertz (1881). To better understand the deformation of the soft cantilever during indentation, a numerical finite element (FE) simulation was performed using commercial FE package ABAQUS.

The actual cantilever beam was made of silicon nitrate. It had a  $200 \mu\text{m}$  long, V-shaped geometry and a spring constant of  $0.0766 \text{ N/m}$ . The virtual cantilever beam in the numerical experiment was modeled as a  $200 \mu\text{m}$  long rectangular beam with a section profile of  $100 \mu\text{m}$  by  $0.455 \mu\text{m}$ , so as to obtain a moment of inertia,  $I$  of  $0.786\text{e-}25 \mu\text{m}^4$ . The material for the beam was modeled as isotropic and had a Young's modulus and Poisson's ratio equivalent to silicon nitride's, which are  $260 \text{ GPa}$  and  $0.24$ , respectively.

The virtual beam was designed to have an identical spring constant of  $0.0766 \text{ N/m}$ . The beam was meshed with 20 2-node linear ‘beam in a plane’ elements (B21). To ensure convergence, the beam was deformed through a series of force and displacement controlled numerical simulations, and the results were found to coincide with known solutions. The number of elements was also doubled with no significant changes to the solutions, suggesting the attainment of convergence. The beam was cantilevered on one end and free on the other, which is identical to the boundary conditions of the actual cantilever. To model the contact problem, the free end of the beam was attached to a non-linear spring, as shown in Fig. 4.13. The spring was infinitely soft (with a spring constant of zero) for the first micron to simulate the snap-in behavior. The concentrated force of  $76 \text{ nN}$  (equals  $f_2$ ) exerted on the tip of the beam, will deflect the virtual beam by approximately  $1 \mu\text{m}$  without any resistance from the attached non-linear spring. Beyond the contraction of this initial distance, the spring will exhibit a Hertz contact load-displacement relationship using  $E$ ,  $\nu$ , and  $R$  of  $144 \text{ kPa}$ ,  $0.5$ , and  $2.5 \mu\text{m}$ , respectively. The stage was moved upwards by approach displacement,  $\delta$ , to simulate the ‘indentation’ process. The tip of the beam was not allowed to move laterally after the snap-in to simulate adhesion between the tip and the specimen.



Fig. 4.13. Schematic of the numerical simulation

Figure 4.14 illustrates the deformed shape of the cantilever at different stages of the indentation. The deformation was magnified fifty times in this illustration. Line 'a' corresponds to the undeformed shape of the cantilever and line 'b' corresponds to the shape of the cantilever at snap-in. Lines c–f describe the shape of the cantilever as the tip 'indents' into the specimen. It can be observed that lines c–f show a buckled cantilever that did not deform like an assumed linear beam. Since the AFM infers the deflection of the cantilever through the slope at the tip, the rotation of the node at the tip of the beam in the simulations was recorded. The slope-to-deflection conversion factor was calibrated during the step when a concentrated force was acting on the tip (to simulate snap-in) with the beam behaving linearly.

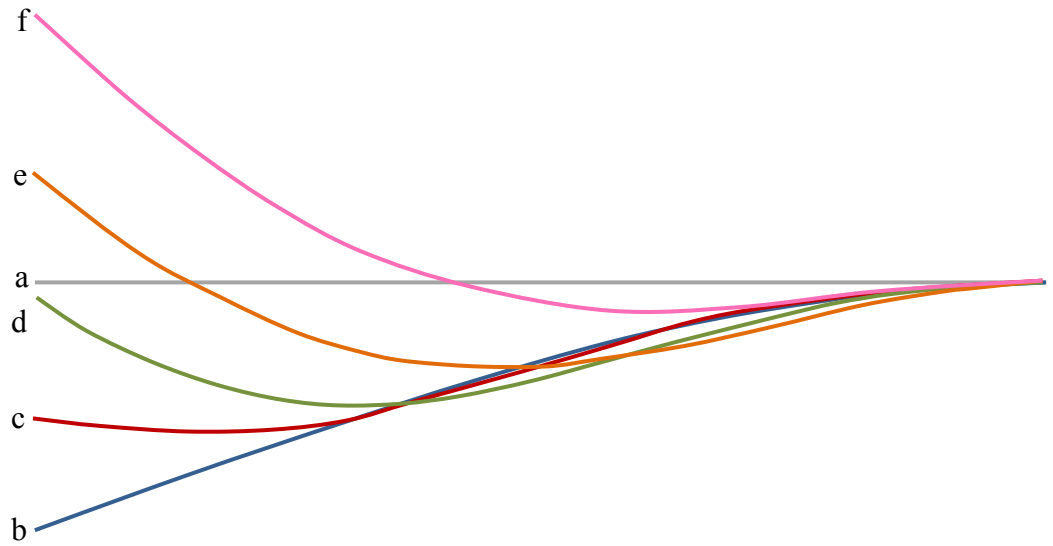


Fig. 4.14. Sketch of the shapes of the deformed cantilever at different stages of indentation.

(The deformation was magnified 50 times.)

Figure 4.15 shows the indentation load-displacement curve obtained from the numerical simulation. The first observation is that the curve captures the general shape of the curve ('S') measured in the experiment shown in Fig. 4.12. This suggests that the soft cantilever was most likely buckled during indentation, which resulted in the erroneous derivation of the indentation load using the slope of the cantilever at the tip. This problem can be eliminated by using stiffer and shorter cantilevers. The indentation depth of the virtual tip, however, is an order of magnitude larger than that measured in the experiment. This is attributed to neglecting the preload in the numerical FE simulation. The numerical experiment considered the snap-in solely as a deflection of the cantilever, without any indentation into the specimen due to the preload from the surface forces. If the preload is considered, the reaction force exerted by the non-linear spring will not start from zero before the 'indentation' process. The reaction force will be equivalent to the preload exerted on the specimen, in order to achieve force equilibrium. Since the non-linear

spring exhibits a monotonically increasing Hertzian contact load-displacement relationship, a smaller indentation depth will be required to achieve a sufficiently large reaction force to buckle the cantilever, if the preload by the surface forces is considered.

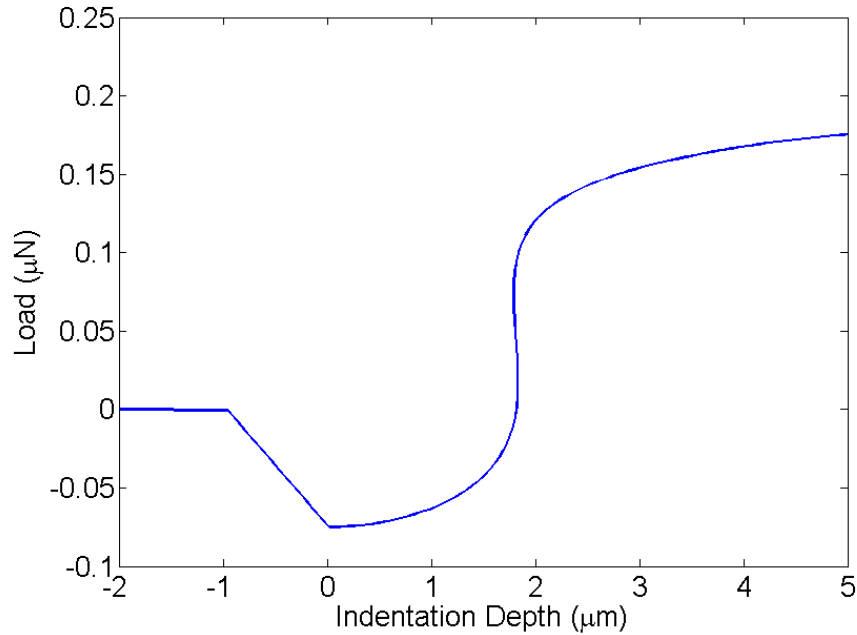


Fig. 4.15. Indentation force vs. indentation depth from numerical simulations

#### 4.3.3.2. Indentation with a stiff cantilever

Unlike the soft cantilever, the indentation load-displacement curve for the stiff cantilever did not exhibit an S-shape behavior, which suggests that the cantilever did not buckle. However, its load-displacement curve is still distinctly different from the Hertz solution. One plausible explanation is that the preload from the attractive surface forces induced indentation upon contact at snap-in. Another reason could be the alteration of the shape of the load-displacement curve due to the attractive surface forces at the tip and specimen, since additional force will now be required to overcome the adhesion between the tip and the specimen. In order to account for the effects from the surface forces,

existing continuum theories describing the effects of adhesion during indentation are carefully reviewed.

The problem of adhesion between two deformable objects had been studied extensively by researchers since the work of Van der Waals (1893). Bradley (1932) and Derjaguin (1934) subsequently derived the attractive force between two rigid bodies. It was 1971 when Johnson, Kendall, and Roberts developed their famous JKR theory which introduced an attractive tip-specimen interaction force into Hertz derivation (Johnson et al., 1971). In 1975, Derjaguin, Muller, and Toporov presented a different theory (DMT theory) for the contact with adhesion problem (Derjaguin et al., 1975). While the JKR theory considers attractive forces within the contact area and takes into account any deformation associated with these forces; the DMT theory considers the attractive forces from the non-contact annulus zone around the area of contact, and assume that these forces do not deform the annulus zone other than Hertz's prediction. After the two contradicting theories were published, researchers began to debate the accuracies of each theory, beginning with the work of Tabor (1977), who compared both theories and highlighted that the DMT theory neglects deformation due to adhesion near the contact area, and that the JKR theory results in a discontinuous displacement around the contact area. This debate continued within the scientific community until Muller et al. (1980) and subsequently Maugis (1991) showed that both theories are the extremes of a theoretical framework they developed. The criteria for the selection of either theory was first proposed by Tabor (1977) and subsequently refined by Muller et al. (1980) — for hard solids with small radii and low surface energies, the DMT theory is more applicable; whereas the JKR theory is more suitable for soft solids with large radii and high surface

energies. Since (i) the spherical indenter tip used in the experiment is large compared to its indentation depth, (ii) the polyacrylamide gel is considerably soft, and (iii) the surface forces were observably strong (possibly due to the hydrophilic nature of the gel), the JKR theory is considered in this study.

The JKR theory considers an additional pressure distribution which also satisfies kinematic constraint for the problem such that (Johnson, 1987)

$$p(r) = p_1(1 - r^2/a^2)^{1/2} + p_2(1 - r^2/a^2)^{-1/2} \quad (7)$$

where  $p_1 = 2aE/\pi R(1-\nu^2)$ ,  $a$  is the radius of contact,  $R$  is the radius of the sphere and  $E$  and  $\nu$ , are the Young's modulus and Poisson's ratio for the specimen respectively. This second term on the right-hand side of (7) was previously omitted by Hertz during his derivation because of the assumption that tensile forces cannot be sustained during indentation. Using a thermodynamic criterion for equilibrium contact,

$$p_2 = -(4\gamma E/\pi a(1 - \nu^2))^{1/2} . \quad (8)$$

The total indentation force,  $P$  found by integrating (5) is

$$P = \left(\frac{2}{3}p_1 + 2p_2\right)\pi a^2 . \quad (9)$$

The total indentation,  $h$  can be derived to be

$$h = \left(\frac{\pi a(1 - \nu^2)}{2E}\right)(p_1 + 2p_2) . \quad (10)$$

The indentation load-displacement curve, which takes adhesive forces into consideration, can be plotted from (9) and (10) if the surface energy per unit area of each surface,  $\gamma$ , is known. This value is usually derived using the pull-off force,  $P_{off}$ , which is given by,

$$P_{off} = -3\pi\gamma R . \quad (11)$$

Unfortunately, in the present experiment on the polyacrylamide gel, the pull-off force is so large that the amount of deflection required by the stiff cantilever to separate the tip and the specimen exceeded the measurable range for the AFM. This problem can be solved experimentally through the use of a stiffer cantilever, but this will reduce the force resolution of the setup, which might be an important consideration for soft materials. To maintain the force resolution of the setup, a stiffer cantilever was not used and  $\gamma$  is treated as an unknown.

The indentations were performed by first manually moving the specimen affixed to the stage slowly towards the tip. The cantilever deflections were monitored throughout the process and when the deflection attained a preset value, the feedback kicked in — the piezoelectric transducers moved a displacement equal to the deflection to ensure no further penetration. The AFM then automatically retracted the tip from the specimen before the nanoindentation experiment was conducted. During the manual approach, as the stage was moved towards the tip, the cantilever was observed to deflect towards the specimen before any contact. This deflection became larger and larger as the distance between the tip and specimen became smaller before the eventual snap-in. This deflection due to long range attractive forces is described by  $f_a$  in Fig. 4.9(b) and was measured manually during the experiment to be approximately 32.8 nN.

Figure 4.16 shows an idealized nanoindentation load-displacement curve for a soft material with surface forces. The snap-in force,  $f_b$ , is composed of the long range attractive force,  $f_a$ , and the short range adhesive force,  $f_b - f_a$ . After snap-in, the adhesive force pulls the tip into the specimen, resulting in a preload displacement of  $h_o$ . The

unloading curve shows a pull-off force,  $P_{off}$  (beyond which the tip separates from the specimen) described by the JKR curve. In this problem, both  $P_{off}$  and  $h_o$  are unknowns.

To solve for  $P_{off}$  and  $h_o$  simultaneously, an error minimization algorithm is used. Since the curvature of the load-displacement curve is unique at each  $h$ , the algorithm minimizes the difference between the experimental curve and JKR curve for all  $P_{off}$  and  $h_o$ . The measure for this difference is the mean of the square of the difference between the load values on the JKR and the experimental curve normalized by the square of the JKR values at each indentation depth. This measure,  $\varepsilon_s$ , is given by

$$\varepsilon_s = \text{mean} \left( \frac{(P_{JKR}(P_{off}, h) - P_{expt}(h_o, h))^2}{P_{JKR}(P_{off}, h)^2} \Big|_{\text{all } h} \right). \quad (12)$$

For each  $P_{off}$ ,  $\varepsilon_s$  was first calculated for all  $h_o$  to determine the optimal  $h_o$  that would minimize  $\varepsilon_s$ . This optimal value for  $h_o$  was then substituted into (12) to determine the optimal  $P_{off}$  that would minimize  $\varepsilon_s$ . The plot for  $\varepsilon_s$  vs.  $P_{off}$  is shown in Fig. 4.17. From this figure, it is observed that  $\varepsilon_s$  was minimized when  $P_{off}$  was approximately -790 nN. The corresponding  $h_o$  that minimizes  $\varepsilon_s$  for  $P_{off}$  at this value was found to be approximately 1.27  $\mu\text{m}$ .

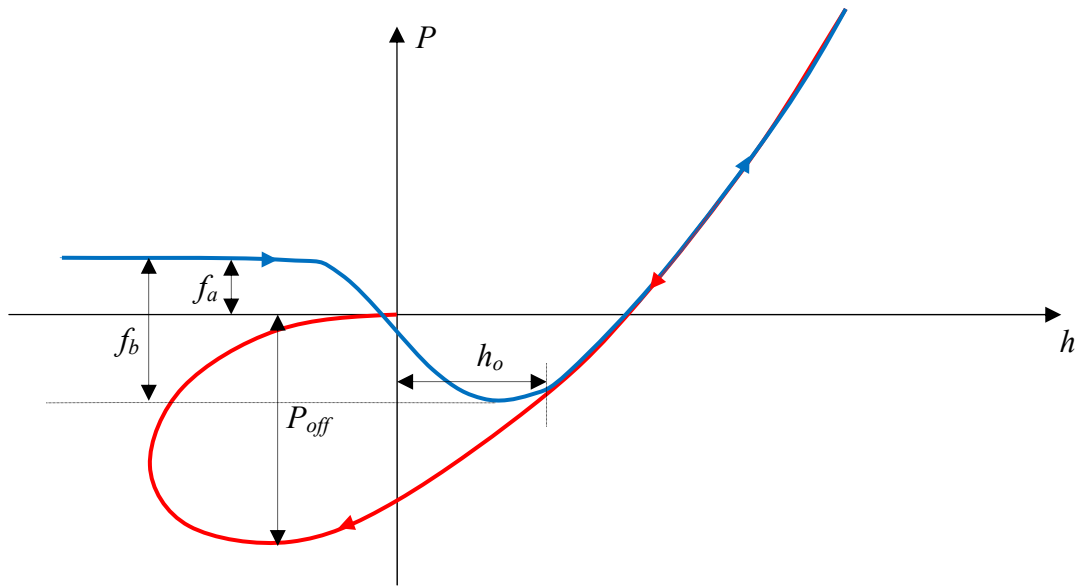


Fig. 4.16. Idealized loading-unloading indentation load-displacement curve for soft material with surface forces

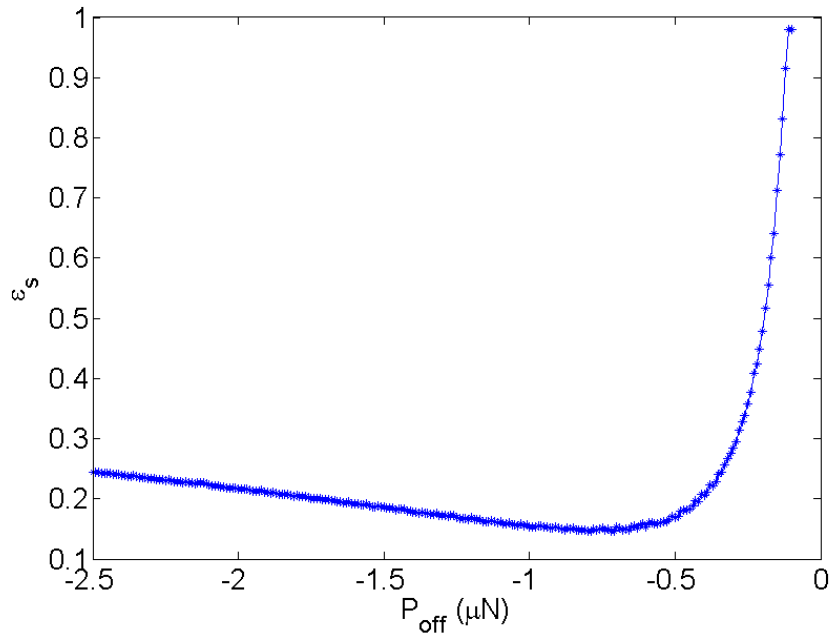


Fig. 4.17. Pull-off force,  $P_{off}$ , vs. percentage square error,  $\epsilon_s$

Figure 4.18 plots the experimental curve in relation to the constructed JKR unloading curve using the  $P_{off}$  and  $h_o$  found to minimize  $\epsilon_s$ . It is evident that the

experimental curve matches the JKR curve better than its previous comparison with Hertz's prediction in Fig. 4.12. While it is true that this minimization scheme requires an *a priori* knowledge of the specimen's reduced modulus,  $E_r = E/(1-\nu^2)$ , a parameter most commonly sought after in indentation experiments, this minimization algorithm provides an alternative to evaluate the surface forces and preload displacement during the indentation of soft materials. Using (11), the surface energy per unit area between glass and polyacrylamide gel,  $\gamma_{gp}$  in air, was found to be approximately  $3.35e-2$  N/m.

The validity of using the JKR model, as opposed to the DMT or transition model can be readily verified. By considering Lennard-Jones potential, Muller et al. (1980) proposed a parameter,  $\mu$ , given by

$$\mu = \frac{32}{3\pi} \left( \frac{8\gamma^2 R (1-\nu^2)}{\pi E^2 Z_o^3} \right)^{1/3} \quad (13)$$

where  $Z_o$  is the typical atomic dimensions. As a rule of thumb, for  $\mu \ll 1$ , the DMT theory is applicable, and for  $\mu \gg 1$ , the JKR theory is more suitable. By considering that the typical atomic dimensions,  $Z_o$ , are of the order of 1 Ångström,  $\mu$  is found to be  $2.16e4$ , which is much larger than one. This confirms that the choice of JKR theory to describe the tip-specimen surface interaction was appropriate.

This technique can also be easily modified for the extraction of the specimen's reduced modulus. In this case, however, the pull-off force has to be measured using a stiffer cantilever. With a known  $P_{off}$ ,  $\varepsilon_s$  can be minimized over  $E_r$  and  $h_o$  (by replacing  $P_{off}$  with  $E_r$  in (12)).

It is important to note that the minimization algorithm is effectively solving an inverse problem where the number of unknowns exceeds the number of constraints. Thus,

it is necessary that a further investigation on the uniqueness of the extracted parameters be conducted following this study.

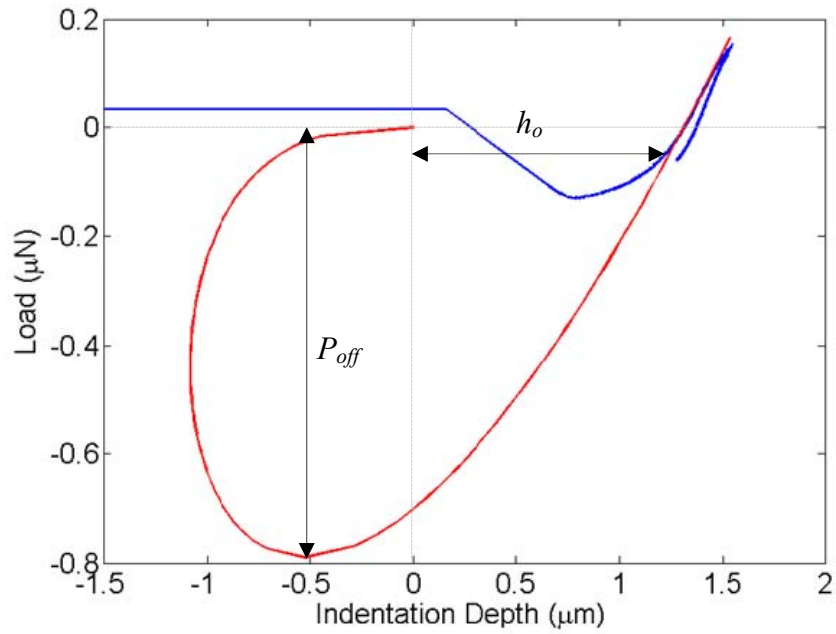


Fig. 4.18. Experimental load-displacement curve plotted in relation to constructed JKR unloading curve with derived  $P_{off}$  and  $h_o$

#### 4.4. SUMMARY AND CONCLUSIONS

This chapter has addressed some of the challenges impeding the accurate extraction of material properties for soft materials using nanoindentation. The effects of the cantilever stiffness, preload, and tip-specimen surface interaction forces were carefully examined. These effects are found to influence each other during the nanoindentation tests. The cantilever stiffness was observed to affect the amount of preload on the specimens and influence the effects of surface forces on the load-displacement measurements. Three indentation scenarios were considered in this study: (i) the indentation with a ‘rigid cantilever’ on a soft material with negligible surface forces, (ii) the indentation with a compliant cantilever on a rigid material with surface forces, and (iii) the indentation with a compliant cantilever on a soft material with surface forces.

The first experiment isolated the effects of preload by examining the nanoindentation of natural latex rubber with a nanoindenter. The Young’s modulus of the natural latex rubber was first measured using a uniaxial compression experiment. The preload was introduced to the nanoindentation experiment due to the finite load set-point required by the nanoindenter to determine contact. This experiment demonstrated that the effects of the preload resemble a shift of the load-displacement curve to the right of the tip-specimen contact point. Neglecting the preload will result in a gross overestimation of the extracted reduced modulus for the specimen.

The second experiment investigated the effects from the cantilever stiffness and the surfaces forces. The nanoindentation experiment was performed using an AFM. A glass slide was indented by glass spherical tips with a radius of  $2.5 \mu\text{m}$ , mounted individually on two separate cantilevers with spring constants  $0.2735 \text{ N/m}$  and  $0.0766$

$N/m$ , respectively. Hysteresis between the loading and unloading curves was observed. This hysteresis was larger for indentations performed using the softer cantilever, which is consistent with the work of Cappella et al. (1997), who demonstrated that the hysteresis can be eliminated with the use of a sufficiently stiff cantilever. However, while Cappella et al. considered a single Lennard-Jones type force function to describe the surface force between the tip and the specimen, it was proposed that different types of surface forces could be at play during the loading and unloading segments of the nanoindentation experiment. During the approach, long-range forces such as Van der Waals and electrostatic forces can cause the unstable snap-in of the cantilever, while short-range forces such as capillary force can be responsible for the larger pull-off force during the retraction of the cantilever.

The third experiment most closely resembles a practical nanoindentation experiment for soft materials where all the effects are present and coupled. In this experiment, 12% polyacrylamide gel was indented by glass spherical tips with a radius of  $2.5 \mu m$ , individually mounted on two different cantilevers (with spring constants  $0.2735 N/m$  and  $0.0766 N/m$ , respectively). The gel was first tested in a uniaxial compression setup to measure its Young's modulus. Both load-displacement curves measured using the soft and stiff cantilever were distinctly different from the linear elastic prediction (Hertz solution), which implied that the stiffness equation cannot be used to accurately extract the material properties of interest.

Using finite element simulations, it was demonstrated that the S-shaped load-displacement curve exhibited by the soft cantilever was the result of buckling. On the other hand, the difference between the load-displacement curve measured by the stiff

cantilever and Hertz's prediction was attributed to the tip-specimen surface forces and the preload. The JKR theory was used to describe the indentation curve with adhesion between the tip and the specimen. However, the JKR theory requires the knowledge of the surface energy, which is commonly derived using the measurable pull-off force. Unfortunately, the pull-off force could not be measured in this experiment as the cantilever's deflection exceeded the measurable limit for the AFM. A stiffer cantilever can be introduced, but it will reduce the load resolution for the nanoindentation experiment. Therefore, an error minimization algorithm between the experimental data and JKR curve was proposed to extract the value of the pull-off force and preload displacement simultaneously. Using the extracted value for the surface energy between the glass tip and polyacrylamide gel, the use of JKR theory was then verified to be appropriate. This error minimization algorithm was demonstrated to be easily modifiable to extract the reduced modulus of the specimen if the pull-off force is measured during the nanoindentation experiment.

The main conclusions for this study are as follows

- The challenges impeding the accurate extraction of material properties in the nanoindentation of soft linearly elastic solids are different from that discussed in the earlier chapters.
- The effects of cantilever stiffness, preload, and surface forces all influence the accurate extraction of material properties.
- The effect of the preload is equivalent to a translation of the load-displacement curve to the right of the tip-specimen contact point.

- The cantilever stiffness is observed to influence the difference between the snap-in and pull-off forces.
- Strong adhesive forces between the tip and specimen can prevent in-plane displacement of the tip, which was demonstrated to be capable of buckling a soft cantilever.
- The JKR theory was demonstrated to be appropriate for the indentation of polyacrylamide gel with a spherical glass indenter.
- An error minimization algorithm was proposed to determine the pull-off force and preload displacement simultaneously.
- This algorithm was demonstrated to be easily modifiable to extract the reduced modulus and preload displacement simultaneously if the pull-off force is known.

## REFERENCES

- Ando, Y., Ino, J., 1996. Friction and Pull-Off Force on Silicon Surface Modified by FIB. *Sens. Actuators. A, Phys.* 57 (2), 83–89.
- Bradley, R.S., 1932. The Cohesive Force between Solid Surfaces and the Surface Energy of Solids. *Philos. Mag.* 13 (86), 853–862.
- Burnham, N.A., Colton, R.J., 1989. Measuring the Nanomechanical Properties and Surface Forces of Materials using an Atomic Force Microscope. *J Vac. Sci. & Tech. A: Vac., Surf. and Films* 7 (4), 2906–2913.
- Burnham, N.A., Colton, R.J., Pollock, H.M., 1991. Interpretation Issues in Force Microscopy. *J Vac. Sci. & Tech. A: Vac., Surf. and Films* 9 (4), 2548–2556.
- Butt, H., Cappella, B., Kappl, M., 2005. Force Measurements with the Atomic Force Microscope: Technique, Interpretation and Applications. *Surf. Sci. Reports* 59, 1–152.
- Cappella, B., Baschieri, P., Frediani, C., Miccoli, P., Ascoli, C., 1997. Force-distance Curves by AFM - A Powerful Technique for Studying Surface Interactions. *IEEE Eng. Med. and Bio. Mag.* 16 (2), 58–65.
- Derjaguin, B.V., 1934. Analysis of Friction and Adhesion IV: The Theory of the Adhesion of Small Particles. *Koll.-Zeit.* 69 (2), 155–164.
- Derjaguin, B.V., Muller, V.M., Toporov, Y.P., 1975. Effect of Contact Deformations on Adhesion of Particles. *J. Coll. Interface Sci.* 53 (2), 314–326.
- Fischer-Cripps, A.C., 2004. *Nanoindentation*. Springer.

Hertz, H., 1881. *Über Die Berührung Fester Elastischer Körper (On the Contact of Elastic Solids)*. *J. Reine Angew. Math.*, 156–171.

Hodges, C.S., Cleaver, J.A.S., Ghadiri, M., Jones, R., Pollock, H.M., 2002. Forces between Polystyrene Particles in Water using the AFM: Pull-Off Force vs. Particle Size. *Langmuir* 18 (15), 5741–5748.

Hutter, J.L., Bechhoefer, J., 1993. Calibration of Atomic-Force Microscope Tips. *Rev. Sci. Instrum.* 64 (7), 1868–1873.

Ingber, D.E., Dike, L., Hansen, L., Karp, S., Liley, H., Maniotis, A., McNamee, H., Mooney, D., Plopper, G., Sims, J., Wang, N., 1994. Cellular Tensegrity — Exploring how Mechanical changes in the Cytoskeleton regulate Cell-growth, Migration, and Tissue Pattern during Morphogenesis. *Int. Rev. Cytol — A Survey of Cell Biology* 150, 173–224.

Jang, J., Sung, J., Schatz, G.C., 2007. Influence of Surface Roughness on the Pull-Off Force in Atomic Force Microscopy. *J. Phys. Chem. C* 111 (12), 4648–4654.

Johnson, K.L., 1987. *Contact Mechanics*. Cambridge University Press.

Johnson, K.L., Kendall, K., Roberts, A.D., 1971. Surface Energy and the Contact of Elastic Solids. *Proc. R. Soc. Lond. A, Math. Phys. Sci.* 324 (1558), 301–313.

Lichinchi, M., Lenardi, C., Haupta, J., Vitalib, R., 1998. Simulation of Berkovich Nanoindentation Experiments on Thin Films Using Finite Element Method. *Thin Solid Films* 312, 240–248.

Lo, C.M., Wang, H.B., Dembo, M., Wang, Y.L., 2000. Cell Movement is guided by the rigidity of the substrate. *Biophys. J.* 79 (1), 144–152.

Mann, A.B., Pethica, J.B., 1996. Nanoindentation Studies in a Liquid Environment. *Langmuir* 12 (19), 4583–4586.

Maugis, D., 1991. Adhesion of Spheres: The JKR-DMT Transition Using a Dugale Model. *J. Coll. Interface Sci.* 150 (1), 243–269.

Muller, V.M., Yushchenko, V.S., Derjaguin, B.V., 1980. On the Influence of Molecular Forces on the Deformation of an Elastic Sphere and Its Sticking to a Rigid Plane. *J. Coll. Interface Sci.* 77 (1), 91–101.

Oliver, W.C., Pharr, G.M., 1992. An Improved Technique for Determining Hardness and Elastic Modulus Using Load and Displacement Sensing Indentation Experiments. *J. Mater. Res.* 7, 1564–1583.

Ouyang, Q., Ishida, K., Okada, K., 2000. Investigation of Micro-Adhesion by Atomic Force Microscope. *Appl. Surf. Sci.* 169–170, 644–648.

Paszek, M., Zahir, N., Johnson, K., Lakins, J., Rozenberg, G., Gefen, A., Reinhart-King, C., Margulies, S., Dembo, M., Boetiger, D., 2005. Tensional homeostasis and the malignant phenotype. *Cancer Cell* 8 (3), 241–254.

Pharr, G.M., Oliver, W.C., Brotzen, F.R., 1992. On the Generality of the Relationship Among Contact Stiffness, Contact Area, and the Elastic Modulus During Indentation. *J. Mater. Res.* 7 (3), 613–617.

Sneddon, I.N., 1948. Boussinesq's Problem for a Rigid Cone. Proc. Cambridge Philos. Soc., 492–507.

Suresh, S., Spatz, J., Mills, J.P., Micoulet, A., Dao, M., Lim, C.T., Beil, M., Seufferlein, T., 2005. Connections between Single-Cell Biomechanics and Human Disease States: Gastrointestinal Cancer and Malaria. Acta Biomaterialia 1 (1), 15–30.

Tabor, D., 1977. Surface Forces and Surface Interactions. J. Coll. Interface Sci. 58 (1), 2–13.

Waals, J.D.v.d., 1893. The Thermodynamic Theory of Capillarity Under the Hypothesis of a Continuous Variation of Density. Konink. Akad. Weten. Amsterdam 1 (8).

Wang, J.Y., Velasco, A., Rajagopalan, P., Pham, Q., 2003. Directed Movement of Vascular Smooth Muscle Cells on Gradient-Compliant Hydrogels Langmuir 19 (5), 1908–1913.

Wang, T.H., Fang, T.H., Lin, Y.C., 2006. A Numerical Study of Factors Affecting the Characterization of Nanoindentation on Silicon. Mat. Sci. and Engng. 447 (1–2), 244–253.

Wells, R.G., 2008. The Role of Matrix Stiffness in Regulating Cell Behavior Hepatology 47 (4), 1394–1400.

Yu, N., Polycarpou, A.A., Conry, T.F., 2004. Tip-Radius Effect in Finite Element Modeling of Sub-50 Nm Shallow Nanoindentation. Thin Solid Films 450, 295–303.

Zammaretti, P., Fakler, A., Zaugg, F., Spichiger-Keller, U.E., 2000. Atomic Force Microscope: A Tool for Studying Ionophores. *Anal. Chem.* 72 (16), 3689–3695.

## CHAPTER 5: CONCLUSIONS AND FUTURE CHALLENGES

This thesis has addressed a number of the challenges impeding the accurate extraction of material properties through nanoindentation using both a nanoindenter and an Atomic Force Microscope (AFM). The approach of this study focused on some of the most common deviations from the stringent assumptions necessary for the accurate use of the stiffness equation to extract material properties from the load-displacement measurements during nanoindentation experiments. These assumptions include: (i) the specimen is an infinite half-space, (ii) the indenter has an ideal geometry, (iii) the material is linearly elastic and incompressible, and (iv) there are no interaction surface forces during contact (such as adhesive or frictional forces).

The first part of this study, as presented in Chapter 2, considers an isotropic, linearly elastic solid to directly reassess the applicability of Sneddon's solution (1948; 1965) (which the stiffness equation was derived from) in practical nanoindentations. These nanoindentations typically involve specimens with finite dimensions, specimens with Poisson's ratio less than 0.5, and an indenter tip with a finite tip radius. This chapter addressed deviations from the common assumptions through a series of systematic numerical simulations using commercial finite element (FE) package ABAQUS.

In Chapter 2, the study clearly defined a new set of criteria for converged 2-dimensional (axisymmetric) geometry to be 'sufficiently large' to be compared to an infinite half space, as follows

$$\frac{r_s}{h_s} \geq 1$$

and

$$\frac{h_s}{h_{max}} \geq 100 \quad (1)$$

where  $r_s$  and  $h_s$  are the radius and height of the specimen, respectively, and  $h_{max}$  is the maximum indentation depth attained. Geometrical modeling issues are seldom detailed in the literature and these criteria will provide a common basis for comparison with Sneddon's solution. However, these criteria were found to be considerably more stringent than the conventional rule-of-thumb criterion (Fischer-Cripps, 2004) to determine the dimensions for the 'sufficiently large' specimen. It was concluded that the conventional criterion possibly achieved a 'pseudo-convergence', when a slight change in the aspect ratio of the specimens will result in a big deviation in the measured load-displacement behavior.

In addition, in Chapter 2, the study addressed the finite tip effect and developed an accurate empirical load-displacement relationship that takes into account the finite tip radius,  $\rho$ , as follows,

$$\begin{aligned} P &= f(\nu) \frac{2 E \tan(70.3^\circ)}{\pi (1 - \nu^2)} h (h + g(\rho)) \\ &= (a_1 \nu^2 + a_2 \nu + a_3) \frac{2 E \tan(70.3^\circ)}{\pi (1 - \nu^2)} h (h + c_1 \rho^2 + c_2 \rho) \end{aligned} \quad (2)$$

where,  $a_1 = -0.062$ ,  $a_2 = -0.156$ ,  $a_3 = 1.12$ ,  $c_1 = 1.50e4 \text{ m}^{-1}$ , and  $c_2 = 1.17e-1$ . With this relationship, an expression for the correction factor required to account for the neglect of the finite tip effect was derived. This relation for the correction factor revealed the relationship between the effects arising from the use of a compressible specimen and an indenter tip with a finite radius for the first time. It confirms that this composite correction factor is the product of the individual correction factors to separately account

for specimen compressibility and finite tip radius, first proposed by Troyon and Huang (2004). It was also demonstrated that the neglect of finite tip radius will consistently result in an overestimation for the extracted reduced modulus,  $E_r$ .

While it is commonly expected that the finite tip radius effect will be less significant for deep indentations, this study, for the first time, established the criterion for ‘sufficiently deep’ indentations as a function of tip radius. Nanoindentation experiments were performed on a linearly elastic solid (natural latex rubber) to confirm that finite tip radius effects are not significant when sufficiently deep indentations are achieved.

Finally in Chapter 2, two practical applications were proposed. The first is a novel procedure to identify the indenter tip radius using Eq. (2). While it was demonstrated that finite tip radius effects are important for the accurate extraction of  $E_r$ , manufacturers are usually only able to provide an estimation of the tip radius up to 100 nm. It was demonstrated that the proposed technique could achieve an accurate determination of the tip radius without an *a priori* knowledge for the material property of the specimen. The second application is a procedure to decouple the extracted material properties into its Young’s modulus,  $E$ , and Poisson’s ratio,  $\nu$ , through the use of conical and spherical tip indenters. It should be noted however, that the applicability of the proposed procedures are limited by the availability of linearly elastic solids (to large strains), which are scarce in nature. This study naturally led us to the next part of our study in elasto-plastic solids, since most engineering materials exhibit plastic flow on the very onset of indentation with a sharp indenter tip, as in practical nanoindentations.

In Chapter 3, the objective of the study was to reassess some of the common assumptions to adapt elastic-plastic indentations to the linear elastic contact problem to

utilize the stiffness equation. The study also examined the applicability of the correction factor derived under linearly elastic conditions on elasto-plastic indentations, which is commonly practiced by the nanoindentation community.

In Chapter 3, it was established that while the assumption of a linearly elastic unloading curve and the equivalent problem (a mapping of an elastic indentation by a conical indenter on a plastic imprint to an elastic indentation by an equivalent conical indenter on a flat surface) may hold true, Sneddon's solution cannot adequately predict the unloading load-displacement behavior for an elasto-plastic indentation. Due to the elastic recovery during unloading, the sides of the plastic imprint are generally curved; as such, a single geometrical parameter, in this case the equivalent half-angle,  $\alpha'$ , cannot adequately map the actual problem (Sakai, 2003; Stilwell and Tabor, 1961). Consequently, Sneddon's solution with  $\alpha'$  cannot effectively describe the unloading load-displacement relationship.

Pharr and Bolshakov (2002) demonstrated that the stress field during the unloading process resembled that of an elastic indentation with a parabolic indenter. It was therefore established that the stiffness equation is more suitable for the analysis of elasto-plastic unloading curves, due to its applicability to all axisymmetric indenters with infinitely smooth profiles. Yet, the stiffness equation requires an accurate determination of the projected area of contact,  $A$ . The latter is usually calculated using linear elastic considerations, which had been shown to be sufficiently accurate for  $h_r/h_{max} < 0.7$  (Oliver and Pharr, 2004). However, for an elastic, perfectly plastic material, this criterion is equivalent to  $E/\sigma_y < 30$ , which is quite limited in scope for most materials of interest. For hardening elastic-plastic solids, both pile-ups and sink-ins will affect the accuracy of  $A$

derived using linear elastic considerations. In addition,  $A$  is also found to be a function of the indenter's tip-radius,  $\rho$ , through the elastic-plastic loading stage of the indentation cycle. It is therefore imperative to develop an alternative approach to determine  $A$ .

A novel experimental method to directly measure  $A$  using electrical resistance method was proposed. The viability of this method was demonstrated based on experimental results. Once  $A$  was accurately determined, it was observed that the error of the extracted Young's modulus became insensitive to both  $E/\sigma_y$  (a measure of the extent of plasticity) and  $\rho$ . This suggests that an accurately measured  $A$  eliminates any effects arising from plasticity or the finite tip radius.

The error, however, remains sensitive to  $\nu$ . It was found that  $\nu$  determined the amount of residual stress at the plastic imprint of the indent, which certainly violates the assumptions in the theoretical derivation. This however, is in stark contrast with the errors arising from  $\nu$  due to the negligence for lateral displacements in the theoretical derivation for linear elastic indentations. Nonetheless, it is common practice to use the correction factor for  $\nu$  derived for linear elastic indentations on practical elasto-plastic indentations. A comparison between the correction factors to account for the residual stresses at the imprint and for the lateral displacements under indentation showed that both correction factors are quantitatively similar. The correction factor for  $\nu$  in elasto-plastic indentations was only slightly larger than the one for linear elastic indentations, which explains why errors were not reported when the correction factors were used interchangeably. Nevertheless, it is important to note that these correction factors are essentially different.

Finally in Chapter 3, concerning the determination of the yield strength of the material, a power law relationship was identified between  $h_e/h_{max}$  and  $E/\sigma_y$  as follows,

$$\frac{h_e}{h_{max}} = 2.98 \left( \frac{E}{\sigma_y} \right)^{-0.68} \quad (3)$$

where  $h_e$  is the elastic recoverable displacement and  $\sigma_y$  is the yield stress of the specimen. This relation was verified experimentally and found to provide an upper bound for the yield stress of pressure sensitive and/or strain hardening materials.

In Chapter 4, the study addressed some of the challenges faced in the nanoindentation of soft materials. In general, the challenges discussed previously hold for soft materials as well. However, as shown in Chapter 2, deep indentations are usually achieved in the indentation of soft materials which significantly reduce the effects from the finite tip radius. Also, soft rubber-like materials are usually incompressible, which obeys the stringent assumption of incompressibility for the stiffness equation. In addition, soft materials do not commonly deform plastically. All of the above seem to suggest that the elastic properties of these soft materials can be accurately extracted from the nanoindentation experiments. However, a different set of challenges was found to impede the accurate extraction of material properties for soft materials during nanoindentation.

Soft materials are usually rate-sensitive and nonlinearly elastic. The asperities on the surface usually conform to the shape of the indenter, increasing the effective surface area of contact, which tends to amplify the surface interaction forces. Furthermore, since the AFM is commonly used in these experiments for its superior force resolution, the cantilever stiffness becomes an additional parameter for consideration in the problem.

To simplify the problem, soft linear elastic solids were considered in this study. The effects of the cantilever stiffness, preload, and tip-specimen surface interaction

forces were carefully examined. These effects were found to influence each other and the overall accuracy of the extracted material properties during the nanoindentation. To examine these effects further, three indentation scenarios were investigated: (i) the indentation with a ‘rigid cantilever’ on a soft material with no surface forces, (ii) the indentation with a compliant cantilever on a rigid material with surface forces, and (iii) the indentation with a compliant cantilever on a soft material with surface forces.

The first experiment examined the effects of preload by indenting natural latex rubber with a nanoindenter. The preload was introduced by the finite indentation force required by the nanoindenter to establish contact. It was demonstrated that it is crucial to account for the preload to accurately extract elastic properties using the stiffness equation; otherwise, there will be a severe overestimation for  $E_r$ .

The second experiment examined the interaction between the cantilever stiffness and surface forces during an indentation. The experiment was performed using an AFM with a spherical glass tip mounted on two separate cantilevers with different spring constants. The specimen used in the example was a glass slide. It was observed that the snap-in force was smaller than the pull-off force. This difference was larger for indentations performed using the softer cantilever, which is consistent with the work of Cappella et al. (1997). Cappella et al. demonstrated that this hysteresis can be eliminated with the use of a sufficiently stiff cantilever. However, while Cappella et al. considered a single Lennard-Jones type force function to describe the surface force between the tip and the specimen, it was proposed that different types of surface forces could be at play during the loading and unloading segments of the nanoindentation experiment. During the approach, long-range forces such as Van der Waals and electrostatic forces can cause

the unstable snap-in of the cantilever, while short-range forces such as capillary force can be responsible for the larger pull-off force during the retraction of the cantilever.

Finally, for the third scenario, the study considered the nanoindentation of a soft linearly elastic material, 12% polyacrylamide gel with a spherical glass tip mounted on two cantilevers with different stiffness. In this experiment, the effects from the cantilever stiffness, preload, and surface forces were present and coupled.

Using the softer cantilever, the load-displacement measurement was found to resemble an S-shaped curve. To understand the deformation of the cantilever during the indentation, FE simulations were performed. It was demonstrated that the softer cantilever was most likely buckled during the indentation due to the adhesion between the indenter tip and the specimen.

Using the stiffer cantilever, the load-displacement curve was also observed to be distinctly different from Hertz's prediction. It was determined that this was possibly due to surface adhesive forces and preload which were not accounted for in Hertz's relation. The Johnson-Kendall-Roberts (JKR) model was used to account for the tip-specimen adhesion. However, information on the pull-off force and the preload were unavailable. A stiffer cantilever will be required to measure the pull-off force, but its force resolution will be compromised. Hence, a minimization scheme was proposed to derive the pull-off force and the indentation depth due to preload simultaneously. This scheme offered an alternative method to study the surface interaction forces between the indenter tip and the specimen. The extracted surface energy between the glass tip and the polyacrylamide gel was used to verify the appropriate use of the JKR theory. It was also subsequently demonstrated that with an accurate measurement for the pull-off force, the proposed

minimization scheme can be easily modified to extract the reduced modulus of interest and the preload displacement simultaneously. Neglecting preload and tip-specimen adhesion will inevitably result in an overestimation for the extracted reduced modulus for the specimen.

This thesis has shed light on several concepts related to the field of nanoindentation, but many open questions still remain. The ultimate challenge for the nanoindentation to extract a representative stress-strain curve from nanoindentation data for comparison with traditional uniaxial measurements still remains. An important milestone towards this goal was achieved recently when researchers such as Dao et al. (2001) proposed the use of the forward-reverse algorithms to extract both elastic and plastic properties for the material of interest using nanoindentation. Unfortunately, due to its nature as an inverse problem, where the number of unknowns exceeds the number of constraints, researchers have found that this method may not yield unique solutions (Chen et al., 2007).

A plausible method to derive an equivalent stress-strain for the material under indentation is to experimentally measure the full-field stress and strain fields of the material under indentation. Established optical techniques such as photoelasticity, coherent gradient sensing (CGS), and digital image correlation (DIC) may provide valuable information on the stress and strain fields of the specimen.

Lastly, another important area for research in nanoindentation is to account for anisotropy in materials. For the length scale of interest to nanoindentations, many solids exhibit anisotropy. Since the nanoindentation is effectively a multiaxial loading experiment, the challenge to decouple the material properties at different orientation

remains. An interesting method to study anisotropy experimentally was proposed by Yonezu (2007), who attempted to infer the material's anisotropy by measuring the dimensions of the plastic imprint at the indent in different directions. Using the spherical indenter, the plastic imprint will resemble an ellipse with the minor axis parallel to the material orientation with larger elastic recovery.

No doubt, the development of the nanoindentation mechanical testing technique has come a long way since Hertz's pioneering contribution in 1881. Commercial nanoindenters today have made nanoindentation a relatively simple test to perform. Nevertheless, many challenges concerning the practical extraction of useful material properties still remain.

## REFERENCES

- Cappella, B., Baschieri, P., Frediani, C., Miccoli, P., Ascoli, C., 1997. Force-distance Curves by AFM - A Powerful Technique for Studying Surface Interactions. *IEEE Eng. Med. and Bio. Mag.* 16 (2), 58–65.
- Chen, X., Ogasawara, N., Zhao, M., Chiba, N., 2007. On the uniqueness of measuring elastoplastic properties from indentation: The indistinguishable mystical materials. *J. Mech. Phys. Solids* 55, 1618–1660.
- Dao, M., Chollacoop, N., Vliet, K.J.V., Venkatesh, T.A., Suresh, S., 2001. Computational Modeling of the Forward and Reverse Problems in Instrumented Sharp Indentation. *Acta Materialia* 49, 3899–3918.
- Fischer-Cripps, A.C., 2004. *Nanoindentation*. Springer.
- Oliver, W.C., Pharr, G.M., 2004. Review: Measurement of Hardness and Elastic Modulus by Instrumented Indentation: Advances in Understanding and Refinements to Methodology. *J. Mater. Res.* 19, 3–20.
- Pharr, G.M., Bolshakov, A., 2002. Understanding Nanoindentation Unloading Curves. *J. Mater. Res.* 17, 2660–2671.
- Sakai, M., 2003. Elastic recovery in the unloading process of pyramidal microindentation. *J. Mater. Res.* 18 (7), 1631–1640.
- Sneddon, I.N., 1948. Boussinesq's Problem for a Rigid Cone. *Proc. Cambridge Philos. Soc.*, 492–507.

Sneddon, I.N., 1965. The Relation Between Load and Penetration in the Axisymmetric Boussinesq Problem for a Punch of Arbitrary Profile. *Int. J. Engng. Sci.* 3, 47–57.

Stilwell, N.A., Tabor, D., 1961. Elastic recovery of conical indentations. *Proceedings of the Physical Society of London* 78 (500), 169.

Troyon, M., Huang, L., 2004. Correction factor for contact area in nanoindentation measurements. *J. Mater. Res.* 30 (3), 610–617.

Yonezu, A., 2007. Experimental Observations of the Plastic Imprint for Anisotropic Solids. Personal Communication.